THE EFFECT OF EVAPORATION ON FRONTOGENESIS

by

HO-CHUN HUANG

B.S., Atmospheric Science, National Taiwan University
(1984)

Submitted to the Department of
Earth, Atmospheric, and Planetary Sciences
in partial fulfillment of the requirement for
the Degree of

Master of Science in Meteorology

at the

Massachusetts Institute of Technology

September 1989

Signature of Author _____
Department of Earth, Atmospheric and Planetary Sciences
September 1989

Certified by _____
Professor Kerry A. Emanuel
Thesis Supervisor

Accepted by _____
Chairman, Departmental Committee on Graduate Students

THE EFFECT OF EVAPORATION ON FRONTOGENESIS

by

HO-CHUN HUANG

Submitted to the Department of
Earth, Atmospheric and Planetary Sciences
on September 1989 in partial fulfillment of the requirement
for the Degree of Master of Science in Meteorology

Abstract

Studies of the thunderstorms along squall lines show that evaporation is very important in maintaining the downdraft. The effect of condensational heating on frontogenesis has also been examined in many studies. Numerical simulations show that the frontogenesis in the moist case is much larger than in the dry case. We here propose that the combination of condensation heating and evaporation cooling enhances frontogenesis.

Analysis of *GALE pam-II* surface network data is used to diagnose the rate of rain evaporation near a frontal rain band. A residual method is used to estimate the rate of evaporation from *pam-II* surface data set. A modified moist semigeostrophic model is outlined to study evaporative effects on frontogenesis. Model output shows increased convergence near the surface front with the effect of evaporation. The response to frontogenetical forcing due to condensational heating is a strong, concentrated and sloping updraft. The evaporative effect also induces a concentrated sloped downdraft on the cold side of the front. Frontal collapse in the case with evaporation is faster than that without evaporation.

Sensitivity tests with different rates of evaporation and criteria for evaporation occurrence indicate that rain evaporation can accelerate frontogenesis. The effect of diabatic heating will create sources and sinks of potential vorticity. The low level positive potential vorticity anomaly and upper level negative potential vorticity anomaly due to latent heat

release might meet the necessary condition for secondary baroclinic instability. Evaporative cooling also causes a local maximum of potential vorticity which is favorable to secondary baroclinic instability.

Thesis supervisor: Dr. Kerry A. Emanuel
Title: Professor of Meteorology

Acknowledgments

I am grateful to my thesis advisor, Professor Emanuel, without his help and critical suggestions my thesis would not have been possible. I want to thank my fellow students Robert Black, Chris Davis, Peter Neilley, John Nielsen, Nilton Renno and Shuntai Zhou, the discussions with them have always been helpful. Specially thank to Jane McNabb, with her kindness and help give me a happy life as a graduate student in MIT. Finally, I want to thank all my friends for their advise, support and friendship during these years in MIT.

Table of Contents

Chapter 1: Introduction

In the atmosphere there are many cases where a vertical sounding is stable to upright convection but there is significant cloud and precipitation. Many studies show that the atmosphere is often stable to upright convection, but still unstable to slantwise moist convection. Detailed case studies of slantwise convection (Emanuel, 1983 ; Sanders and Bosart, 1985) indicate that near neutrality to moist adiabatic displacements along M-surfaces is characteristic.

In the New England Winter Storms Experiment, a majority of updrafts were observed to be nearly neutral or slightly unstable to slantwise convection. It also showed that this situation sometimes persists for many hours after the condition of neutrality is first observed. Theoretical Studies show that the response to frontogenetical forcing is inversely proportional to slantwise stability. A particularly strong response should continue in an atmosphere which, having been previously unstable to slantwise convection, has undergone an adjustment to neutrality (Emanuel, 1985).

It appears that slantwise convection releases the slantwise instability whenever it is present, and it releases the instability so quickly that the sounding is always nearly neutral. It is observed that in many frontal zones, the air is stable to upright convection and nearly neutral to slantwise convection. In this circumstance the structural characteristics of slantwise convection can persist even after a condition of near neutrality has been achieved, as long as there is frontogenetical forcing (Emanuel, 1985 ; Sanders and Bosart, 1985).

Hoskins (1971) studied frontogenesis in a constant deformation field. The model simulated both the surface front and the upper level front, and the results show good agreement with the observations made by Sanders (1955), and Reed (1955). The discontinuity of the temperature gradient formed in a finite time. He also noticed that diabatic heating will increase the convergence at the surface due to the increasing vertical velocity, thus increasing the rate of surface frontogenesis. The effect of surface friction will enhance the Ekman layer suction at the surface and thus increase upward motion, but the horizontal divergence at the top of the planetary boundary layer will inhibit the upward motion and weaken the surface front.

Several studies have examined frontal circulations which include diabatic forcing typical of latent heat release. Sawyer (1956) included a diabatic source term in what is now known as the Sawyer-Eliassen equation for cross-frontal circulation. Hoskins and Bretherton (1972) introduce the equations for frontogenesis in geostrophic coordinates, which facilitates the study of frontogenesis. Emanuel (1985) solved the Sawyer-Eliassen equation to study the nature of the response to frontogenetical forcing in an atmosphere which is nearly neutral to moist slantwise convection. In the dry case, a frontal circulation has ascent on the warm side of maximum geostrophic forcing and descent on the cold side of it. His analysis shows that the response due to diabatic heating is a strong, concentrated, sloping updraft ahead of the region of maximum geostrophic frontogenetical forcing, while the downdraft occurs over a large area on the cold side. It appears that ageostrophic flow due to condensation is frontolytic at the position of the surface front but strongly frontogenetical near the base of the sloping updraft ahead of the front. The inclusion of evaporation and melting effects of falling precipitation has been suggested as possibly modifying the strong downdraft near the

front. Once the condensation begins in the frontal zone, it would produce sinks and sources of potential vorticity, thus sharp gradients in potential vorticity would develop relatively quickly, and it is likely that the necessary condition for barotropic/baroclinic instability may be met in the frontal zone.

Potential vorticity in the semigeostrophic systems plays the same role as static stability does in quasi-geostrophic systems, and the intrinsic length and time scales of baroclinic waves vary with the square root of the potential vorticity. Latent heat release will tend to produce a positive potential vorticity anomaly in the lower troposphere and an upper tropospheric negative potential vorticity anomaly. These anomalies are then advected horizontally by the total wind field. When the moist potential vorticity (q_e) in the ascent region becomes small, as it often does in saturated regions within cyclones, the geostrophic momentum approximation breaks down. It appears that the inertia of the ageostrophic flow may have an important effect on frontogenesis.

The study of Thorpe and Emanuel (1985) shows that if the geostrophic state is not allowed to change by the ageostrophic flow, latent heat release leads to descent in the region of maximum geostrophic forcing at the surface. This implies that such heating may locally decrease frontogenesis (as found by Emanuel, 1985). For a time dependent model, however, results show that latent heat release will increase the rate of surface frontogenesis. The results show that the position of maximum vertical velocity descends toward the lower boundary after one day of simulation. The ageostrophic horizontal velocity shows a tendency to enhance the convergence along the frontal surface. The maximum cyclonic vorticity is about five times that in the dry case, while the minimum is nearly the same as that

in the dry case. Vertical symmetry does not exit in the moist case, as the maximum relative vorticity on lower boundary is nearly four times that at the upper boundary. The peak potential vorticity increase due to condensation is five times the initial value at the surface, with a broad region of potential vorticity decrease at upper levels. The vertical velocity is three times as strong in the dry case but the horizontal ageostrophic velocity has increased only slightly. Similar dynamical results were found in the analytic study of baroclinic instability in a the two-layer semigeostrophic model and multilevel semigeostrophic model by Emanuel, Fantini and Thorpe (1987).

The rate of frontogenesis in physical space can be derived from

$$\frac{\partial}{\partial x}\frac{d\theta}{dt}=\frac{\partial}{\partial x}\frac{\partial\theta}{\partial t}+\frac{\partial}{\partial x}\left(u\frac{\partial\theta}{\partial x}\right)+\frac{\partial}{\partial x}\left(w\frac{\partial\theta}{\partial z}\right) \quad ,$$

$$=\frac{\partial}{\partial t}\frac{\partial\theta}{\partial x}+u\frac{\partial}{\partial x}\frac{\partial\theta}{\partial x}+w\frac{\partial}{\partial x}\frac{\partial\theta}{\partial z}+\frac{\partial u}{\partial x}\frac{\partial\theta}{\partial x}+\frac{\partial w}{\partial x}\frac{\partial\theta}{\partial z} \quad ,$$

$$=\frac{d}{dt}\left(\frac{\partial\theta}{\partial x}\right)+\frac{\partial u}{\partial x}\frac{\partial\theta}{\partial x}+\frac{\partial w}{\partial x}\frac{\partial\theta}{\partial z} \quad ,$$

or,

$$\frac{d}{dt}\left(\frac{\partial\theta}{\partial x}\right)=\frac{\partial S}{\partial x}-\frac{\partial u}{\partial x}\frac{\partial\theta}{\partial x}-\frac{\partial w}{\partial x}\frac{\partial\theta}{\partial z} \quad .$$

Where $d\theta/dt = S$, and S is the source term.

Since evaporative cooling or condensational heating occurring in the interior of atmosphere will change the distribution of the θ field, the rate of frontogenesis could be strongly affected by diabatic forcing. Seitter and Kuo (1983) have shown that the evapora-

tion of raindrops is important in maintaining a downdraft in the thunderstorms of squall lines. Srivastava (1985) also shows that the strength of downdrafts is dependent on the amount of rain water falling from a cloud. The study of squall-line life cycles shows that it is dependent on the strength of the developing cold pool (Weisman, Klemp and Rotunno, 1988). Together, condensation and evaporation will accelerate a secondary circulation and enhance the convergence near the surface front. Also, the diabatic heat release in the stronger updraft and diabatic cooling in the downdraft will increase the kinetic energy of frontal systems.

Since condensation produces a strong source of potential vorticity at low levels, it is possible that the necessary condition for barotropic/baroclinic instability will be met locally in the frontal zone due to evaporation. It appears that an important role of moist processes in the atmosphere is to allow baroclinic development locally in the domain where it would otherwise be stable to baroclinic instability.

For the above reasons it appears of interest and importance to study the effects of evaporation on frontogenesis. The following sections will briefly review some related studies, perform a data analysis using the *GALE pam-II* surface data set to estimate the rate of evaporation, describe the numerical model which is used to study the effect of evaporation on frontogenesis and discuss the results.

Chapter 2 : Review

The important of diabatic heating on the development of cyclones has been studied by Emanuel, Fantini and Thorpe (1987). The effect of near neutrality to slantwise convection causes the updraft to collapse down to very small scale and somewhat enhances the rate of surface frontogenesis (Thorpe and Emanuel, 1985). Emanuel, Fantini and Thorpe (1987) find analytic solutions of two-dimensional disturbances in a two-layer semigeostrophic model. They also performed numerical simulations using a multilevel semigeostrophic model. Some parameter fields from the model have features which resemble to the study of frontogenesis of Thorpe and Emanuel (1985). The critical parameter is γ, defined as

$$\gamma \equiv \frac{\Gamma_m q_{ge}}{\Gamma_d q_{g0}} \quad ,$$

where Γ_m and Γ_d are the moist and dry adiabatic lapses, respectively. q_{ge} and q_{g0} are respectively the moist and geostrophic potential vorticity. The parameter γ serves as a measure of the strength of condensation. For the analytic solutions of the two-layer model, in the dry case ($\gamma = 1$), the maximum value of growth rate is 0.586 when k^2 (k is the wavenumber) equals 0.828. The value of the maximum growth rate in the continuous Eady model is 0.62 occurring at a k^2 of 0.65.

When $\gamma \neq 1$, the problem becomes nonlinear due to the dependence of γ on the sign of w. The values of growth rate for different values of γ show that the total wavelength at maximum growth rate decreases with γ, and the growth rate increases with decreasing γ. The asymptotic analysis shows that the maximum growth rate is about 2.5 times that of the dry

case as $\gamma \rightarrow 0$. In the limiting case of small γ the updraft width becomes vanishingly small. The most rapidly growing moist mode with zero stability to slantwise moist convection has a total horizontal wavelength of about 0.6 times that for the maximum growing dry mode. The horizontal structure of the various field for the case $\gamma = 0.08$ with L near the wavelength of maximum growth shows that the most obvious effect of condensation is to narrow and intensify the updraft and weaken and broaden the downdraft. Frontal collapse occurs at low levels first, unlike in the dry model, in which singularities appears at the lower and upper level simultaneously. The strongest descent is just to the rear of the surface pressure trough. The associated meridional wind field is strongly asymmetric at the lower level but only modestly so aloft.

The vertical structure of baroclinic waves together with other wave properties were described for their numerical simulations using a multilevel semigeostrophic model. In their results, in the moist development the horizontal scale is contracted in the region of ascent, and the moist mode grows between two and three times as fast as the dry mode. In the dry simulation the warm air maximum and cold air minimum of meridional (along-front) flow are equal in magnitude and symmetrical in the lower and upper parts of the domain. A small asymmetry in the vertical is found in the moist case but the main asymmetry is that the warm southerly flow is substantially stronger than the cold northerly flow. The stronger warm flow and the narrow region of ascent are ahead of the frontal surface.

As condensational heating is increased with time, the slope of the moist ascent is larger at lower levels than that of the ascent aloft. A large horizontal gradient of vertical velocity on the cold side of the ascent region is found in the two-layer model. Although it also occurs

in the dry case, it is more significant in the moist case. The moist simulation shows that latent heat release will produce a lower tropospheric positive anomaly and an upper troposphere negative anomaly of potential vorticity. A positive potential vorticity anomaly is consistent with a balanced flow having cyclonic relative vorticity and increased static stability, and the opposite signs apply for a negative anomaly (Hoskins et al. 1985). Thus in moist baroclinic waves there is an increase in stability and cyclonic vorticity at low levels and a decrease at upper levels due to the condensation. Because of horizontal advection, this occurs not only where the condensation is located but throughout the wave.

While these studies show that diabatic heating can have an important effect on frontogenesis, they did not examine the possible contribution of cooling due to evaporation of precipitation. In the real atmosphere, the cooling due to raindrop evaporation will commence shortly after condensation begins. Both processes should effectively change the distribution of the temperature field in the interior of the atmosphere.

Seitter and Kuo (1983) use a two-dimensional numerical model to study the dynamical structure of squall line type thunderstorms. They found that the vorticity production due to liquid water loading, condensational heating and evaporative cooling lead to an upshear slope of the updraft/downdraft interface. In their simulations, liquid water loading is important in producing a downdraft. But if evaporation is not permitted, liquid water loading is not sufficient to maintain the the downdraft. This suggests that evaporation plays an important role in establishing the downdraft in thunderstorm circulations. For similar reasons, a strong downdraft enhanced by evaporation could accelerate the secondary circulation during frontogenesis which, in turn, may accelerate frontogenesis.

Srivastava (1985) used a one-dimensional, time dependent model to study microbursts driven by evaporation of raindrops and precipitation loading. His study shows that intense downdrafts frequently develop as the lapse rate of temperature in the environment approaches the dry-adiabatic lapse rate. With the nearly neutral lapse rates, intense downdrafts can occur with small rainfall rates or precipitation content. When the thermal stratification becomes more stable, one needs a higher rainfall rates or precipitation contents to drive intense downdrafts. Although his study showed that with a stable lapse rate more raindrops were needed to drive a strong downdraft, it suggests the potential importance of evaporation in enhancing downdraft forced by other mechanism. A latter study (Srivastava, 1987), which includes the effects of ice crystal melting shows that much less rain water is needed in the presence of ice crystals to obtain a downdraft of similar magnitude. This suggests that both ice crystal and rain formation associated with slantwise ascent may enhance the downdrafts of cross-frontal circulations.

The previous work suggests that evaporation may play an important role in enhancing the secondary circulation associated with frontogenesis. Also, diabatic heating and cooling play an important roles as sources and sinks of potential vorticity. A simple model to study the effects of evaporation is described. We begin, however, with an estimate of evaporation in frontal zones based on surface observations.

Chapter 3 : Data Analysis

We propose to examine the occurrence of the evaporation of rain near frontal areas and estimate the rate of evaporation. Since the resolution of upper air stations is coarse, and data with short time measurements is unavailable, we try to perform the analysis using the surface data to estimate the rate of evaporation near the surface. The data set we used is from the *Genesis of Atlantic Lows Experiment's (GALE) pam-II* network. The *pam-II* network contains 50 stations spaced approximately 60km apart (figure 3.1) taking measurements at 5 minutes intervals. The upper air network has a much smaller resolution than the *pam-II* network, thus the data set allows us to distinguish the mesoscale motions, and investigate the interaction between different scales.

Because *pam-II* stations only observe parameters (temperature, dew point, wet bulb temperature, potential temperature, wet potential temperature, pressure, wind direction, wind speed, gust wind, mixing ratio, relative humidity, and precipitation accumulation) at the surface, a residual method is developed which uses the surface data to determine the occurrence of the rain evaporation and the rate of the evaporation.

From the water vapor equation;

$$\frac{dr}{dt} = \frac{\partial r}{\partial t} + \vec{v} \cdot \nabla r$$

$$= E_r - \nabla \cdot (\vec{v}' r'),$$

where E_r is the rate of evaporation. The second term on the right hand side includes the

fluxes of water vapor from the soil , surface evaporation, turbulence, diffusion, etc.. In our data analysis we will explicitly assume these fluxes are small compared to E_r.

Thus the rate of evaporation can be calculated from the residual of the surface total derivative of the mixing ratio of water vapor.

$$E_r = \frac{L_v}{C_p \Pi_0}\left(\frac{\partial r}{\partial t} + u\frac{\partial}{\partial x} + v\frac{\partial}{\partial y}\right) \qquad (3.4)$$

The case we analyzed is IOP-6 of *GALE*. The operation time is from 14 FEB 1700Z to 15 FEB 0930Z. A large precipitation amount has been recorded by *pam-II* stations between 14 FEB 2355Z to 14 FEB 0855Z (figure 3.2). From the NWS radar summary (figure 3.3), the rain band passed through the network area between 14 FEB 2335Z and 15 FEB 0635Z. The values of E_r calculated from *pam-II* data are shown in figure 3.4.

From figures 3.3 and 3.4, the major evaporation areas (positive areas) are located in the major frontal rain band, especially from 0135Z to 0435Z. The maximum rates of evaporation calculated from *pam-II* data set during 14 FEB 2030Z to 15 FEB 0530Z range from $4 \times 10^{-7} s^{-1}$ to $1 \times 10^{-6} s^{-1}$, which is equivalent to evaporating 1 g/kg of rain in from 41.7 minutes to 16.7 minutes. The results show that the incorporation of evaporation in studying the frontogenesis should be influential.

Chapter 4 : Numerical Model

Emanuel (1985), Thorpe and Emanuel (1985) and Emanuel, Fantini and Thorpe (1987) implicitly neglect the effect of evaporation of raindrops by assuming that once the raindrop is formed it will fall and reach the ground in a time short enough that no evaporation will take place. This assumption may be reasonable for rain drops formed in the lower portion of the atmosphere. But the depth of the atmosphere which is used in these studies is about 10km. Thus precipitation may fall through deep unsaturated regions of the atmosphere, affecting temperatures over a large volume through evaporation. The inclusion of the effects of evaporation should be important in understanding the dynamical structure of baroclinic waves and frontogenesis.

From the works mentioned in the last section, ageostrophic motion appears to be an important mechanism in frontogenesis. The ageostrophic advection which is absent from the quasi-geostrophic system can be incorporated by using the semigeostrophic system. Here, we add the effect of evaporation to the model. The model initially has an uniform potential vorticity field, and a horizontal temperature gradient is specified on the two horizontal boundaries. This is the same as in the moist and dry cases of Thorpe and Emaneul (1985). Frontogenesis is induced by a constant, specified deformation field. The effect of moisture will be represented by a diabatic source consistent with the conservation of moist potential vorticity in the saturated region. It is assumed that the atmosphere has undergone adjustment by slantwise convection to a state of small stability to slantwise displacements.

4.1 Coordinate Transformation

The equations for frontogenesis can be found in Hoskins and Bretherton (1972). They describe two-dimensional semigeostrophic dynamics using the geostrophic coordinates:

$$X \equiv x + \frac{V_g}{f}, \quad Z \equiv z, \quad \tau \equiv t,$$

where V_g is the geostrophic flow along the front and x is the coordinate along the temperature gradient. The definition of "pseudo height" z which is a function of pressure p is

$$z = \left[1 - \left(\frac{p}{p_0}\right)^{\kappa}\right]\frac{H_s}{\kappa} \quad ,$$

where $H_s = p_0/\rho_0 g$ and $\kappa = R_d/C_p$, ρ is the density, g the acceleration of gravity, R_d the gas constant for dry air, and C_p the specific heat of dry air at constant pressure. The subscript 0 denotes a the typical surface reference value. To a good approximation, z can be treated as physical height over the troposphere (Hoskins and Bretherton ,1972). The pseudo height is bounded above by $z = z_a$, where $z_a = H_s/\kappa$.

We can derive the relations

$$\frac{d}{dt} = \frac{d}{d\tau}$$

where for three dimensional flow:

$$\frac{d}{dt} = \frac{\partial}{\partial t} + u\frac{\partial}{\partial x} + v\frac{\partial}{\partial y} + w\frac{\partial}{\partial z} \quad ,$$

$$u \equiv \frac{dx}{dt} \quad , \quad v \equiv \frac{dy}{dt} \quad , \quad w \equiv \frac{dz}{dt} \quad .$$

and

$$\frac{d}{d\tau} = \frac{\partial}{\partial \tau} + U\frac{\partial}{\partial X} + V\frac{\partial}{\partial Y} + W\frac{\partial}{\partial Z} \quad ,$$

with specified deformation field,

$$U \equiv \frac{dX}{d\tau} = -\alpha X + U_g \quad , \quad V \equiv \frac{dY}{d\tau} = \alpha Y + V_g \quad , \quad W \equiv -\frac{\zeta}{f}\frac{\partial \psi}{\partial X} \quad .$$

The relations of the derivative terms and parameters between the two coordinate systems are

$$\frac{\partial}{\partial x} = \frac{\partial X}{\partial x}\frac{\partial}{\partial X} = \left(1 + \frac{1}{f}\frac{\partial V_g}{\partial x}\right)\frac{\partial}{\partial X} = \frac{\zeta}{f}\frac{\partial}{\partial X} \quad , \tag{4.1}$$

$$\frac{\partial}{\partial z} = \frac{\partial X}{\partial z}\frac{\partial}{\partial X} + \frac{\partial Z}{\partial z}\frac{\partial}{\partial Z} = \frac{1}{f}\frac{\partial V_g}{\partial z}\frac{\partial}{\partial X} + \frac{\partial}{\partial Z} \quad ,$$

where ζ is the absolute vorticity and f the coriolis parameter. Then

$$\frac{\partial V_g}{\partial x} = \frac{\zeta}{f}\frac{\partial V_g}{\partial X} \quad ,$$

adding f on both sides, we have

$$\zeta = f\left(1 - \frac{1}{f}\frac{\partial V_g}{\partial X}\right)^{-1} \tag{4.2} \quad .$$

Also,

$$\frac{\partial V_g}{\partial z} = \frac{1}{f}\frac{\partial V_g}{\partial z}\frac{\partial V_g}{\partial X} + \frac{\partial V_g}{\partial Z} \quad ,$$

$$\left(1-\frac{1}{f}\frac{\partial V_g}{\partial X}\right)\frac{\partial V_g}{\partial z}=\frac{\partial V_g}{\partial Z} \quad ,$$

$$\frac{\partial V_g}{\partial z}=\frac{\zeta}{f}\frac{\partial V_g}{\partial Z} \quad .$$

Then

$$\frac{\partial}{\partial z}=\frac{\zeta}{f^2}\frac{\partial V_g}{\partial Z}\frac{\partial}{\partial X}+\frac{\partial}{\partial Z} \qquad (4.3) \quad .$$

The thermal wind relationship in physical coordinates is

$$f\frac{\partial V_g}{\partial z}=\frac{g}{\theta_0}\frac{\partial \theta}{\partial x} \quad .$$

After the transformation, it becomes

$$f\frac{\partial V_g}{\partial Z}=\frac{g}{\theta_0}\frac{\partial \theta}{\partial X} \quad ,$$

i.e. it remains unchanged from that in physical coordinates. From this relationship, there exists a function Φ such that

$$fV_g=\frac{\partial \Phi}{\partial X} \quad , \quad \frac{g}{\theta_0}\theta=\frac{\partial \Phi}{\partial Z} \quad ,$$

thus

$$V_g=\frac{1}{f}\frac{\partial \Phi}{\partial X} \quad , \quad \theta=\frac{\theta_0}{g}\frac{\partial \Phi}{\partial Z} \quad . \qquad (4.4)$$

In physical coordinates,

$$V_g = \frac{1}{f}\frac{\partial \phi}{\partial x} \quad , \quad \theta = \frac{\theta_0}{g}\frac{\partial \phi}{\partial z} \quad ,$$

where ϕ is the geopotential, from both equations of θ in the two coordinates, it shows that

$$\frac{\partial \phi}{\partial z} = \frac{\partial \Phi}{\partial Z} \quad .$$

Using this transformation,

$$\frac{\partial \phi}{\partial X} = \frac{f}{\zeta}\frac{\partial \phi}{\partial x} = \frac{f^2}{\zeta}V_g \quad ,$$

$$\frac{\partial \phi}{\partial z} = \frac{\zeta}{f^2}\frac{\partial V_g}{\partial Z}\frac{\partial \phi}{\partial X} + \frac{\partial \phi}{\partial Z} = \frac{f^2}{\zeta}V_g\frac{\zeta}{f^2}\frac{\partial V_g}{\partial Z} + \frac{\partial \phi}{\partial Z} \quad ,$$

$$= V_g\frac{\partial V_g}{\partial Z} + \frac{\partial \phi}{\partial Z} = \frac{\partial \Phi}{\partial Z} \quad ,$$

so, the modified geopotential Φ is

$$\Phi = \phi + \frac{1}{2}V_g^2 \qquad (4.5) \quad .$$

In our case the total flow is composed of a deformation field, with amplitude 2α, and ageostrophic velocities u_a:

$$U_T = -\alpha x + u_a \quad , \quad V_T = \alpha y + V_g \quad , \quad W = w$$

where V_g is the geostrophic wind from thermal wind balance

$$\frac{\partial V_g}{\partial Z} = \frac{g}{f\theta_0}\frac{\partial \theta}{\partial X} \quad .$$

For two dimensional flow, we can assume that parameters are independent of y (Y), which means that the geostrophic wind in the x (X) direction is constant with height.

The continuity equation in physical space is

$$\frac{\partial u_a}{\partial x}+\frac{\partial w}{\partial z}=0 \quad ,$$

where u_a is the horizontal ageostrophic velocity and w the vertical velocity. Thus there exists a streamfunction ψ, for which

$$u_a=\frac{\partial \psi}{\partial z} \qquad , \qquad w=-\frac{\partial \psi}{\partial x} \quad .$$

In geostrophic coordinates

$$u_a=\frac{\zeta}{f^2}\frac{\partial V_g}{\partial Z}\frac{\partial \psi}{\partial X}+\frac{\partial \psi}{\partial Z} \qquad , \qquad w=-\frac{\zeta}{f}\frac{\partial \psi}{\partial X} \tag{4.6}$$

4.2 The Governing Equations and Boundary Conditions

The equations in geostrophic coordinates are

$$\frac{dq}{d\tau}=\frac{\zeta}{\rho}\frac{\partial S}{\partial Z} \tag{4.7}$$

$$\rho\frac{\partial}{\partial Z}\left(\frac{1}{\rho}\frac{\partial \psi}{\partial Z}\right)+\frac{\partial}{\partial X}\left(q\frac{\rho g}{f^3\theta_0}\frac{\partial \psi}{\partial X}\right)=-2Q-\frac{\rho g}{f^2\theta_0}\frac{\partial S}{\partial X} \tag{4.8}$$

$$\frac{\partial^2 \Phi}{\partial X^2}+\frac{f^3\theta_0}{q\rho g}\frac{\partial^2 \Phi}{\partial Z^2}=f^2 \tag{4.9}$$

where

$$q = \frac{\zeta}{\rho}\frac{\partial\theta}{\partial Z} \quad , \qquad S = \frac{d\theta}{d\tau} \quad , \qquad Q = \rho\frac{\alpha}{f}\frac{\partial V_g}{\partial Z} \quad .$$

Here q is potential vorticity, S the source term, and Q the geostrophic forcing of frontogenesis. A pseudo density $r(z)$ has been introduced by Hoskins and Bretherton, where

$$r(z) = \rho_0\left(\frac{p}{p_0}\right)^{1-\kappa} = \rho_0\left(1-\frac{z}{z_a}\right)^{\frac{1-\kappa}{\kappa}} \quad .$$

For the Boussinesq approximation in our equations $r(Z) = r(z_0) = \rho$. In our calculation, the upper boundary condition $w = 0$ will be imposed at a geopotential surface $z = H$. The errors induced by the artificial lid and the Boussinesq approximation are small (Hoskins and Bretherton ,1972).

The source term S following the motion is approximated as

$$S = -\frac{L_v}{C_p\Pi}\frac{dr_{vs}}{d\tau} \qquad for \quad w \geq 0$$

$$= -E_r \qquad for \quad w < 0 \qquad (4.10)$$

where

$$\Pi = \left(\frac{\overline{p}}{p_0}\right)^{\kappa} \quad , \quad \overline{(\ )} = \frac{\int(\ )dX}{\int dX} \quad .$$

r_{vs} is the saturation mixing ratio of water vapor and E_r is the rate of evaporation.

We will replace Π by a constant value Π_0, this assumption is equivalent to the height independence of γ (= $\Gamma_m/\Gamma_d^* q_e/q_0$) in the evolution of potential vorticity (Emanuel et. al. 1987)

$$\frac{dq_g}{dt} = \frac{\zeta}{f}\frac{\partial}{\partial Z} w^* \left(q_g - \frac{\Gamma_m}{\Gamma_d} q_e \right) \qquad (4.11) \quad ,$$

where $w^* = -\partial\psi/\partial X$.

In the ascent regions where the slantwise convection has occurred the critical parameter γ will be kept as a small constant. Following Emanuel et. al. (1987), the source term can be expressed as

$$S \approx \frac{w^*}{f}\left(q - \frac{\Gamma_m}{\Gamma_d} q_e \right) \qquad for \quad r_v \geq r_{vs}$$

$$= 0 \qquad for \quad r_v < r_{vs} \qquad (4.12),$$

in which the latent heating only occurs for the ascending parcel in the saturated region. Thus, the time rate of change of potential vorticity (4.7) becomes

$$\frac{dq}{d\tau} = \frac{\zeta}{\rho f}\frac{\partial}{\partial Z} w^* \left(q - \frac{\Gamma_m}{\Gamma_d} q_e \right) \qquad for \quad r_v \geq r_{vs}$$

$$= 0 \qquad for \quad r_v < r_{vs} \qquad (4.13),$$

and (4.8) becomes

$$\rho \frac{\partial}{\partial Z}\left(\frac{1}{\rho}\frac{\partial \psi}{\partial Z} \right) + \frac{\partial}{\partial X}\left(\bar{q}\frac{\rho g}{f^3 \theta_0}\frac{\partial \psi}{\partial X} \right) = -2Q \qquad for \quad w > 0 \qquad (4.14),$$

where,

$$\tilde{q} = \frac{\Gamma_m}{\Gamma_d} q_e \qquad for \quad r_v \geq r_{vs}$$

$$= q \qquad for \quad r_v < r_{vs} \quad .$$

The change of potential temperature in descent due to evaporation can be calculated from

$$S = \frac{d\theta}{d\tau} \cong \frac{-L_v}{C_p \Pi_0} E_r \qquad (4.15).$$

Thus the change of potential vorticity in the descent region is

$$\frac{dq}{d\tau} = \frac{\zeta}{\rho} \frac{\partial S}{\partial Z} = -\frac{\zeta L_v}{\rho C_p \Pi_0} \frac{\partial E_r}{\partial Z} \qquad for \quad w \leq 0 \quad (4.16).$$

and (4.8) becomes

$$\rho \frac{\partial}{\partial Z}\left(\frac{1}{\rho}\frac{\partial \psi}{\partial Z}\right) + \frac{\partial}{\partial X}\left(q \frac{\rho g}{f^3 \theta_0} \frac{\partial \psi}{\partial X}\right) = -2Q + \frac{\rho g L_v}{f^2 \theta_0 C_p \Pi_0} \frac{\partial E_r}{\partial X} \qquad for \quad w \leq 0 \quad (4.17).$$

The boundary condition for solving the streamfunction ψ are

$$\psi = 0$$

on all boundaries ($u_a = 0$ on lateral boundaries and $w = 0$ on horizontal boundaries),

The diabatic source term S can produces sources and sinks of potential vorticity. The dry and moist cases with zero total boundary flux of potential vorticity, there is no diabatic forcing on the horizontal boundaries, which means that only the geostrophic forcing can

affect the temperature distribution on the horizontal boundaries. However, in the case with evaporation at the surface, both the geostrophic forcing and the diabatic effects will affect the temperature distribution at the bottom boundary.

For dry simulations and simulations with condensational heating, the boundary conditions due to the geostrophic forcing which satisfy the thermodynamic equation

$$\frac{d\theta}{d\tau} = 0 \quad ,$$

are

$$\Phi_z = \frac{g}{\theta_0}\frac{2\Delta\theta}{\pi}\tan^{-1}\left(\frac{X}{L}\right) \tag{4.18}$$

on bottom boundary, and from Hoskins and Bretherton (1972),

$$\theta(Z_{top}) = \theta(Z_0) + \frac{1}{f}\int \rho q_0 dz \quad .$$

Since we have an initially uniform q field, it follows that

$$\Phi_z = \frac{g}{\theta_0}\left[\frac{2\Delta\theta}{\pi}\tan^{-1}\left(\frac{X}{L}\right) + \frac{\rho q_0 Z_{top}}{f}\right] \tag{4.19}$$

on the top boundary,

$$\Phi = g\frac{\Delta\theta}{\theta_0}\left(Z - \frac{H}{2}\right) + \frac{\rho g q_0 Z^2}{\theta_0 f}\frac{}{2} \tag{4.20} \quad ,$$

on the right lateral boundary, and

$$\Phi = -g\frac{\Delta\theta}{\theta_0}\left(Z - \frac{H}{2}\right) + \frac{\rho g q_0 Z^2}{\theta_0 f}\frac{}{2} \tag{4.21} \quad ,$$

on the left lateral boundary.

With no diabatic forcing on the horizontal boundaries, the θ distribution will be given with $L = L_0 \exp(-\alpha T)$ from the Φ field. The initial values of L, q and $\Delta\theta$ are

$$L_0 = 380km\ , \quad q_0 = 2.67 \times 10^{-7} m^2 s^{-1} K kg^{-1}\ , \quad \Delta\theta = 10K\ .$$

The constant deformation rate $\alpha = 1 \times 10^{-5}\ S^{-1}$. The reference values at the surface are p_0 = 1000mb, θ_0 = 288 K and ρ_0 = 1.0 kg/m³.

In the case with evaporation, following Seitter and Kuo (1983), the evaporation should be allowed to happen at surface in order to prevent a super adiabatic layer generated right above the surface. So the boundary condition of θ distribution along the horizontal boundaries become

$$\frac{\partial\theta}{\partial\tau} + U\frac{\partial\theta}{\partial X} = -\frac{L_v}{C_p \Pi_0} E_r \quad , \qquad at \quad Z = 0 \quad (4.22)$$

$$\frac{\partial\theta}{\partial\tau} + U\frac{\partial\theta}{\partial X} = 0 \quad . \qquad at \quad Z = Z_{top} \quad (4.23)$$

equations (4.18) and (4.19) served as the initial θ distribution on horizontal boundaries.

4.3 The Mixing Ratio of Liquid Water

In the descent region, which is unsaturated, the major heat sink comes from evaporation. The governing equations of liquid water content are taken from Kessler (1969) and Klemp and Wilhelmson (1978). The terminal velocity and the rate of evaporation depend on the amount of liquid water content ($\overline{\rho r_l}$), and are not constant as in Seitter and Kuo

(1983). The equation for liquid water content is

$$\frac{dr_l}{dt}-\frac{1}{\bar{\rho}}\frac{\partial}{\partial z}(\bar{\rho}V_T r_l)=-\frac{dr_{vs}}{dt} \qquad w\geq 0$$

$$=-E_r \qquad w<0 \qquad (4.24),$$

here V_T is the terminal velocity of raindrops, E_r the rate of evaporation and r_l the mixing ratio of liquid water. After the coordinate transformation, it becomes

$$\frac{dr_l}{d\tau}-\left(\frac{\zeta}{\bar{\rho}f^2}\frac{\partial V_g}{\partial Z}\frac{\partial}{\partial X}+\frac{1}{\bar{\rho}}\frac{\partial}{\partial Z}\right)\bar{\rho}V_T r_l=-\frac{dr_{vs}}{dt} \qquad w\geq 0$$

$$=-E_r \qquad w<0 \qquad (4.25),$$

Again the major change in r_{vs} is due to the vertical advection along M surfaces, thus in the ascent region

$$\frac{dr_l}{d\tau}=\left(\frac{\zeta}{\bar{\rho}f^2}\frac{\partial V_g}{\partial Z}\frac{\partial}{\partial X}+\frac{1}{\bar{\rho}}\frac{\partial}{\partial Z}\right)\bar{\rho}V_T r_l-w\frac{\partial r_{vs}}{\partial Z} \qquad for \quad w\geq 0 \quad (4.26),$$

and in the descent region

$$\frac{dr_l}{d\tau}=\left(\frac{\zeta}{\bar{\rho}f^2}\frac{\partial V_g}{\partial Z}\frac{\partial}{\partial X}+\frac{1}{\bar{\rho}}\frac{\partial}{\partial Z}\right)\bar{\rho}V_T r_l-E_r \qquad for \quad w<0 \quad (4.27).$$

Follow Thorpe and Emanuel (1985), we have

$$\frac{\partial r_{vs}}{\partial Z}=(q_e-q)\frac{C_p\Pi_0\rho}{L_v\zeta} \quad .$$

So (4.26) becomes

$$\frac{dr_l}{d\tau}=\left(\frac{\zeta}{\bar{\rho}f^2}\frac{\partial V_g}{\partial Z}\frac{\partial}{\partial X}+\frac{1}{\bar{\rho}}\frac{\partial}{\partial Z}\right)\bar{\rho}V_T r_l+w(q-q_e)\frac{C_p\Pi_0\rho}{L_v\zeta} \quad for \quad w\geq 0 \quad (4.28).$$

We will let the water fall "through" the ground but allow no water comes at the top boundary (Seitter and Kuo, 1983), thus the boundary conditions for the mixing ratio of liquid water are

$$\frac{\partial r_l}{\partial \tau} = \left(\frac{\zeta}{\bar{\rho} f^2} \frac{\partial V_g}{\partial Z} \frac{\partial}{\partial X} + \frac{1}{\bar{\rho}} \frac{\partial}{\partial Z} \right) \bar{\rho} V_T r_l - E_r \quad , \qquad at \quad Z = 0 \quad (4.29)$$

$$r_l = 0 \quad . \qquad at \quad Z = Z_{top} \quad (4.30)$$

Equations (4.27), (4.28), (4.29) and (4.30) serve as the governing equation of mixing ratio of liquid water as time integration proceed.

4.4 The Mixing Ratio of Water Vapor

In order to control the rate of evaporation, we need a prognostic equation for the mixing ratio of water vapor as time integration proceed. In the ascent region, in which it is saturated, $r_v = r_{vs}$. In the descent region, the equation for mixing ratio of water vapor is

$$\frac{dr_v}{d\tau} = E_r \qquad (4.31)$$

The initial condition for r_v is $r_v = r_{vs}$ in the ascent region which is always saturated. In descent region which is unsaturated the initial condition of r_v is equivalent to relative humidity equals to 70%.

4.5 The Rate of Evaporation and Terminal Velocity

The rate of evaporation and equation for terminal velocity (Klemp and Wilhelmson ,1978) are

$$E_r = \frac{1}{\bar{\rho}} \frac{(1 - r_v/r_{vs}) C (\bar{\rho} r_l)^{0.525}}{5.4 \times 10^5 + 2.55 \times 10^6 / \bar{p}\, r_{vs}} \qquad (4.32),$$

where

$$C = 1.6 + 124.9(\bar{\rho} r_l)^{0.2046} \qquad (4.33),$$

$$r_{vs} = \frac{3.8}{\bar{p}} \exp\left(17.27 \frac{T - 273}{T - 36}\right) \qquad (4.34).$$

The terminal velocity V_T is

$$V_T = 36.34(\bar{\rho} r_l)^{0.1364} \left(\frac{\bar{\rho}}{\rho_0}\right)^{-0.5} \quad (m/\sec) \qquad (4.35).$$

The unit of $\bar{\rho}$ in (4.32), (4.33) and (4.35) is gm/cm³, and the unit of pressure in (4.32) and (4.34) is *mb*.

4.6 Model Summary

The relaxation method has been used to solve the elliptic equations (4.9), (4.14) and (4.17). The time scheme used here is a leapfrog scheme, with centered differences as the space scheme. The grid spacing is 40km in the X direction and 250m in the Z direction. In order to satisfy the stable criteria of numerical simulation, the time step for the integration of the dry simulations and simulations with condensation only is 60 sec, and 20 sec for simulation with evaporative cooling.

There is a neutral computational mode which will grow in the nonlinear equation and cause errors using the leapfrog scheme for time integration. For suppressing the computational mode, use a first order accurate (two-level) scheme, e.g. Euler scheme, once after applying the leapfrog scheme several times (Mesinger and Arakawa, 1976). During the model simulation we did find that the growing computational mode affects the results. Thus we use the Euler scheme every 5 time steps to smooth out the computational mode.

Following Thorpe and Emanuel (1985), the dry run of this model is initialized with constant potential vorticity. Without condensational heating, potential vorticity is constant $q = q_0$ throughout the time integration, and the changes of various fields are due to the geostrophic forcing field. The moist run of this model is run initially with a specified constant potential vorticity field. When the time integration proceed the critical number γ decrease from 1 to 0.07 in one hour, then it was held as a constant in the ascent region. The variation of potential vorticity of moist run with condensational heating only is calculated from (4.13). The result are resemble to that of Thorpe and Emanuel (1985).

The simulations with evaporation are similar to moist run except incorporated evaporation in the decent regions. In the study of Seitter and Kuo (1983), the evaporation allows to occur only when the relative humidity is less or equal to 90%. The criteria of our standard run (E_r) is equivalent to relative humidity equal to 85%. The variation of potential vorticity in the descent region duo to evaporation is from equation (4.16).

Chapter 5 : Results and Discussions

The numerical simulations include a case without diabatic heating (dry case or case-D), one with condensational heating only (moist case or case-C) and a third with both condensational heating and evaporative cooling (evapor case or case-E). Tables 5.1, 5.2 and 5.3 list the maximum or minimum value of parameters at 6 hour intervals up to 24 hour for the case-D, case-C and case-E respectively.

Where there are two lines in some of the columns, the number in the upper line denotes the maximum or minimum value along the upper boundary, while the number on the lower line denotes the maximum or minimum value along the lower boundary, except in the column of vertical velocity. The value of vertical velocity in the upper line denotes the maximum value of descent while the value on the lower line denotes the maximum of ascent. In case-E the second value in the upper line means the maximum downdraft induced by evaporation in the lower portion of atmosphere. The number in the columns of streamfunction and condensational heating rate denotes the maximum or minimum value in the interior of the domain.

The initial conditions are shown in figure 5.1. After one day of simulation, the results of the case-D, case-C and case-E are shown in figures 5.2, 5.3 and 5.4. The maximum or minimum value of parameters at 24 hour included initial condition are shown in Table 5.4. In 24 hours the cyclonic vorticity grows from 0.28 to 2.1 f in the case-D, from 0.28 to 11.52 f

in the case-C and from 0.28 to 28.72 f in the case-E. The anticyclonic vorticity grows from -0.21 to -0.42 f in the case-D, from -0.21 to -0.44 f in the case-C and from -0.21 to -0.60 f in the case-E.

The asymmetry between the upper boundary and lower boundary occurs in almost every figure in the case-C and in the case-E. Since there is evaporative cooling on the lower boundary, the redistribution of temperature changes the geostrophic forcing. The increasing geostrophic forcing increases the ageostrophic wind, the convergence of ageostrophic wind near front accelerates the secondary circulation, thus increasing the maximum upward velocity. The frontal collapse (as $\zeta \to \infty$, since $\partial V_g/\partial X$ will not equal f exactly in our calculation, so vorticity becomes negative is our criterion for frontal collapse) is faster in the case-E than that in the case-C. From table 5.4, the maximum absolute vorticity in the case-E at the lower boundary is about 4.5 times that at the upper boundary, while it is about 3 times that in the case-C. The values of the along-front velocity , geostrophic forcing and ageostrophic velocity at lower boundary are greater than those at the upper boundary.

Figure 5.4 shows that the temperature gradient near the front in the case-E is greater than that in the case-C after 24 hours. The cyclonic vorticity in the mid layer is enhanced due to evaporation. The maximum downdraft moves toward the lower portion of the atmosphere where the maximum evaporation occurs. This agree with the description by Srivastava (1987) and Seitter and Kuo (1983), in which the strong downdraft is mainly driven by evaporative cooling. Comparing figures 5.1, 5.2, 5.3 and 5.4, the condensational heating results in a concentrated sloping updraft along the frontal zone (Emanuel, 1985), and the evaporative cooling results in a concentrated sloping downdraft along the frontal zone

toward the cold air side of the front. In the case-C the maximum potential vorticity at the lower boundary generated by condensational heating could result in baroclinic instability. A similar situation is found in the case-E where many local maximum and minimum of potential vorticity occur along the lower boundary. Thus the sharp gradient of potential vorticity could result in more baroclinic instability. With the evaporative cooling at the lower boundary, a positive increase of potential vorticity through out the domain is expected.

Some sensitivity tests have been performed to check the effect of evaporation on frontogenesis. In the case *Er/10* the rate of evaporation is one tenth that of the standard run (case-E). In the case *Er*10* the rate of evaporation is ten times that of the standard run. The results are shown in figures 5.5 and 5.6. The maximum and minimum value at 6 hours interval are shown in tables 5.5 and 5.6. The comparison of these three cases at 24 hours is shown in table 5.7. Increasing the rate of evaporation enhances the frontogenesis. In the case *RH75* the critical relatively humidity for allowing evaporation is change from 85% to 75%. In the case *RH95* the critical relative humidity is change from 85% to 95%. In the case *RH75* the frontal collapse at 1 day 1 hour 21 minutes and 20 seconds, and at 23 hours 41 minutes and 20 seconds in the case *RH95*. These tests show that frontogenesis is enhanced with larger rate of evaporation. The time of frontal collapse strongly depended on the initial condition, which is dependent on the initial temperature gradient.

From tables 5.2 to 5.4, the frontogenesis accelerates much faster in the last 6 hours period. This is resemble to the results in the study of latent heat release in the extratropical cyclone by Smith et. al. (1984), which in the early stage cyclone's evolution is dominated by dry dynamical process, and the cyclone's evolution is dominated by the latent heat release

from midway to final stage. The diabatic effects on frontogenesis is much more significant than the geostrophic forcing (in dry case) on frontogenesis. From tables 5.4 and 5.8 the evaporative effect seems to be less significant than condensational heating on frontogenesis, however, in the case with evaporation the frontal collapse is faster.

Srivastava (1987), studying microbursts, uses a model similar to that of his 1985 paper but included the downdraft driven by the melting of ice particles. The calculations showed that precipitation in the form of ice crystals will increase the intensity of downdrafts over that with rain water alone. When the thermal stratification is increased, an intense downdraft requires a rather high concentration of precipitation but can be facilitated by the presence of ice. In the presence of precipitation with fractional content of ice particles, it is easy to drive the same intense downdraft with a smaller concentration of precipitation at the top of the downdraft.

In his study, under typical atmospheric conditions, ice particles of a few millimeters in diameter can melt completely in a fall through a few kilometers of above melting temperature, while raindrops of the same size can not evaporate completely under similar conditions. Even though the latent heat of melting is much smaller than that of evaporation, the heat lost by the environment to a melting particle can be substantially larger than to a raindrop of the same mass. Therefore, ice particles are potentially important for generating intense downdrafts by cooling the atmosphere. It appears that the melting effect of ice crystals might be a important mechanism in driving the downdraft. Thus a study including melting effects should be performed in the future to improve the understanding of diabatic effects on frontogenesis, and on related problems.

Chapter 6 : Summary and Conclusion

Geostrophic forcing used to be invoked as the primary factor that forces frontogenesis, while diabatic effects were treated as enhancing the frontal structure. Comparisons of moist and dry models of baroclinic instability show that the moist cyclone tends to develop faster, with a shorter horizontal scale than that of the dry cyclone.

Many investigations of the characteristics of disturbances growing in an environment of near neutrality to slantwise convection have been done. The importance of diabatic effects on frontogenesis has been demonstrated in some of these studies.

Evaporation has been found to be an important mechanism for maintaining and intensifying the downdraft in some studies too. The numerical simulations show that the acceleration of secondary circulations associated with the frontal system due to either condensational heating or evaporative cooling did enhance the convergence near the front. Although the effect of evaporation is less significant as compare with condensational heating, it did help to accelerate the secondary circulation. The local maxima of potential vorticity due to latent heat release might meet the necessary condition for secondary baroclinic instability, a condition which may also arise due to evaporation.

The study of frontogenesis is also related to the studies of cyclonic development and baroclinic instability, thus we feel that it would be interesting to study baroclinic waves development in the presence of diabatic heating or cooling, and problems related to it. The

effects of unstable moist stratification (i.e., $q_{ge} < 0$) on developing baroclinic waves, and effects such as evaporation of ice, surface friction, surface heat fluxes, and three-dimensionality remain to be explored in future work.

Reference

Emanuel, K. A. : Observational evidence of slantwise convective adjustment.

Emanuel, K. A. : Large-scale and mesoscale circulation in convectively adjusted atmosphere.

Emanuel, K. A., 1983: The lagrangian parcel dynamics of moist symmetric instability. *J Atmos. Sci.*, **40,** 2369-2376.

Emanuel, K. A., 1985: Frontal circulations in the presence of small moist symmetric stability. *J. Atmos. Sci.*, **42,** 1062-1071.

Emanuel, K. A., 1986: Some dynamical aspects of precipitating convection. *J. Atmos. Sci.* **43,** 2183-2198.

Emanuel, K. A., M. Fantini and A. J. Thorpe, 1987: Baroclinic Instability in an environment of small stability to slantwise moist convection, Part I: Two-Dimensional models. *J. Atmos. Sci.*, **44,** 1559-1573.

Hoskins, B. J., 1971: Atmospheric frontogenesis model: some solution. *Quart. J. Roy. Meteor. Soc.*, **97,** 139-153.

Hoskins, B. J. and F. P. Bretherton, 1972: Atmospheric frontogenesis models: Mathematical formulation and solution. *J. Atmos. Sci.*, **29,** 11-37.

Hoskins, B. J., M. E. Mcintyre and A. W. Robertson, 1985: On the use and significance of isentropic potential vorticity maps. *Quart. J. Roy. Meteor. Soc.*, **111,** 877-916.

Kessler, E., 1969: On the distribution and continuity of water substance in atmospheric circulation. *Meteor. Monogr.*, **No.32,** *Amer. Meteor. Soc.*, 84 pp.

Klemp, J. B. and R. B. Wilhelmson, 1978: The simulation of three-dimensional convective storm dynamics. *J. Atmos. Sci.*, **35,** 1070-1096.

Klemp, J. B. and R. B. Wilhelmson, 1978: Simulation of right- and left-moving storms produced through storm splitting. *J. Atmos. Sci.*, **35,** 1097-1110.

Reed, R. J. and F. Sanders, 1955: An investigation of the development of a mid-tropospheric frontal zone and its associated vorticity field. *J. Meteor.*, **10,** 338-349.

Sanders, F., 1955: An investigation of the structure and dynamic of an intense surface frontal zone. *J. Meteor.*, **12,** 542-552.

Sanders, F. and L. F. Bosart,1985: Mesoscale structure in the megalopolitan snowstorm of 11-12 February 1983, Part I: Frontogenetical forcing and symmetric instability. *J. Atmos. Sci.*, **42,** 1050-1061.

Sawyer, J. S., 1956: The vertical circulation at meteorological fronts and its relation to frontogenesis. *Proc. Roy. Soc. London,* **A234,** 346-362.

Seitter, K. L. and K. -L. Kuo, 1983: The dynamical structure of squall-line type thunderstorms. *J. Atmos. Sci.*, **40,** 2831-2854.

Smith, P. J., P. M. Dare and S. -J. Lin, 1984: The impact of latent heat release on synoptic-scale vertical motion and development of an extratropical cyclone system. *Mon. Wea. Rev.* **112,** 2421-2430.

Srivastava, R. C., 1985: A simple model of evaporatively driven downdraft: Application to microburst downdraft. *J. Atmos. Sci.*, **42,** 1004-1023.

Srivastava, R. C., 1987: A model of intense downdrafts driven by the melting and evaporation of precipitation. *J. Atmos. Sci.*, **44,** 1752-1773.

Thorpe, A. J. and K. A. Emanuel, 1985: Frontogenesis in the presence of small stability to slantwise convection. *J. Atmos. Sci.*, **42,** 1809-1824.

Weisman, M. L., J. B. Klemp and R. Rotunno, 1988: Structure and evolution of numerically simulated squall lines. *J. Atmos. Sci.*, **45,** 1990-2013.

Figure and Table Legends

Figure 3.1 The distribution of *Pam-II* network stations.

Figure 3.2 The 3 hourly precipitation accumulation.

(3.2a) 3 hourly precipitation from 15 FEB 0000Z to 15 FEB 0255Z
(3.2b) 3 hourly precipitation from 15 FEB 0300Z to 15 FEB 0555Z
(3.2c) 3 hourly precipitation from 15 FEB 0600Z to 15 FEB 0855Z.

Figure 3.3 National Weather Service radar summary.

(3.3a) 14 FEB 2035Z Radar Summary.
(3.3b) 14 FEB 2135Z Radar Summary.
(3.3c) 14 FEB 2235Z Radar Summary.
(3.3d) 14 FEB 2335Z Radar Summary.
(3.3e) 15 FEB 0135Z Radar Summary.
(3.3f) 15 FEB 0235Z Radar Summary.
(3.3g) 15 FEB 0335Z Radar Summary.
(3.3h) 15 FEB 0435Z Radar Summary.
(3.3i) 15 FEB 0535Z Radar Summary.

Figure 3.4 The rate of evaporation (areas with +) calculated from *pam-II* data set. Unit: $10^{-7}s^{-1}$.

(3.4a) 14 FEB 2030Z, areas of evaporation (+) and the rate of evaporation. Heavy dash line is the border line of radar echo from Figure 3.3.
(3.4b) as that of 3.4a, except for 14 FEB 2130Z.
(3.4c) as that of 3.4a, except for 14 FEB 2230Z.
(3.4d) as that of 3.4a, except for 14 FEB 2330Z.
(3.4e) as that of 3.4a, except for 15 FEB 0030Z.
(3.4f) as that of 3.4a, except for 15 FEB 0130Z.

(3.4g) as that of 3.4a, except for 15 FEB 0230Z.

(3.4h) as that of 3.4a, except for 15 FEB 0330Z.

(3.4i) as that of 3.4a, except for 15 FEB 0430Z.

(3.4j) as that of 3.4a, except for 15 FEB 0530Z.

Figure 5.1 Initial condition. Cross section in x-z plane in physical space; the unit is km in both z and x direction.

(5.1a) potential temperature θ (°C).

(5.1b) Along front velocity V_g (ms^{-1}). $V_{gmax} = 21.22\ ms^{-1}$, $V_{gmin} = -21.22\ ms^{-1}$.

(5.1c) Absolute vorticity ζ ($10^{-4} s^{-1}$). $\zeta_{max} = 1.28 \times 10^{-4} s^{-1}$, $\zeta_{min} = 0.79 \times 10^{-4} s^{-1}$.

(5.1d) Geostrophic forcing Q ($10^{-4} kg\ m^{-3} s^{-1}$). $Q_{max} = 5.68 \times 10^{-4} kg\ m^{-3} s^{-1}$.

(5.1e) The x-derivative of geostrophic forcing $-Q_x$ (10^{-9} kg m^{-4} s^{-1}). $-Q_{x\ max} = 0.96 \times 10^{-9} kg\ m^{-4} s^{-1}$, $-Q_{x\ min} = -0.96 \times 10^{-9} kg\ m^{-4} s^{-1}$.

(5.1f) Streamfunction ψ ($10^3 kg\ m^{-1} s^{-1}$). $\psi_{max} = 7.77 \times 10^3 kg\ m^{-1} s^{-1}$.

(5.1g) Vertical velocity w ($cm\ s^{-1}$). $w_{max} = 0.60\ cm\ s^{-1}$, $w_{min} = -0.60\ cm\ s^{-1}$.

(5.1h) Ageostrophic velocity in the x-direction u_a ($m\ s^{-1}$). $u_{amax} = 3.42\ m\ s^{-1}$, $u_{amin} = -3.42\ m\ s^{-1}$.

Figure 5.2 Case-D, after one day of simulation. Cross section in x-z plane in physical space; the unit is km in both z and x direction.

(5.2a) potential temperature θ (°C).

(5.2b) Along-front velocity V_g (ms^{-1}). $V_{gmax} = 36.17\ ms^{-1}$, $V_{gmin} = -36.17\ ms^{-1}$.

(5.2c) Absolute vorticity ζ ($10^{-4} s^{-1}$). $\zeta_{max} = 3.10 \times 10^{-4} s^{-1}$, $\zeta_{min} = 0.58 \times 10^{-4} s^{-1}$.

(5.2d) Geostrophic forcing Q ($10^{-4} kg\ m^{-3} s^{-1}$). $Q_{max} = 13.25 \times 10^{-4} kg\ m^{-3} s^{-1}$.

(5.2e) The x-derivative of geostrophic forcing $-Q_x$ (10^{-9} kg m^{-4} s^{-1}). $-Q_{x\ max} = 4.93 \times 10^{-9} kg\ m^{-4} s^{-1}$, $-Q_{x\ min} = -4.93 \times 10^{-9} kg\ m^{-4} s^{-1}$.

(5.2f) Streamfunction ψ ($10^3 kg\ m^{-1} s^{-1}$). $\psi_{max} = 10.36 \times 10^3 kg\ m^{-1} s^{-1}$.

(5.2g) Vertical velocity w ($cm\ s^{-1}$). $w_{max} = 1.04\ cm\ s^{-1}$, $w_{min} = -1.04\ cm\ s^{-1}$.

(5.2h) Ageostrophic velocity in the x-direction u_a ($m\ s^{-1}$). $u_{amax} = 5.14\ m\ s^{-1}$, $u_{amin} = -5.14\ m\ s^{-1}$.

Figure 5.3 Case-C, after one day of simulation. Cross section in x-z plane in physical space; the unit is km in both z and x direction.

(5.3a) Potential temperature θ (°C).

(5.3b) Along-front velocity V_g (ms^{-1}). $V_{gmax} = 39.52\ ms^{-1}$, $V_{gmin} = -39.51\ ms^{-1}$.

(5.3c) Absolute vorticity ζ ($10^{-4} s^{-1}$). $\zeta_{max} = 12.52 \times 10^{-4} s^{-1}$, $\zeta_{min} = 0.56 \times 10^{-4} s^{-1}$.

(5.3d) Geostrophic forcing Q ($10^{-4} kg\ m^{-3} s^{-1}$). $Q_{max} = 13.18 \times 10^{-4} kg\ m^{-3} s^{-1}$.

(5.3e) The x-derivative of geostrophic forcing $-Q_x$ (10^{-9} kg m^{-4} s^{-1}). $-Q_{x\ max} = 4.97 \times 10^{-9} kg\ m^{-4} s^{-1}$, $-Q_{x\ min} = -4.97 \times 10^{-9} kg\ m^{-4} s^{-1}$.

(5.3f) Streamfunction ψ ($10^3 kg\ m^{-1} s^{-1}$). $\psi_{max} = 14.06 \times 10^3 kg\ m^{-1} s^{-1}$.

(5.3g) Vertical velocity w (cm s^{-1}). $w_{max} = 3.39$ cm s^{-1}, $w_{min} = -1.38$ cm s^{-1}.

(5.3h) Ageostrophic velocity in the x-direction u_a (m s^{-1}). $u_{amax} = 6.28$ m s^{-1}, $u_{amin} = -6.27$ m s^{-1}.

(5.3i) Potential vorticity q (10^{-7} m^2 °K s^{-1} kg^{-1}). $q_{max} = 19.30 \times 10^{-7}$ m^2 °K s^{-1} kg^{-1}, $q_{min} = 1.77 \times 10^{-7}$ m^2 °K s^{-1} kg^{-1}.

(5.3j) Condensational heating S at one day of moist simulation. $S_{max} = 8.12 \times 10^{-5}$ °K s^{-1}.

Figure 5.4 Case-E, after one day of simulation. Cross section in x-z plane in physical space; the unit is km in both z and x direction.

(5.4a) Potential temperature θ (°C).

(5.4b) Along-front velocity V_g (ms^{-1}). $V_{gmax} = 39.64\ ms^{-1}$, $V_{gmin} = -44.54\ ms^{-1}$.

(5.4c) Absolute vorticity ζ ($10^{-4} s^{-1}$). $\zeta_{max} = 29.72 \times 10^{-4} s^{-1}$, $\zeta_{min} = 0.40 \times 10^{-4} s^{-1}$.

(5.4d) Geostrophic forcing Q ($10^{-4} kg\ m^{-3} s^{-1}$). $Q_{max} = 19.34 \times 10^{-4} kg\ m^{-3} s^{-1}$.

(5.4e) The x-derivative of geostrophic forcing $-Q_x$ (10^{-9} kg m^{-4} s^{-1}). $-Q_{x\ max} = 12.33 \times 10^{-9} kg\ m^{-4} s^{-1}$, $-Q_{x\ min} = -13.89 \times 10^{-9} kg\ m^{-4} s^{-1}$.

(5.4f) Streamfunction ψ ($10^3 kg\ m^{-1} s^{-1}$). $\psi_{max} = 14.44 \times 10^3 kg\ m^{-1} s^{-1}$.

(5.4g) Vertical velocity w (cm s^{-1}). $w_{max} = 3.58$ cm s^{-1}, $w_{min} = -1.91$ cm s^{-1}.

(5.4h) Ageostrophic velocity in the x-direction u_a (m s^{-1}). $u_{amax} = 7.15$ m s^{-1}, $u_{amin} = -6.34$ m s^{-1}.

(5.4i) Potential vorticity q less than 2.5×10^{-7} m^2 °K s^{-1} kg^{-1}. $q_{min} = 1.77 \times 10^{-7}$ m^2 °K s^{-1} kg^{-1}, on the upper boundary.

(5.4j) Potential vorticity q larger than 3×10^{-7} m^2 °K s^{-1} kg^{-1}. $q_{max} = 27.53 \times 10^{-7}$ m^2 °K s^{-1} kg^{-1}.

(5.4k) Source term (heating or cooling rate). $S_{max} = 8.44 \times 10^{-5}$ °K s^{-1}.

Figure 5.5 Case Er/10, after one day of simulation. Cross section in x-z plane in physical space; the unit is km in both z and x direction.

(5.5a) Potential temperature θ (°C).

(5.5b) Along-front velocity V_g (ms^{-1}). $V_{gmax} = 39.55$ ms^{-1}, $V_{gmin} = -42.66$ ms^{-1}.

(5.5c) Absolute vorticity ζ (10^{-4} s^{-1}). $\zeta_{max} = 16.42 \times 10^{-4}$ s^{-1}, $\zeta_{min} = 0.49 \times 10^{-4}$ s^{-1}.

(5.5d) Geostrophic forcing Q (10^{-4} kg m^{-3} s^{-1}). $Q_{max} = 18.35 \times 10^{-4}$ kg m^{-3} s^{-1}.

(5.5e) The x-derivative of geostrophic forcing $-Q_x$ (10^{-9} kg m^{-4} s^{-1}). $-Q_{x\,max} = 10.66 \times 10^{-9}$ kg m^{-4} s^{-1}, $-Q_{x\,min} = -12.21 \times 10^{-9}$ kg m^{-4} s^{-1}.

(5.5f) Streamfunction ψ (10^3 kg m^{-1} s^{-1}). $\psi_{max} = 14.18 \times 10^3$ kg m^{-1} s^{-1}.

(5.5g) Vertical velocity w (cm s^{-1}). $w_{max} = 3.46$ cm s^{-1}, $w_{min} = -1.39$ cm s^{-1}.

(5.5h) Ageostrophic velocity in the x-direction u_a (m s^{-1}). $u_{amax} = 6.85$ m s^{-1}, $u_{amin} = -6.28$ m s^{-1}.

(5.5i) Potential vorticity q less than 2.5×10^{-7} m^2 °K s^{-1} kg^{-1}. $q_{min} = 1.77 \times 10^{-7}$ m^2 °K s^{-1} kg^{-1}, on the upper boundary.

(5.5j) Potential vorticity q larger than 3×10^{-7} m^2 °K s^{-1} kg^{-1}. $q_{max} = 21.91 \times 10^{-7}$ m^2 °K s^{-1} kg^{-1}.

(5.5k) Source term (heating or cooling rate). $S_{max} = 8.25 \times 10^{-5}$ °K s^{-1}.

Figure 5.6 Case Er*10, after one day of simulation. Cross section in x-z plane in physical space; the unit is km in both z and x direction.

(5.6a) Potential temperature θ (°C).

(5.6b) Along-front velocity V_g (ms^{-1}). $V_{gmax} = 39.55$ ms^{-1}, $V_{gmin} = -45.37$ ms^{-1}.

(5.6c) Absolute vorticity ζ (10^{-4} s^{-1}). $\zeta_{max} = 32.85 \times 10^{-4}$ s^{-1}, $\zeta_{min} = 0.43 \times 10^{-4}$ s^{-1}.

(5.6d) Geostrophic forcing Q (10^{-4} kg m^{-3} s^{-1}). $Q_{max} = 19.88 \times 10^{-4}$ kg m^{-3} s^{-1}.

(5.6e) The x-derivative of geostrophic forcing $-Q_x$ (10^{-9} kg m^{-4} s^{-1}). $-Q_{x\,max} = 13.16 \times 10^{-9}$ kg m^{-4} s^{-1}, $-Q_{x\,min} = -13.85 \times 10^{-9}$ kg m^{-4} s^{-1}.

(5.6f) Streamfunction ψ (10^3 kg m^{-1} s^{-1}). $\psi_{max} = 14.61 \times 10^3$ kg m^{-1} s^{-1}.

(5.6g) Vertical velocity w (cm s^{-1}). w_{max} = 3.65 cm s^{-1}, w_{min} = -4.24 cm s^{-1}.

(5.6h) Ageostrophic velocity in the x-direction u_a (m s^{-1}). u_{amax} = 7.54 m s^{-1}, u_{amin} = -6.35 m s^{-1}.

(5.6i) Potential vorticity q less than 2.5×10^{-7} m^2 °K s^{-1} kg^{-1}. $q_{min} = 1.78 \times 10^{-7}$ m^2 °K s^{-1} kg^{-1}, on the upper boundary.

(5.6j) Potential vorticity q larger than 3×10^{-7} m^2 °K s^{-1} kg^{-1}. $q_{max} = 27.61 \times 10^{-7}$ m^2 °K s^{-1} kg^{-1}.

(5.6k) Source term (heating or cooling rate). $S_{max} = 8.59 \times 10^{-5}$ °K s^{-1}.

Table 5.1 Dry case (case-D). The maximum or minimum values at the upper boundary, lower boundary or interior of atmosphere, in every 6 hours up to 24 hours.

Table 5.2 As that of table 5.1, except for moist case (Case-C).

Table 5.3 As that of table 5.1, except for evapor case (case-E). The second value at the upper line in the column of vertical velocity denotes the second maximum descent induced by evaporation.

Table 5.4 The data of initial condition and data of dry case (case-D), moist case (case-C) and evapor case (case-E) at hour 24.

Table 5.5 As that of 5.3, except with the rate of evaporation equal to one tenth of the rate of evaporation of case-D.

Table 5.6 As that of 5.3, except with the rate of evaporation equal to ten times the rate of evaporation of the case-D.

Table 5.7 The data of the case Er/10, the case-D (Er) and the case Er*10 at hour 24.

Table 5.8 The comparison of the time needed for front to collapse in different cases.

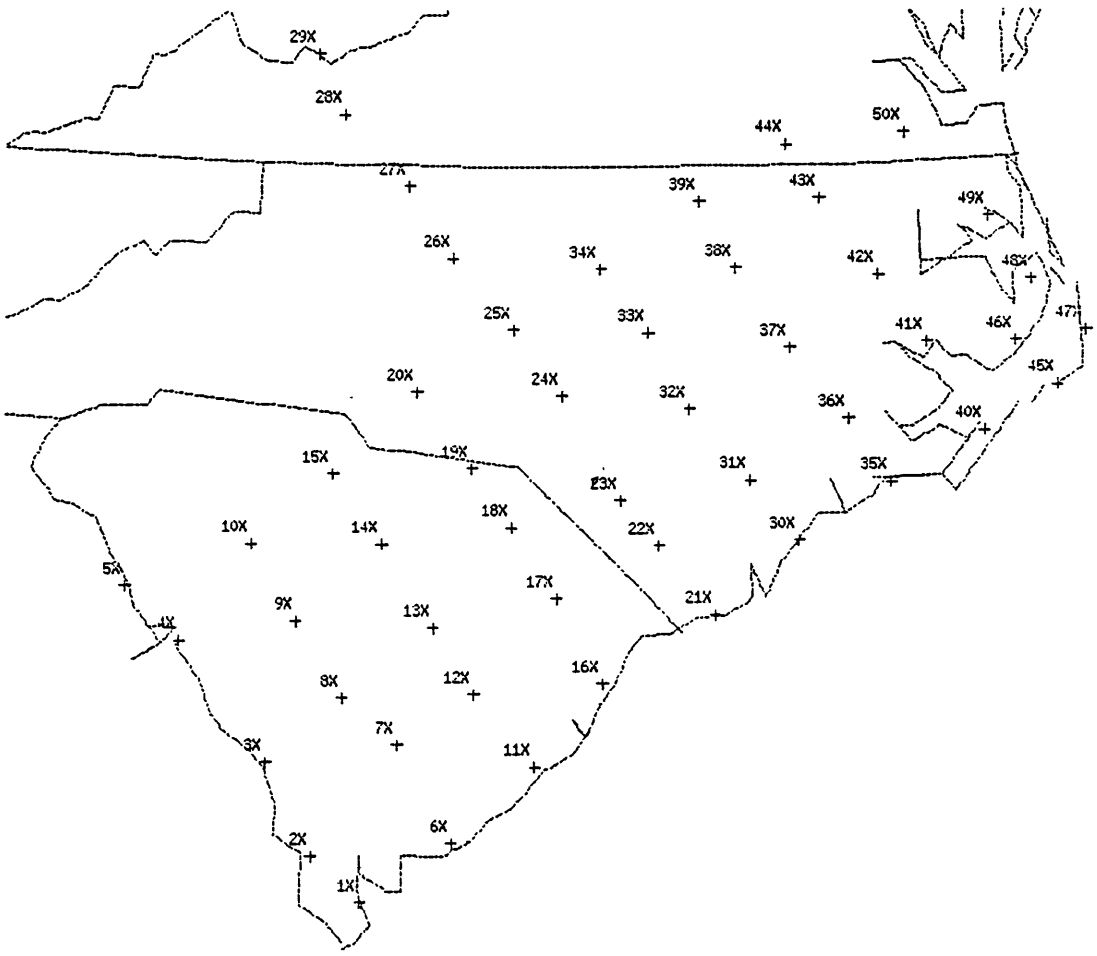

Figure 3.1 The distribution of *Pam-II* network stations.

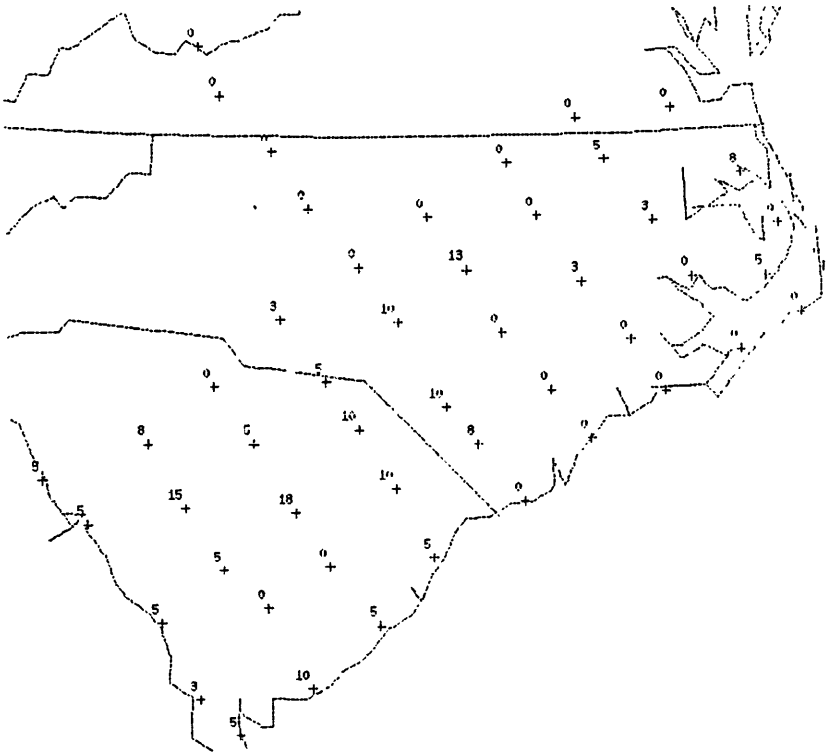

(3.2a) 3 hourly precipitation from 15 FEB 0000Z to 15 FEB 0255Z

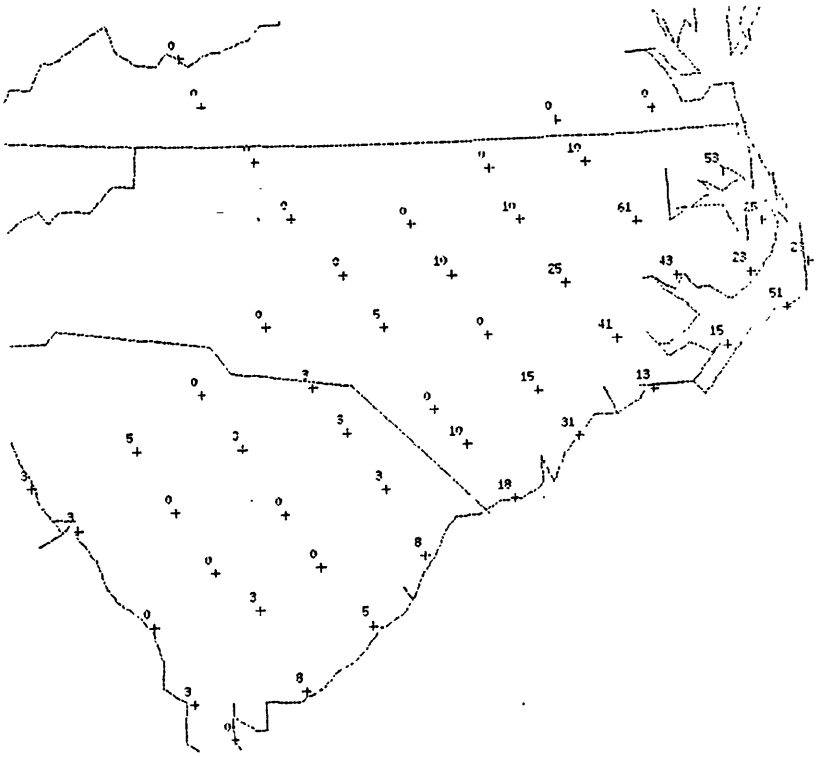

(3.2b) 3 hourly precipitation from 15 FEB 0300Z to 15 FEB 0555Z

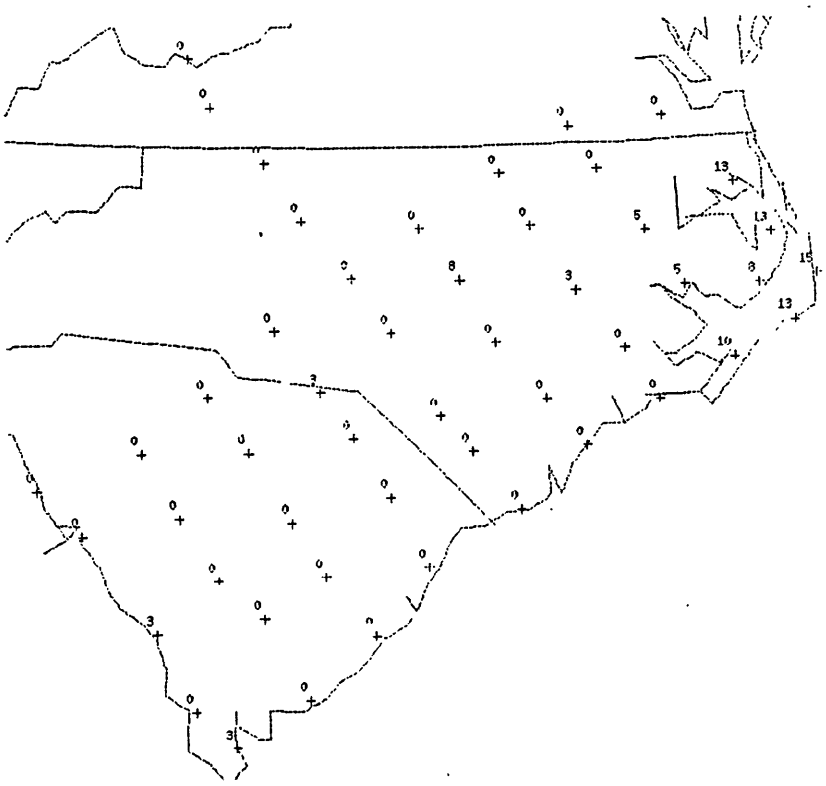

(3.2c) 3 hourly precipitation from 15 FEB 0600Z to 15 FEB 0855Z.

Figure 3.2 The 3 hourly precipitation accumulation.

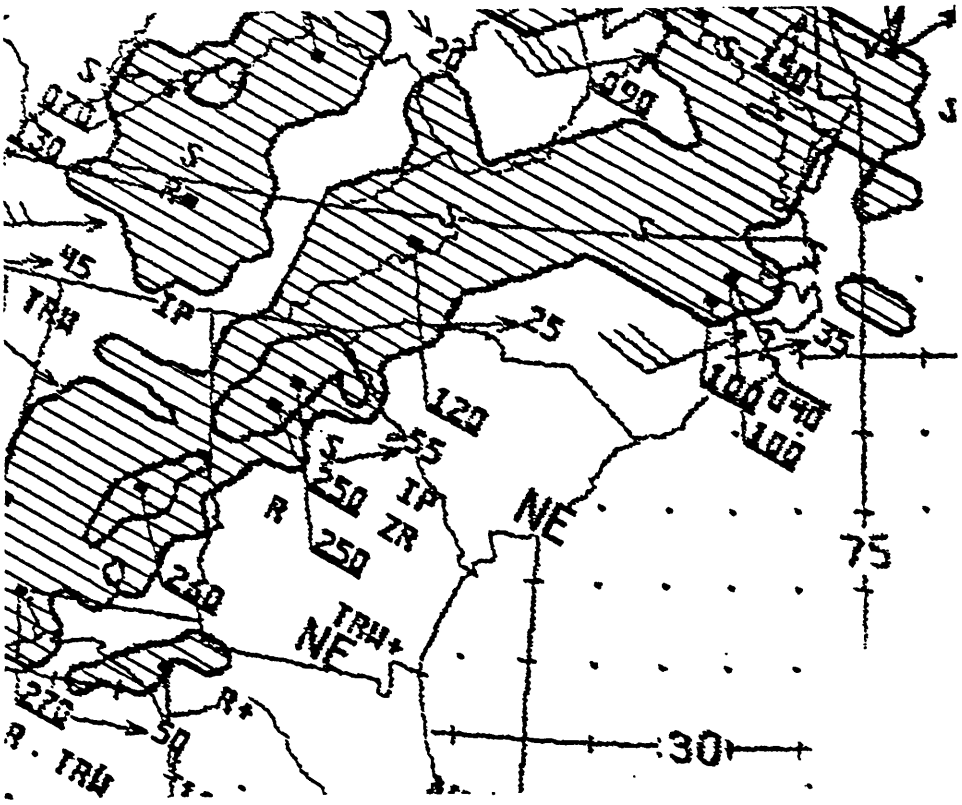

(3.3a) 14 FEB 2035Z Radar Summary.

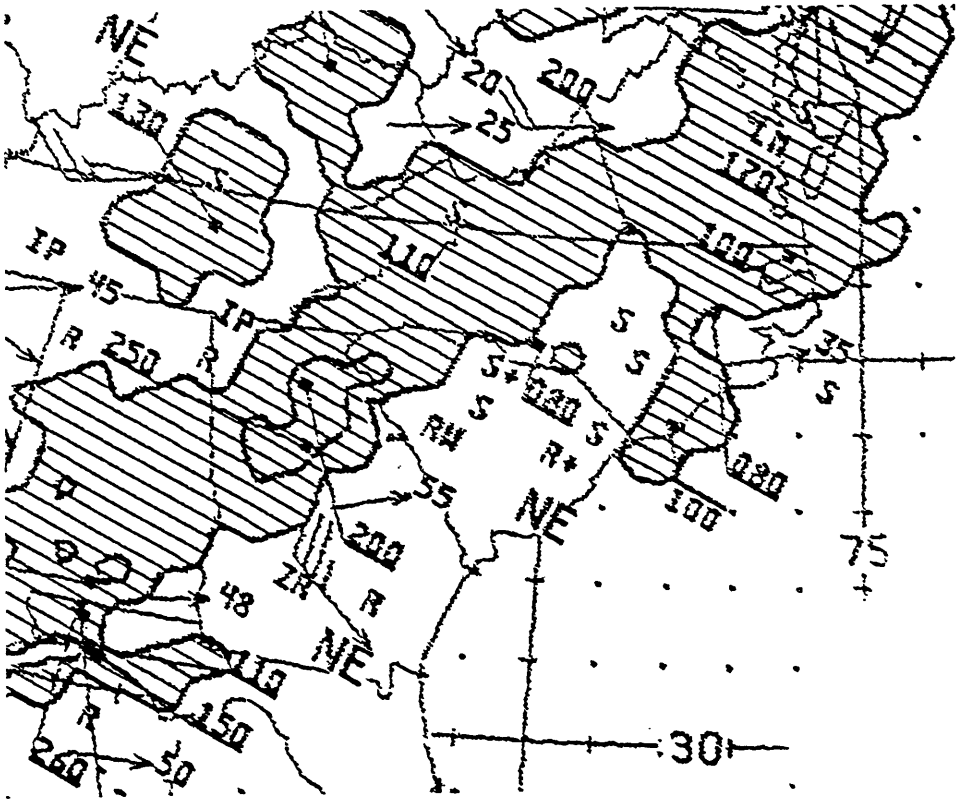

(3.3b) 14 FEB 2135Z Radar Summary.

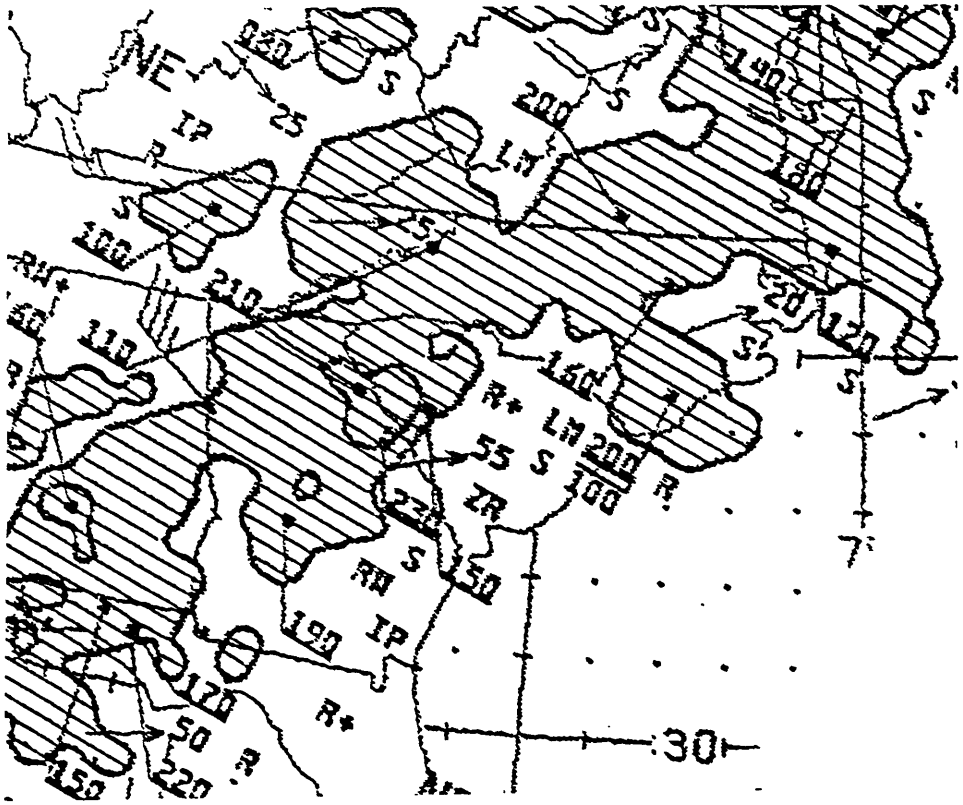

(3.3c) 14 FEB 2235Z Radar Summary.

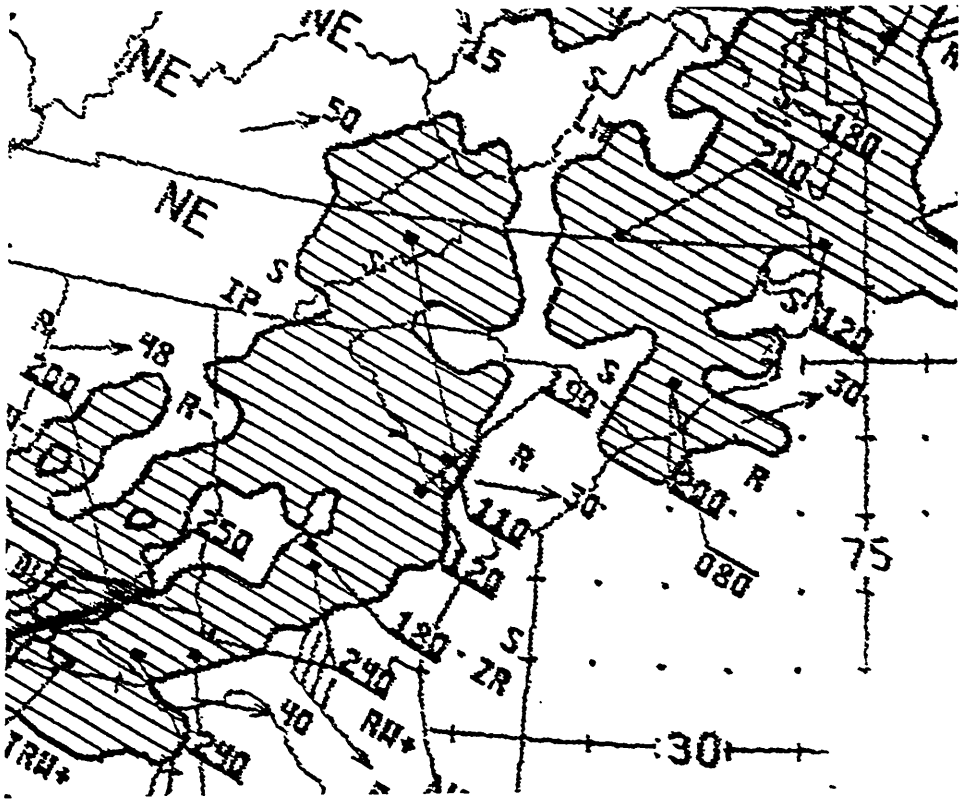

(3.3d) 14 FEB 2335Z Radar Summary.

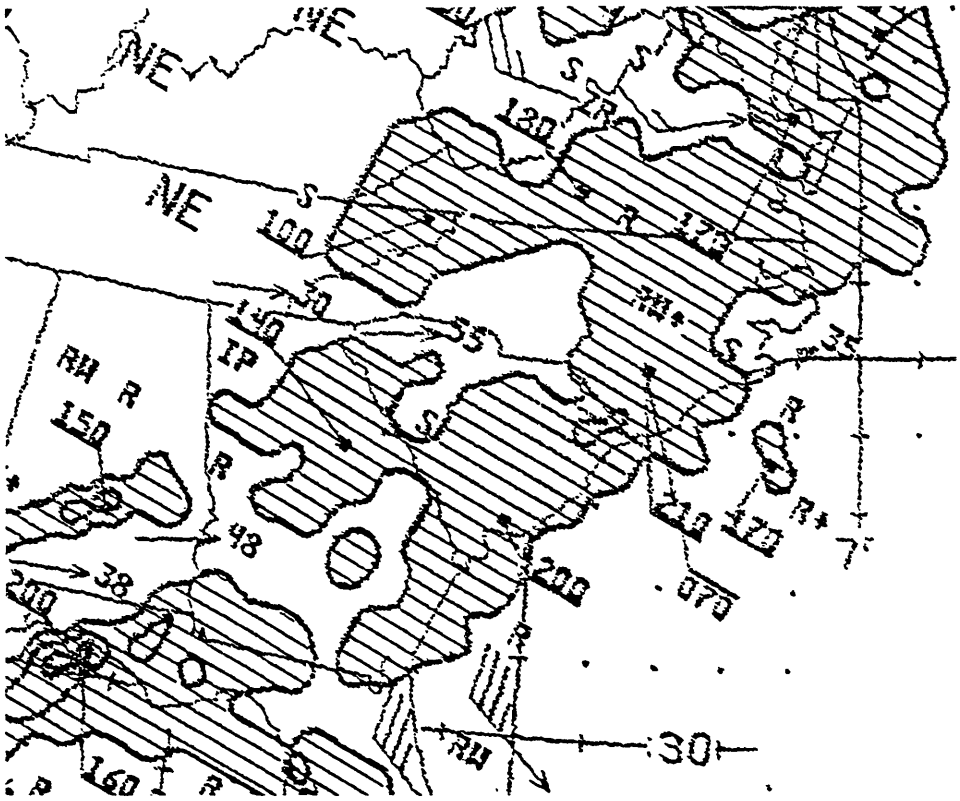

(3.3e) 15 FEB 0135Z Radar Summary.

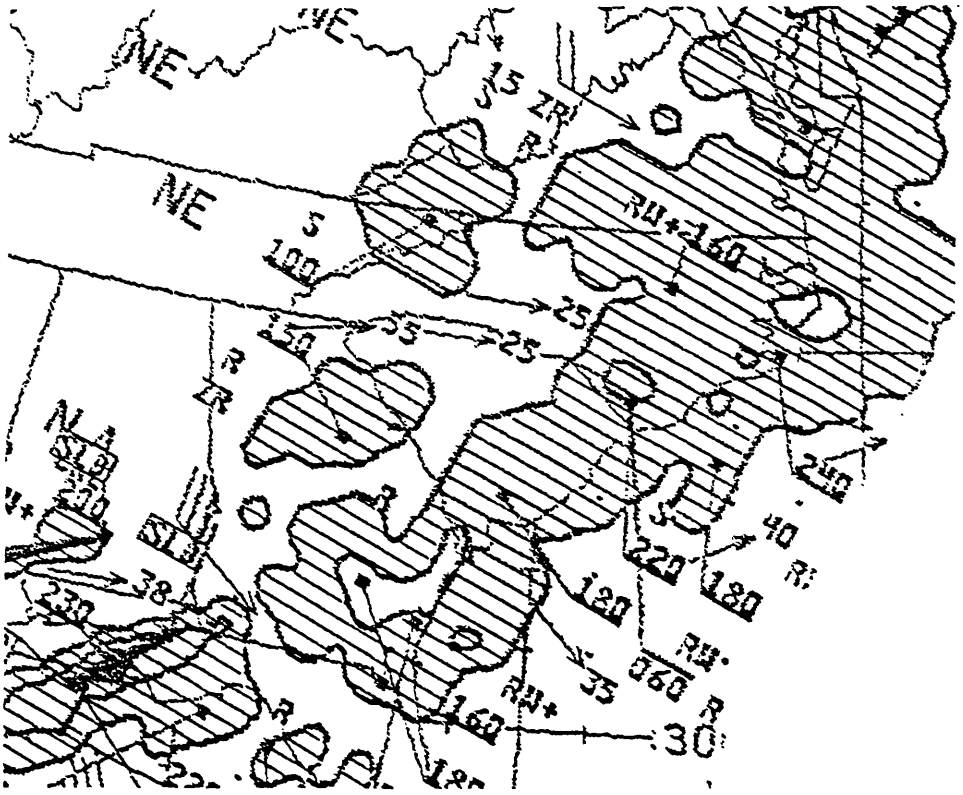

(3.3f) 15 FEB 0235Z Radar Summary.

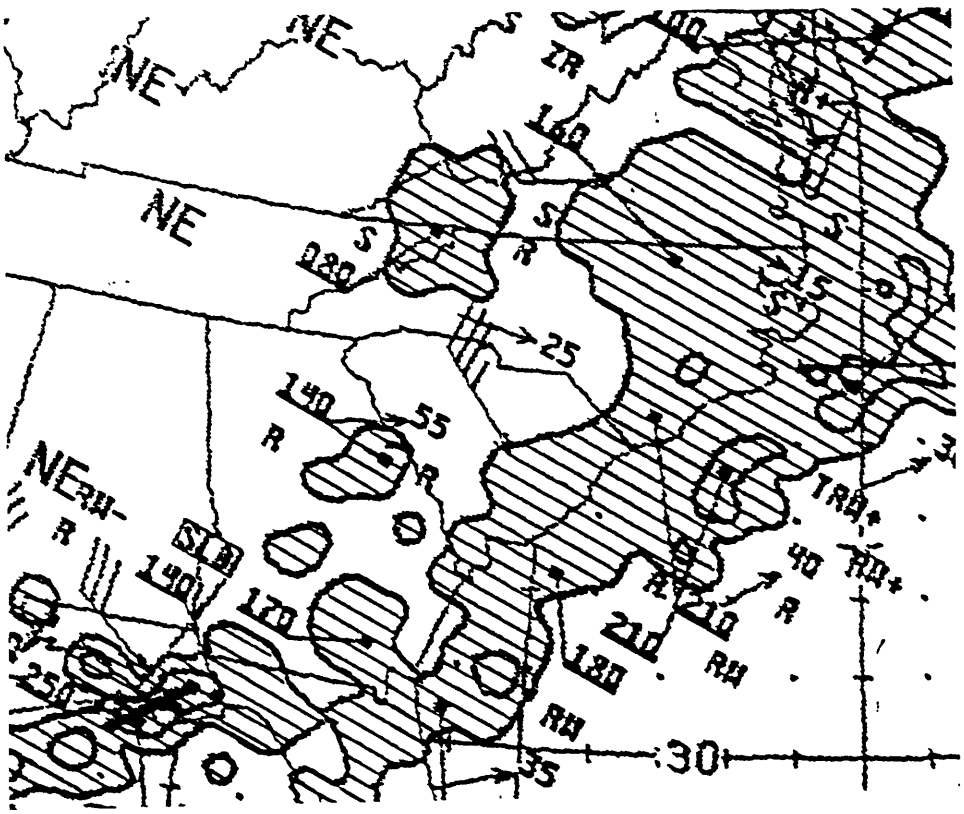

(3.3g) 15 FEB 0335Z Radar Summary.

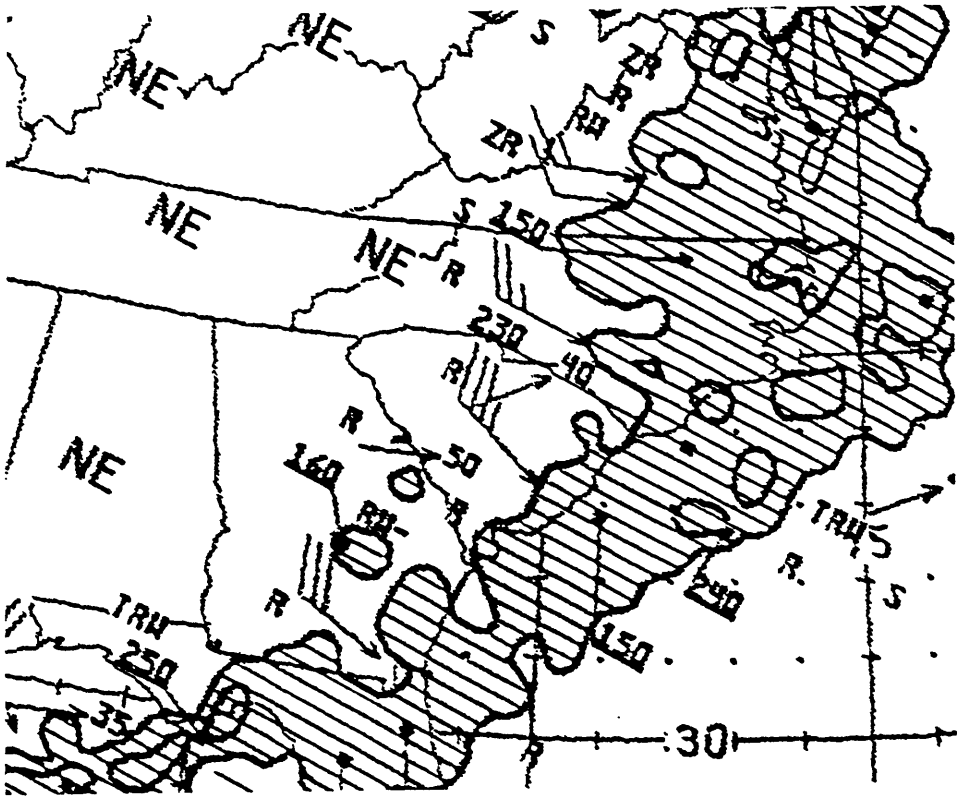

(3.3h) 15 FEB 0435Z Radar Summary.

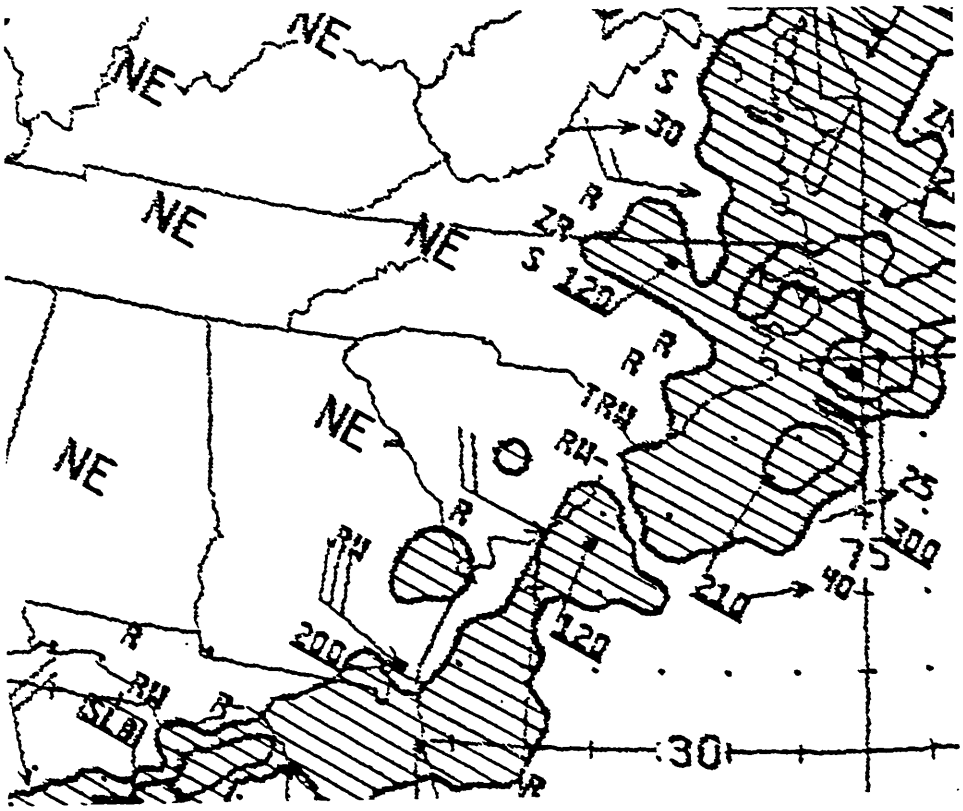

(3.3i) 15 FEB 0535Z Radar Summary.

Figure 3.3 National Weather Service radar summary.

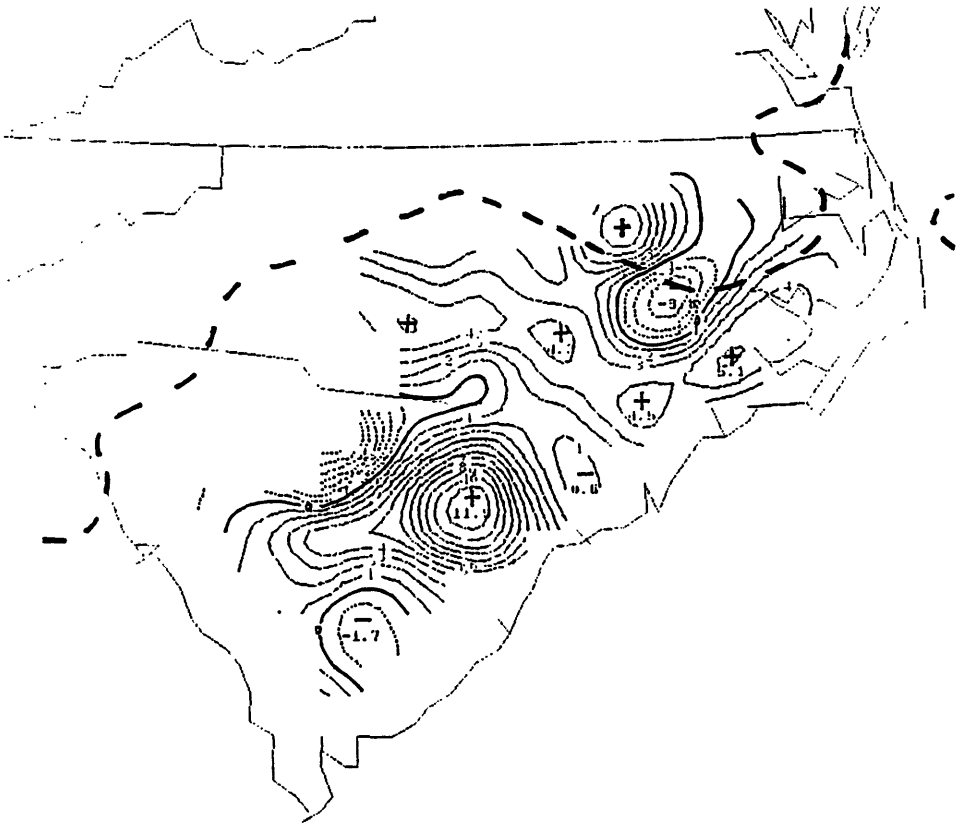

(3.4a) 14 FEB 2030Z, areas of evaporation (+) and the rate of evaporation. Heavy dash line is the border line of radar echo from Figure 3.3.

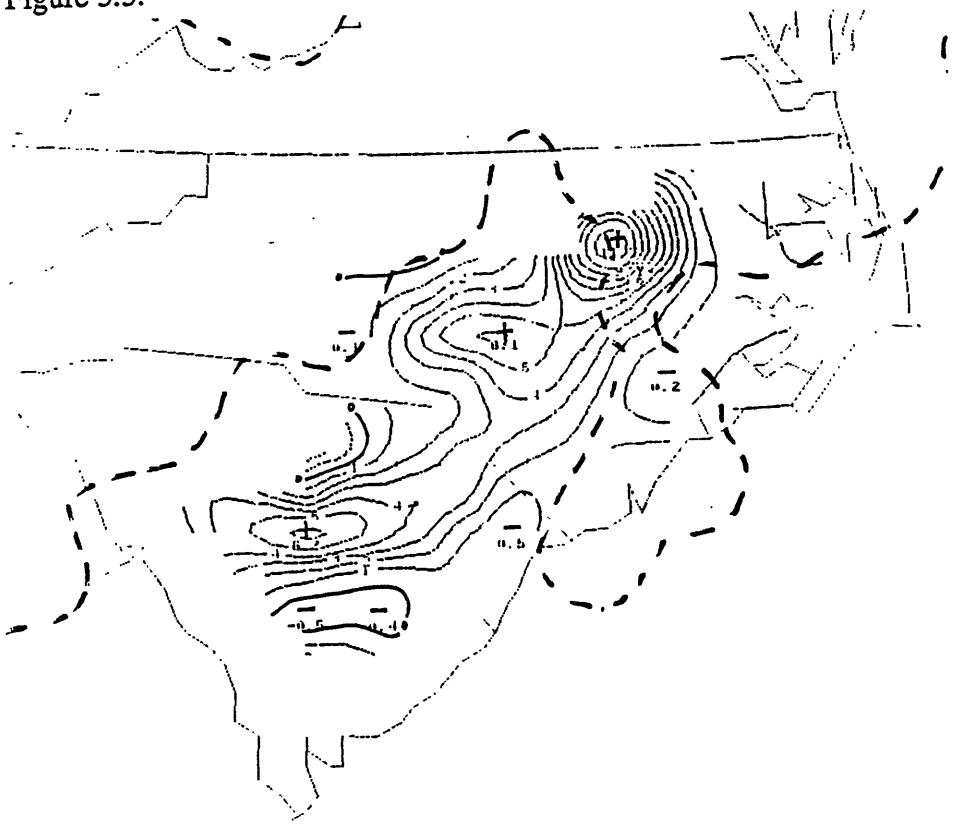

(3.4b) as that of 3.4a, except for 14 FEB 2130Z.

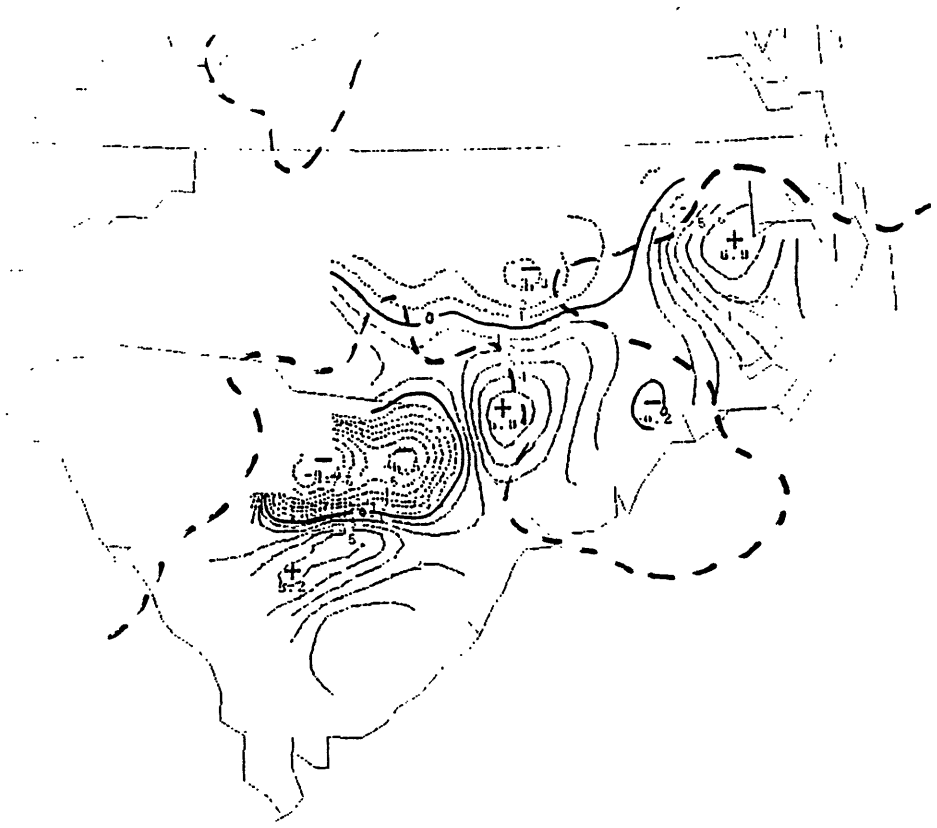

(3.4c) as that of 3.4a, except for 14 FEB 2230Z.

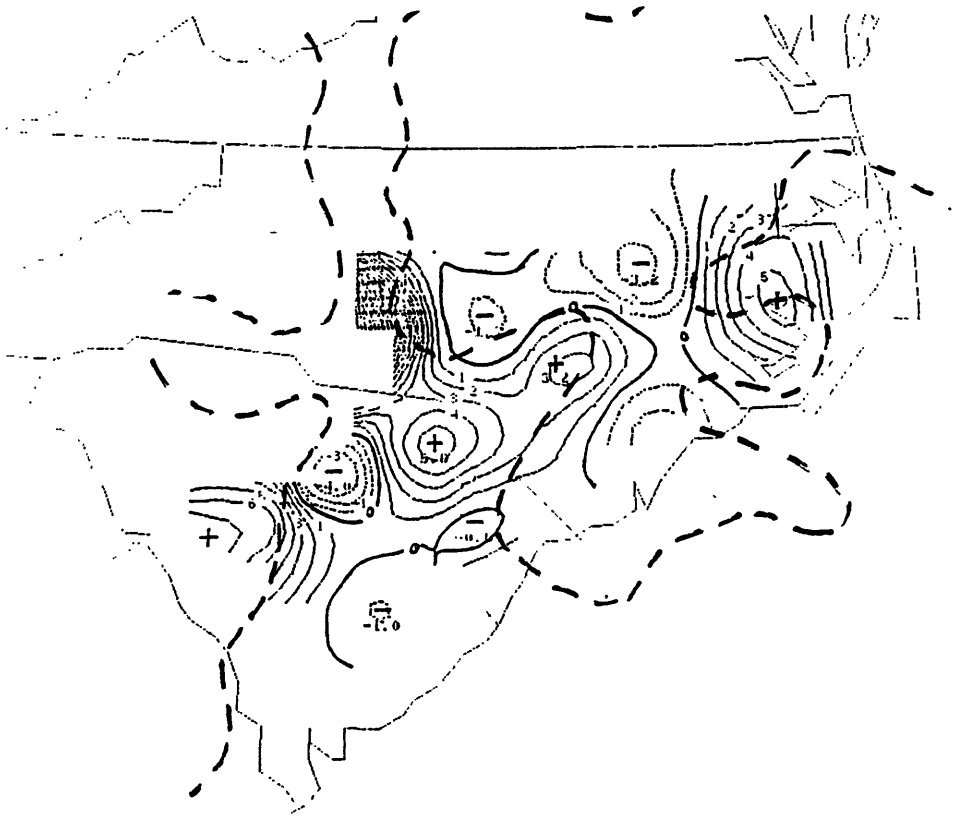

(3.4d) as that of 3.4a, except for 14 FEB 2330Z.

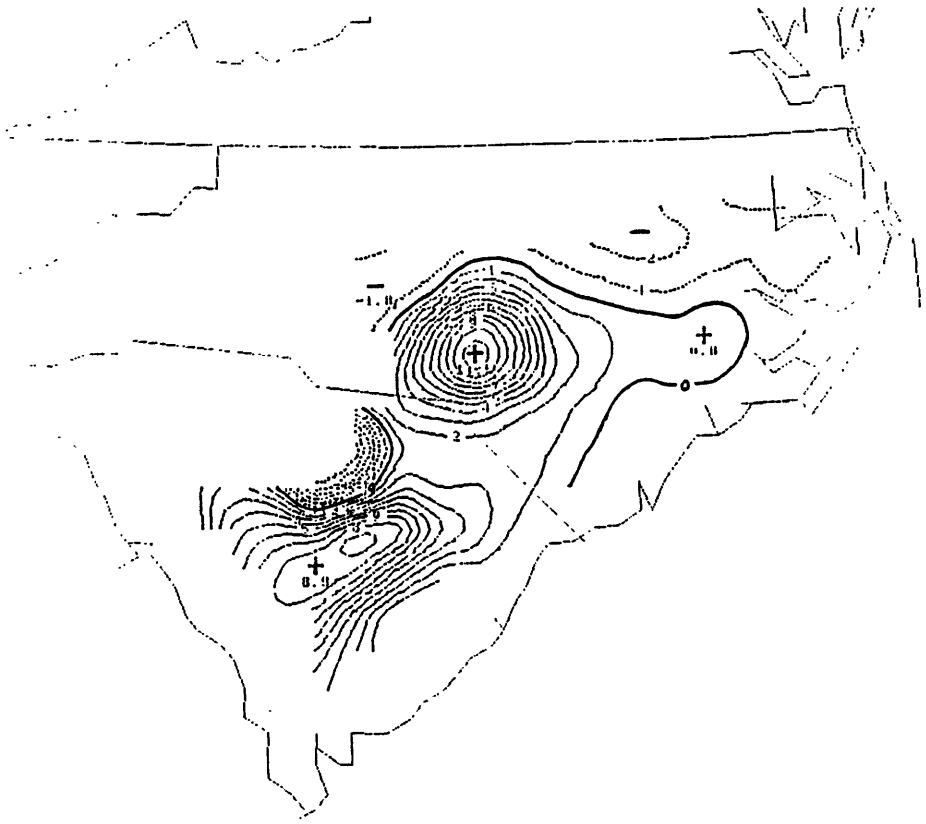

(3.4e) as that of 3.4a, except for 15 FEB 0030Z.

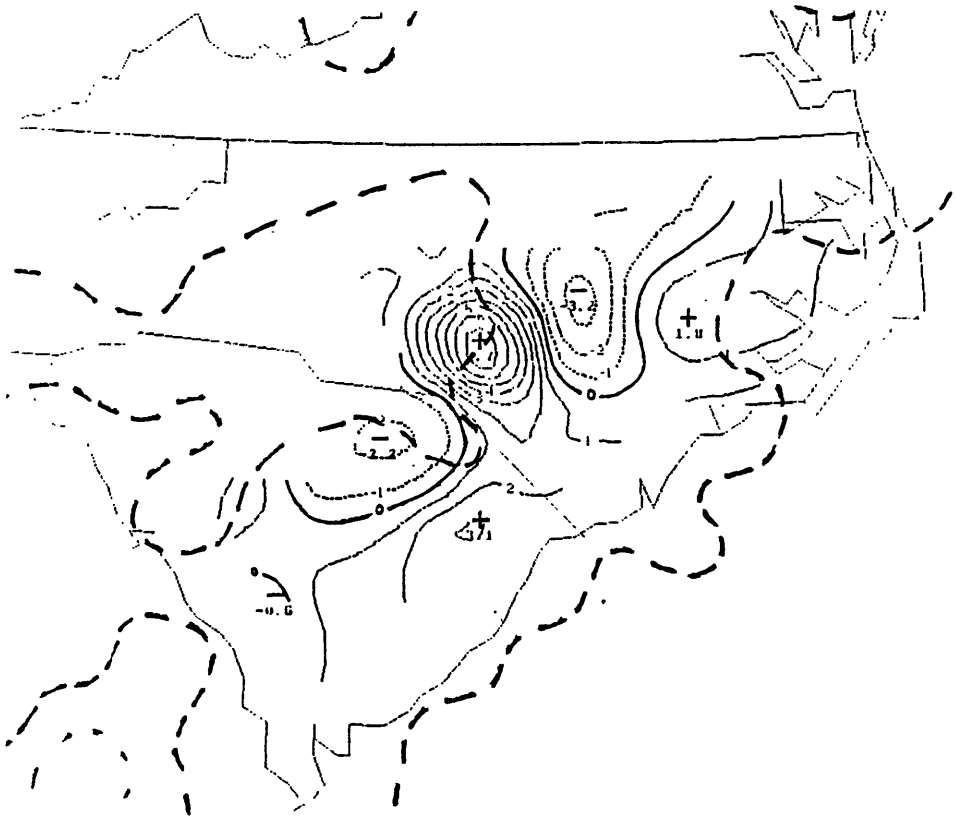

(3.4f) as that of 3.4a, except for 15 FEB 0130Z.

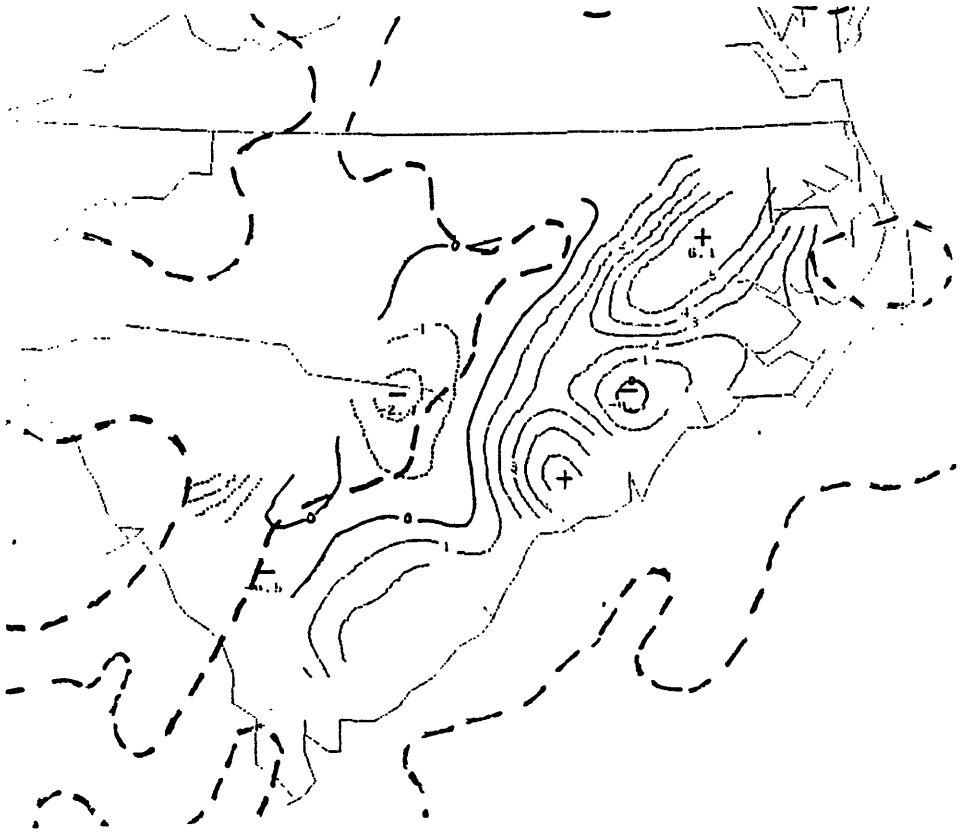

(3.4g) as that of 3.4a, except for 15 FEB 0230Z.

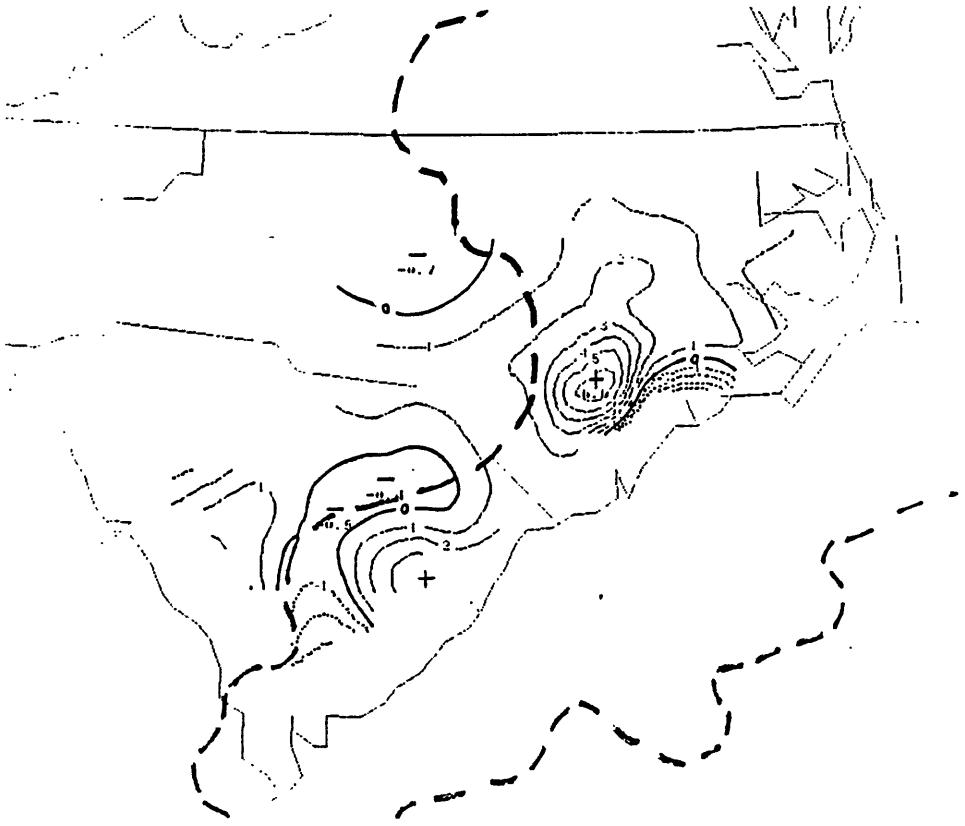

(3.4h) as that of 3.4a, except for 15 FEB 0330Z.

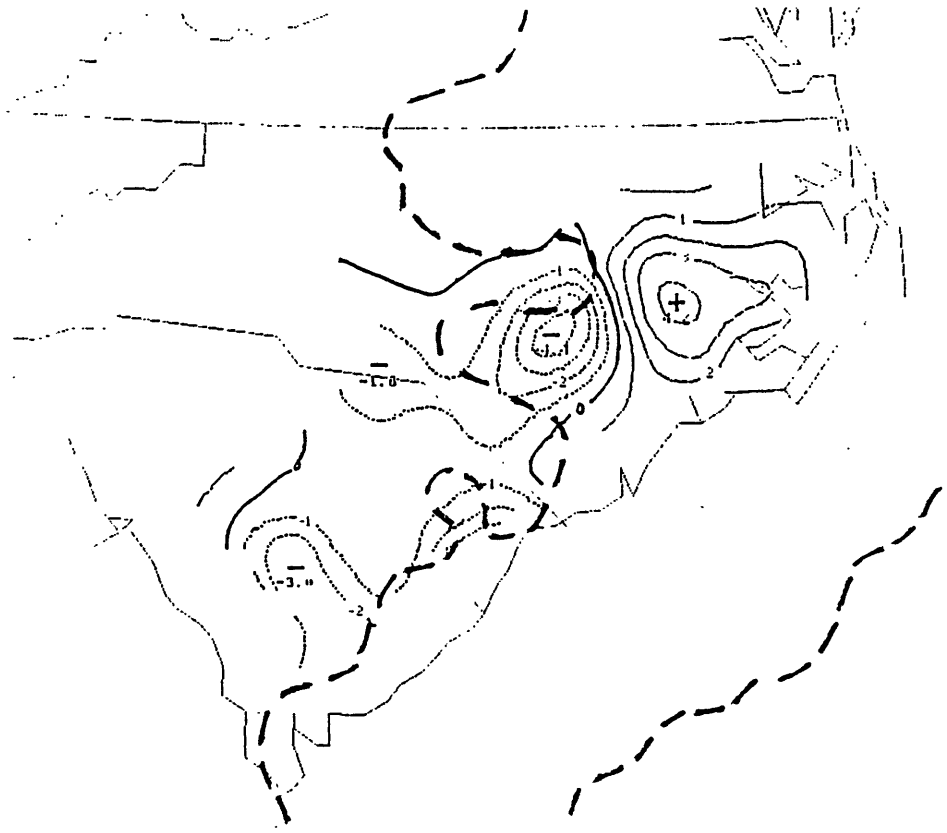

(3.4i) as that of 3.4a, except for 15 FEB 0430Z.

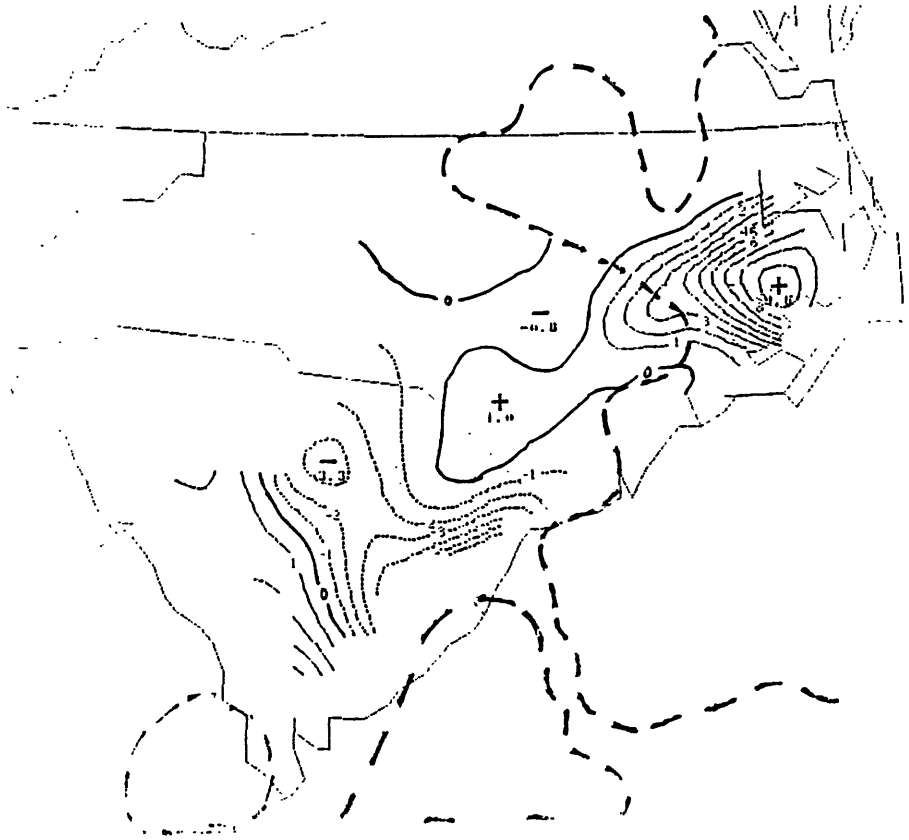

(3.4j) as that of 3.4a, except for 15 FEB 0530Z.

Figure 3.4 The rate of evaporation (areas with +) calculated from *pam-II* data set. Unit:

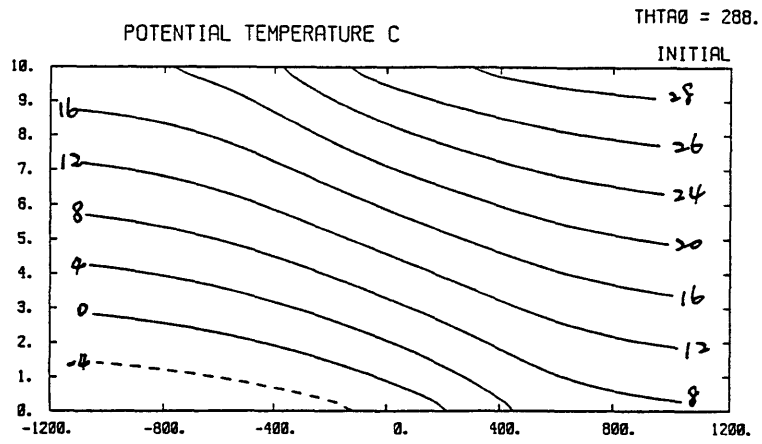

(5.1a) potential temperature θ (°C).

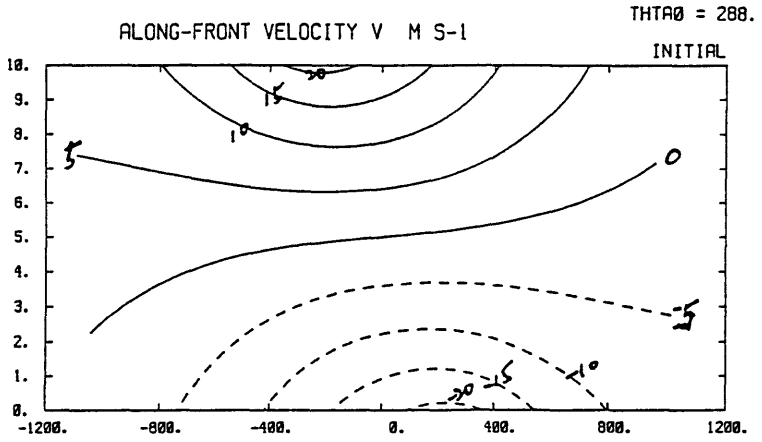

(5.1b) Along front velocity V_g (ms^{-1}). V_{gmax} = 21.22 ms^{-1}, V_{gmin} = -21.22 ms^{-1}.

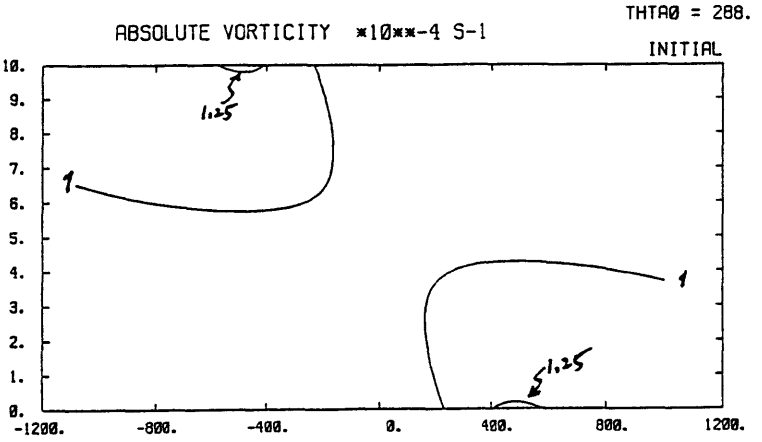

(5.1c) Absolute vorticity ζ ($10^{-4} s^{-1}$). ζ_{max} = 1.28 × $10^{-4} s^{-1}$, ζ_{min} = 0.79 × $10^{-4} s^{-1}$.

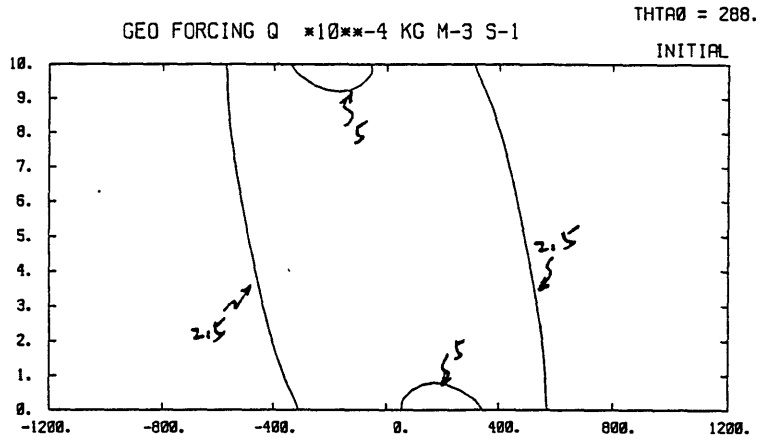

(5.1d) Geostrophic forcing Q (10^{-4}kg m^{-3}s^{-1}). $Q_{max} = 5.68 \times 10^{-4}$kg m^{-3} s^{-1}.

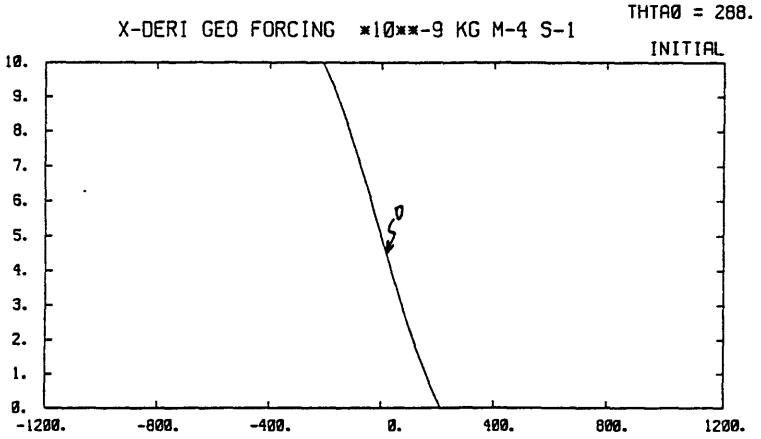

(5.1e) The x-derivative of geostrophic forcing $-Q_x$ (10^{-9}kg m^{-4}s^{-1}). $-Q_{x\,max} = 0.96 \times 10^{-9}$kg m^{-4}s^{-1}, $-Q_{x\,min} = -0.96 \times 10^{-9}$kg m^{-4}s^{-1}.

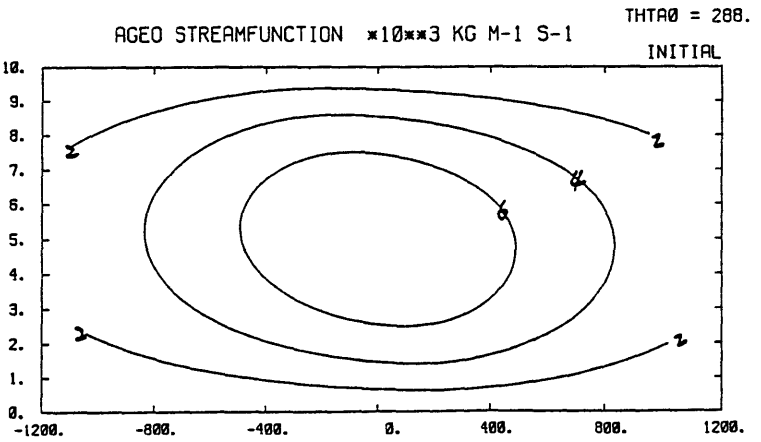

(5.1f) Streamfunction ψ (10^{3}kg m^{-1}s^{-1}). $\psi_{max} = 7.77 \times 10^{3}$kg m^{-1}s^{-1}.

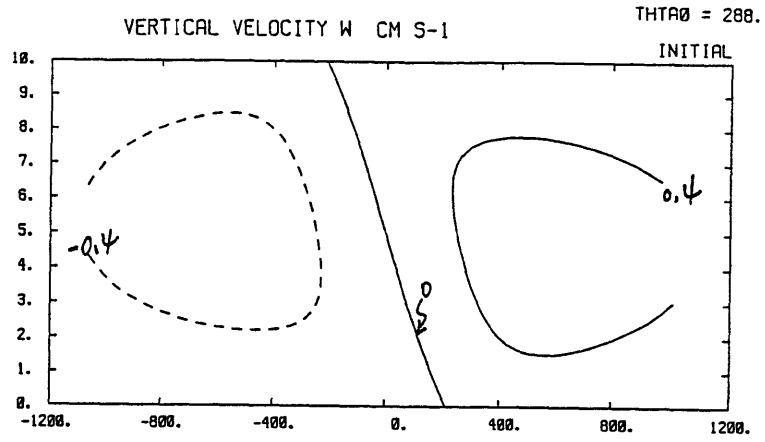

(5.1g) Vertical velocity w (cm s^{-1}). w_{max} = 0.60 cm s^{-1}, w_{min} = -0.60 cm s^{-1}.

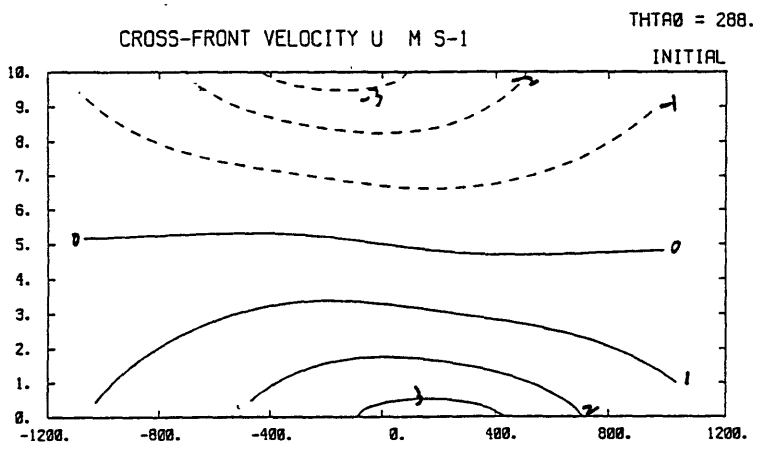

(5.1h) Ageostrophic velocity in the x-direction u_a (m s^{-1}). u_{amax} = 3.42 m s^{-1}, u_{amin} = -3.42 m s^{-1}.

Figure 5.1 Initial condition. Cross section in x-z plane in physical space; the unit is km in both z and x direction.

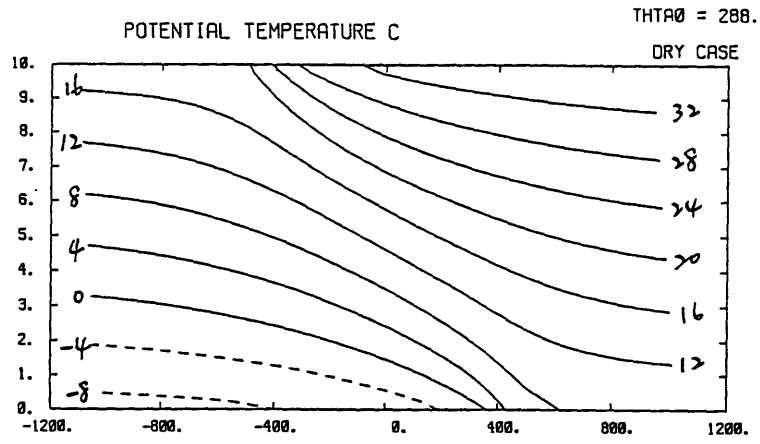

(5.2a) potential temperature θ (°C).

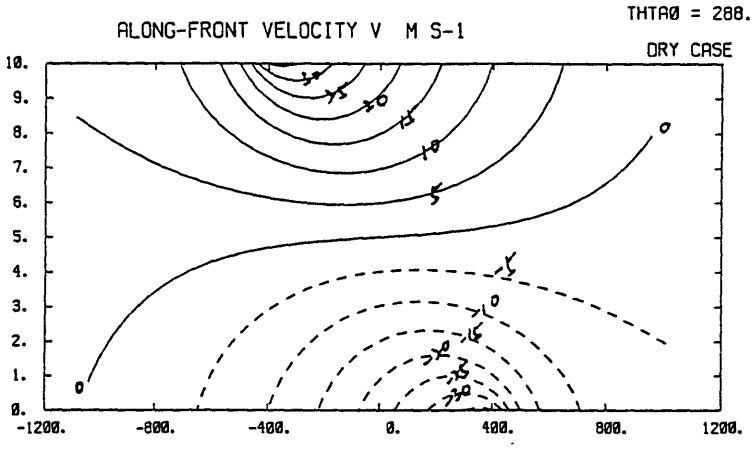

(5.2b) Along-front velocity V_g (ms^{-1}). V_{gmax} = 36.17 ms^{-1}, V_{gmin} = -36.17 ms^{-1}.

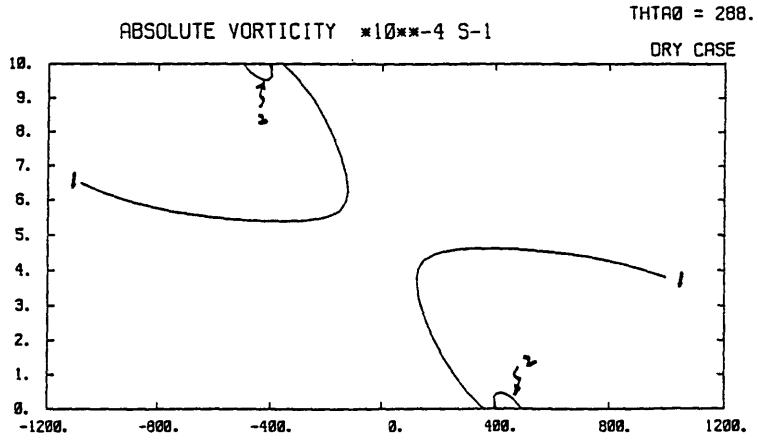

(5.2c) Absolute vorticity ζ ($10^{-4} s^{-1}$). ζ_{max} = 3.10 × $10^{-4} s^{-1}$, ζ_{min} = 0.58 × $10^{-4} s^{-1}$.

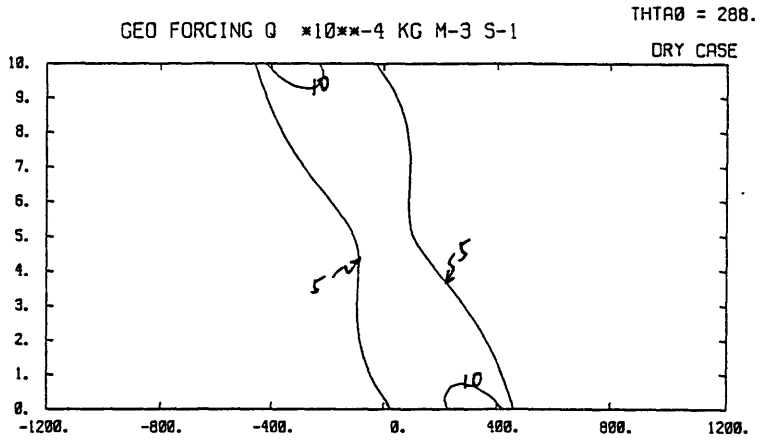

(5.2d) Geostrophic forcing Q (10^{-4} kg m^{-3} s^{-1}). Q_{max} = 13.25 × 10^{-4} kg m^{-3} s^{-1}.

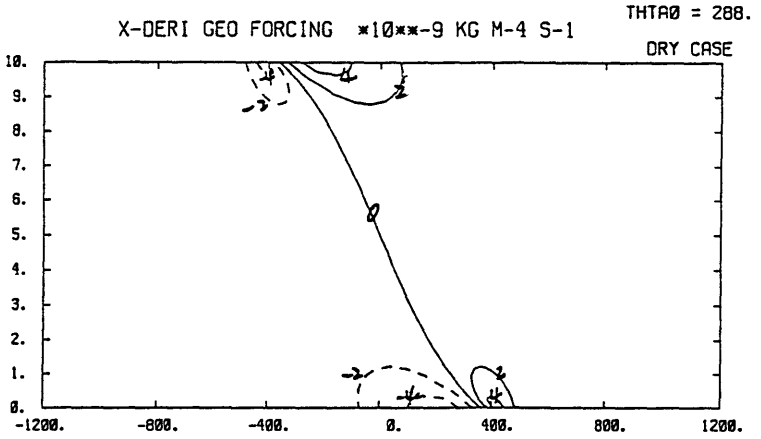

(5.2e) The x-derivative of geostrophic forcing -Q_x (10^{-9} kg m^{-4} s^{-1}). -$Q_{x\,max}$ = 4.93 × 10^{-9} kg m^{-4} s^{-1}, -$Q_{x\,min}$ = -4.93 × 10^{-9} kg m^{-4} s^{-1}.

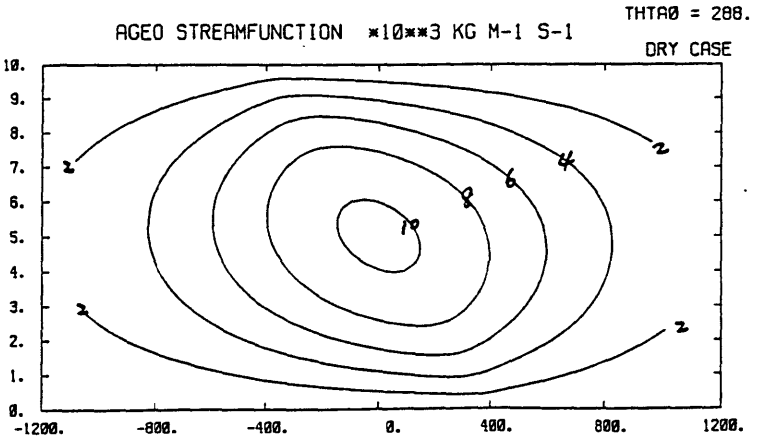

(5.2f) Streamfunction ψ (10^{3} kg m^{-1} s^{-1}). ψ_{max} = 10.36 × 10^{3} kg m^{-1} s^{-1}.

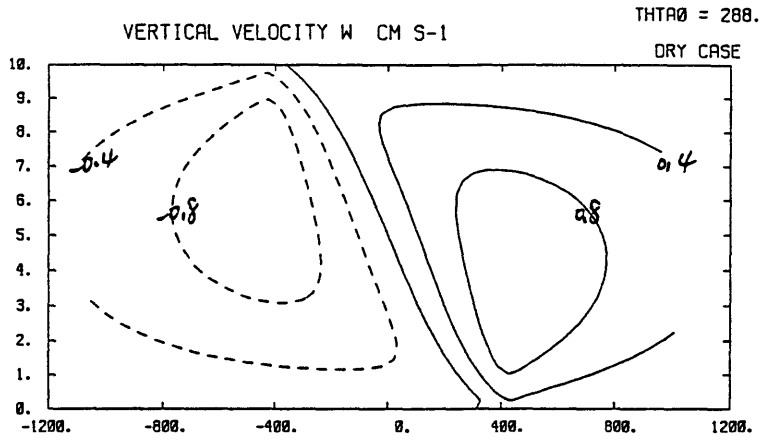

(5.2g) Vertical velocity w (cm s^{-1}). w_{max} = 1.04 cm s^{-1}, w_{min} = -1.04 cm s^{-1}.

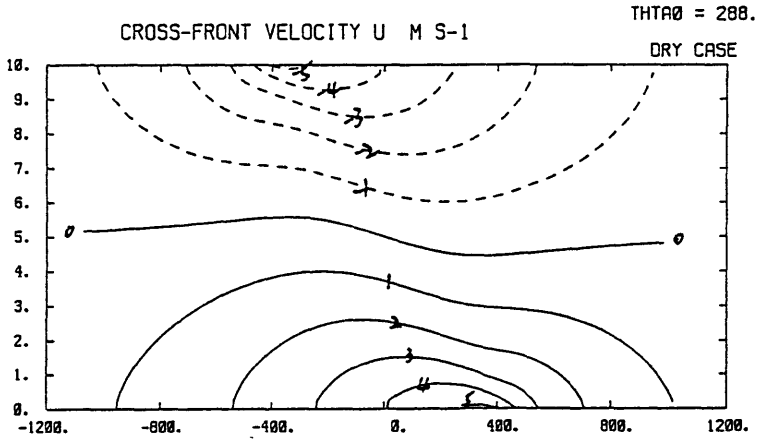

(5.2h) Ageostrophic velocity in the x-direction u_a (m s^{-1}). u_{amax} = 5.14 m s^{-1}, u_{amin} = -5.14 m s^{-1}.

Figure 5.2 Case-D, after one day of simulation. Cross section in x-z plane in physical space; the unit is km in both z and x direction.

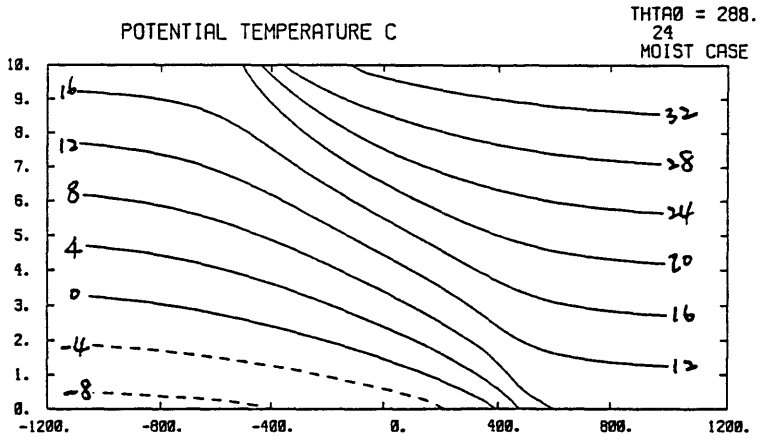

(5.3a) Potential temperature θ (°C).

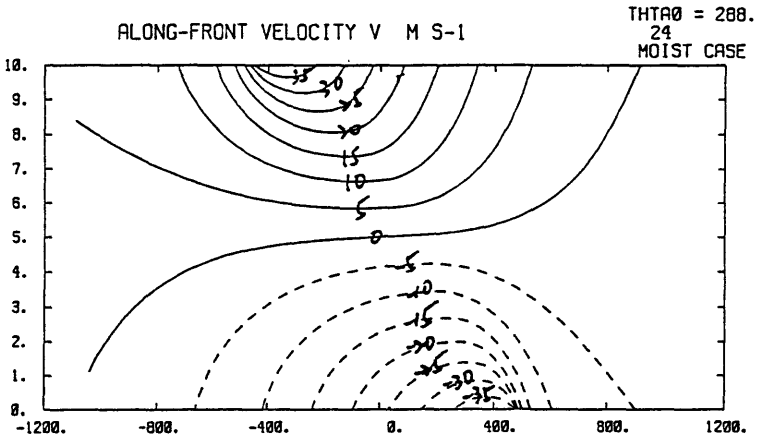

(5.3b) Along-front velocity V_g (ms^{-1}). V_{gmax} = 39.52 ms^{-1}, V_{gmin} = -39.51 ms^{-1}.

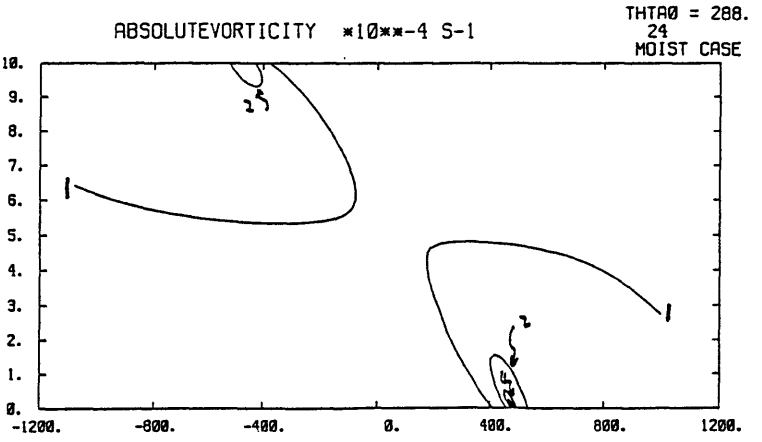

(5.3c) Absolute vorticity ζ ($10^{-4} s^{-1}$). ζ_{max} = 12.52 × $10^{-4} s^{-1}$, ζ_{min} = 0.56 × $10^{-4} s^{-1}$.

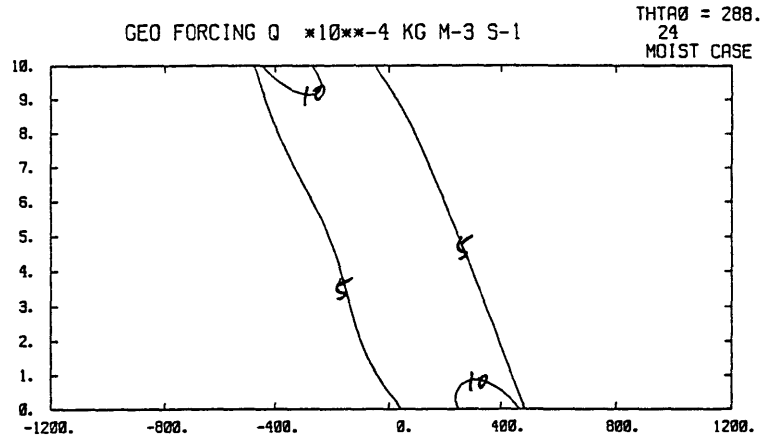

(5.3d) Geostrophic forcing Q (10^{-4}kg m^{-3}s^{-1}). Q_{max} = 13.18 × 10^{-4}kg m^{-3} s^{-1}.

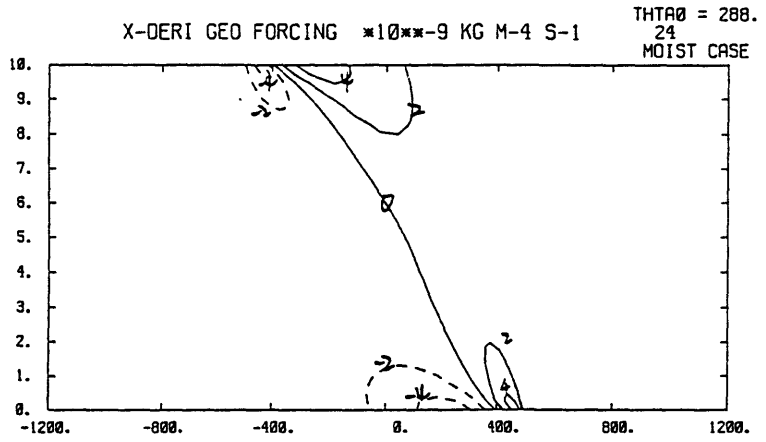

(5.3e) The x-derivative of geostrophic forcing -Q_x (10^{-9}kg m^{-4}s^{-1}). -$Q_{x\,max}$=4.97 × 10^{-9}kg m^{-4}s^{-1}, -$Q_{x\,mn}$= -4.97 × 10^{-9}kg m^{-4}s^{-1}.

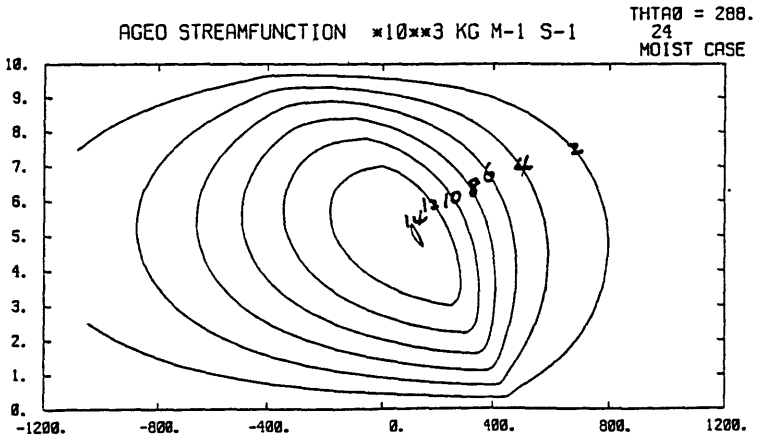

(5.3f) Streamfunction ψ (10^{3}kg m^{-1}s^{-1}). ψ_{max} = 14.06 × 10^{3}kg m^{-1}s^{-1}.

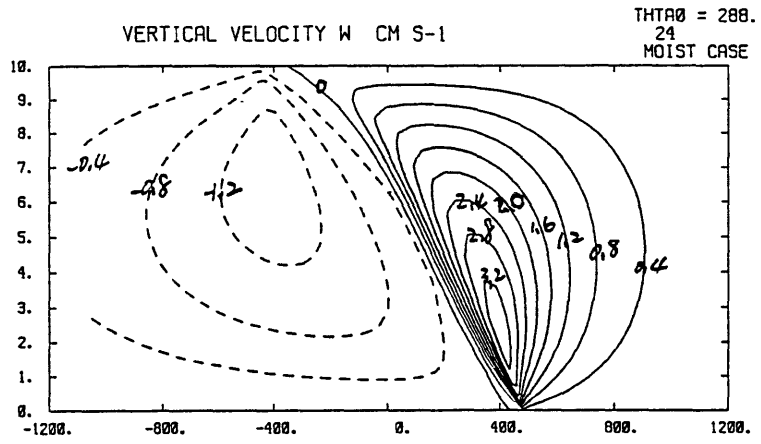

(5.3g) Vertical velocity w (cm s^{-1}). w_{max} = 3.39 cm s^{-1}, w_{min} = -1.38 cm s^{-1}.

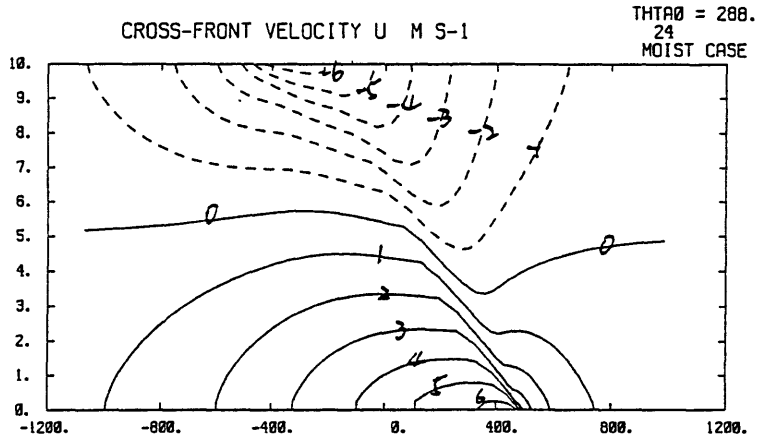

(5.3h) Ageostrophic velocity in the x-direction u_a (m s^{-1}). u_{amax} = 6.28 m s^{-1}, u_{amin} = -6.27 m s^{-1}.

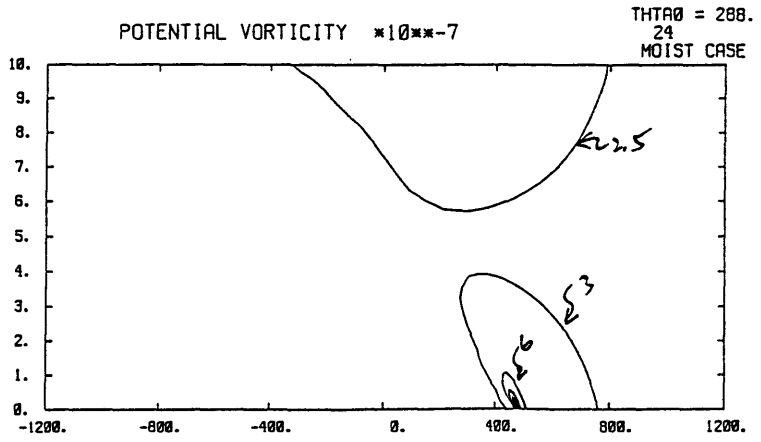

(5.3i) Potential vorticity q (10^{-7} m^2 °K s^{-1} kg^{-1}). q_{max} = 19.30 × 10^{-7} m^2 °K s^{-1} kg^{-1}, q_{min} = 1.77 × 10^{-7} m^2 °K s^{-1} kg^{-1}.

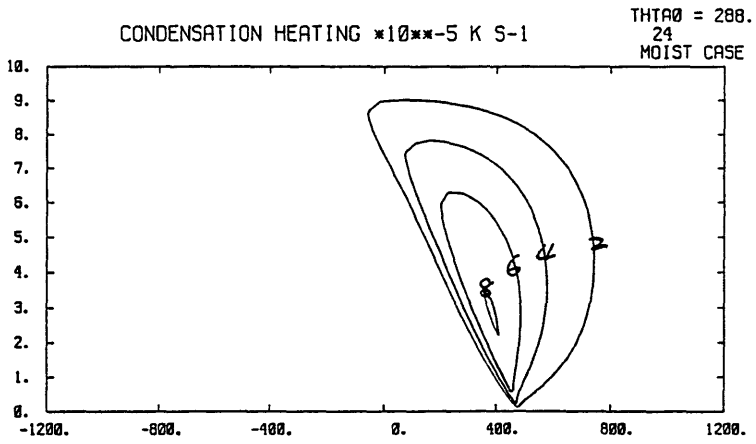

(5.3j) Condensational heating S at one day of moist simulation.

$S_{max} = 8.12 \times 10^{-5}$ °K s^{-1}.

Figure 5.3 Case-C, after one day of simulation. Cross section in x-z plane in physical space; the unit is km in both z and x direction.

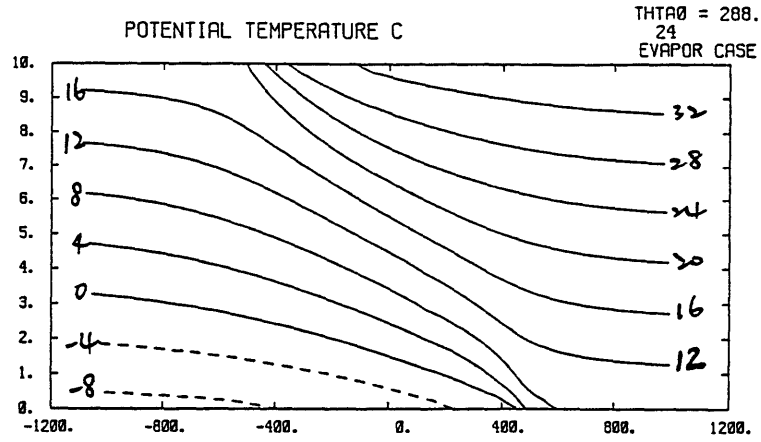

(5.4a) Potential temperature θ (°C).

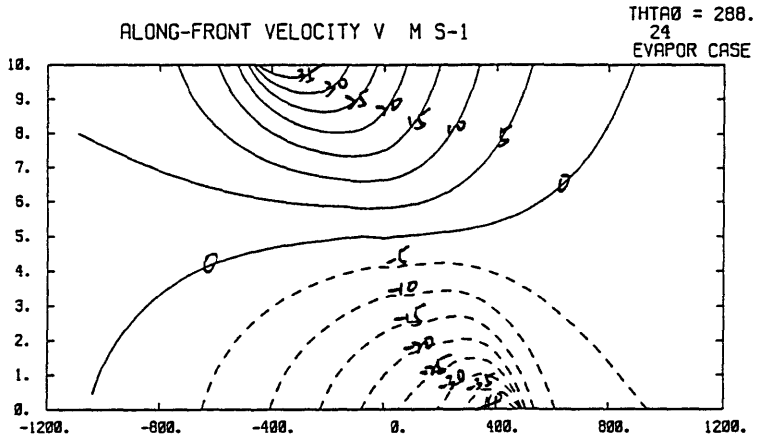

(5.4b) Along-front velocity V_g (ms^{-1}). V_{gmax} = 39.64 ms^{-1}, V_{gmin} = -44.54 ms^{-1}.

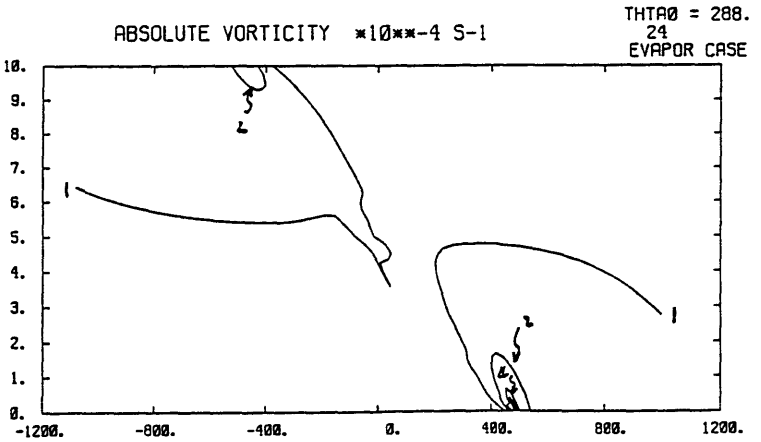

(5.4c) Absolute vorticity ζ (10^{-4} s^{-1}). ζ_{max} = 29.72 × 10^{-4} s^{-1}, ζ_{min} = 0.40 × 10^{-4} s^{-1}.

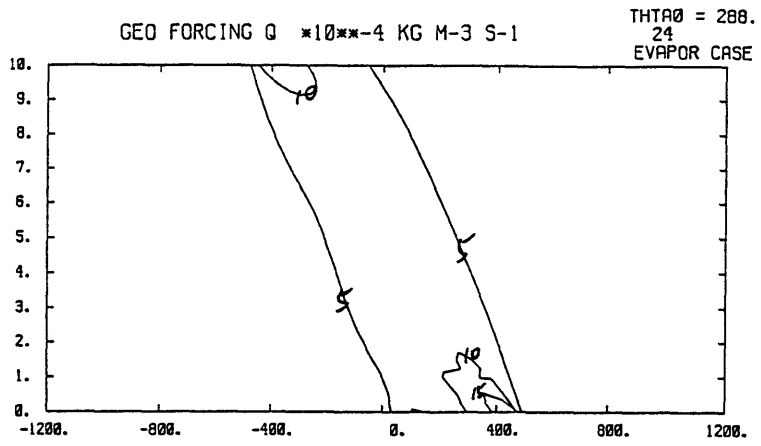

(5.4d) Geostrophic forcing Q (10^{-4} kg m^{-3} s^{-1}). $Q_{max} = 19.34 \times 10^{-4}$ kg m^{-3} s^{-1}.

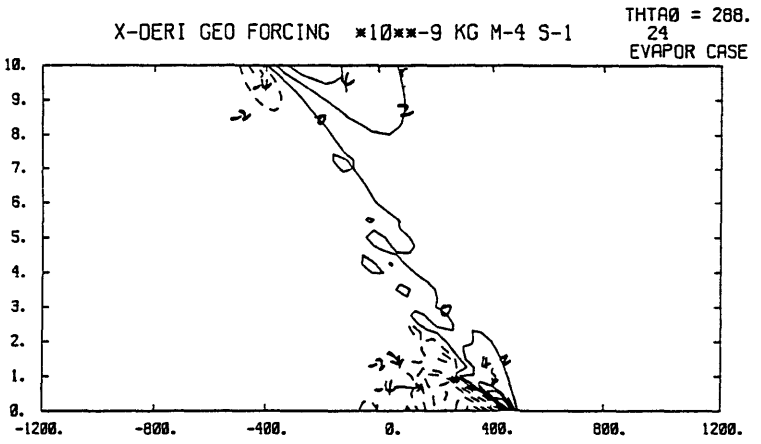

(5.4e) The x-derivative of geostrophic forcing $-Q_x$ (10^{-9} kg m^{-4} s^{-1}). $-Q_{x\,max} = 12.33 \times 10^{-9}$ kg m^{-4} s^{-1}, $-Q_{x\,min} = -13.89 \times 10^{-9}$ kg m^{-4} s^{-1}.

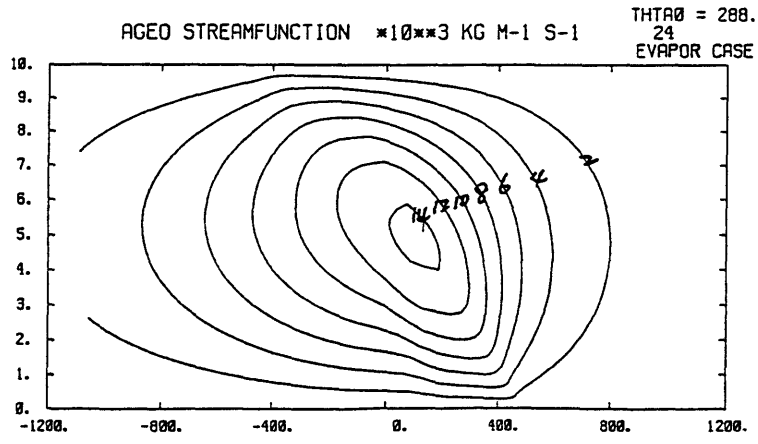

(5.4f) Streamfunction ψ (10^{3} kg m^{-1} s^{-1}). $\psi_{max} = 14.44 \times 10^{3}$ kg m^{-1} s^{-1}.

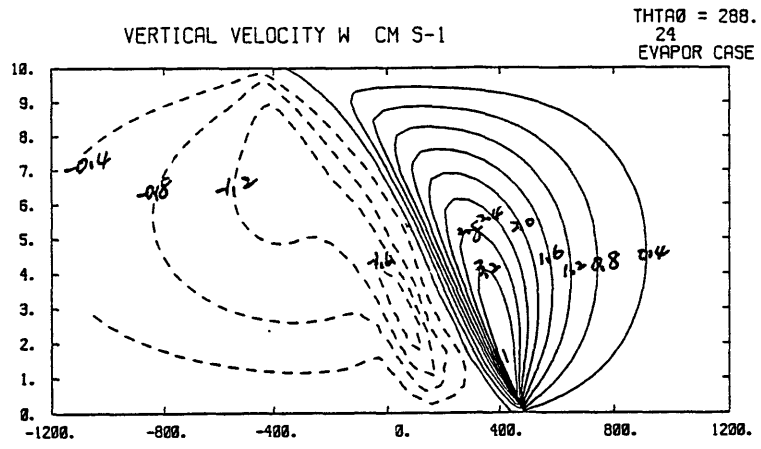

(5.4g) Vertical velocity w (cm s^{-1}). w_{max} = 3.58 cm s^{-1}, w_{min} = -1.91 cm s^{-1}.

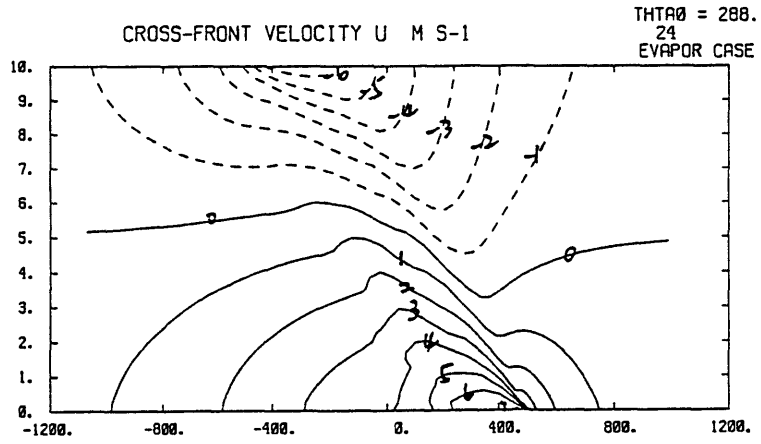

(5.4h) Ageostrophic velocity in the x-direction u_a (m s^{-1}). u_{amax} = 7.15 m s^{-1}, u_{amin} = -6.34 m s^{-1}.

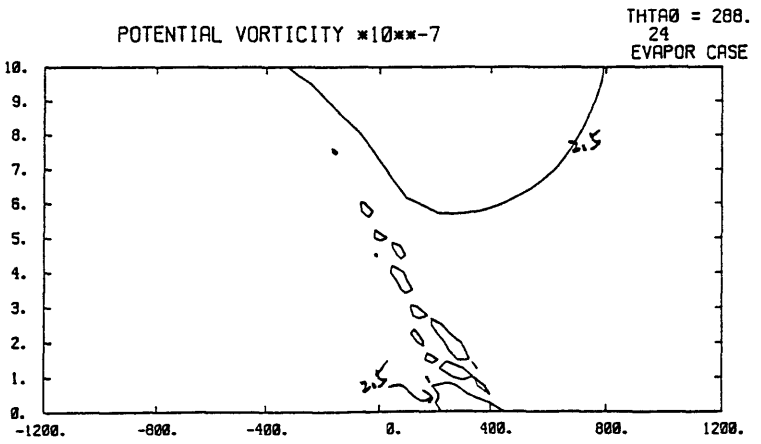

(5.4i) Potential vorticity q less than 2.5 × 10^{-7} m^2 °K s^{-1} kg^{-1}. q_{min} = 1.77 × 10^{-7} m^2 °K s^{-1} kg^{-1}, on the upper boundary.

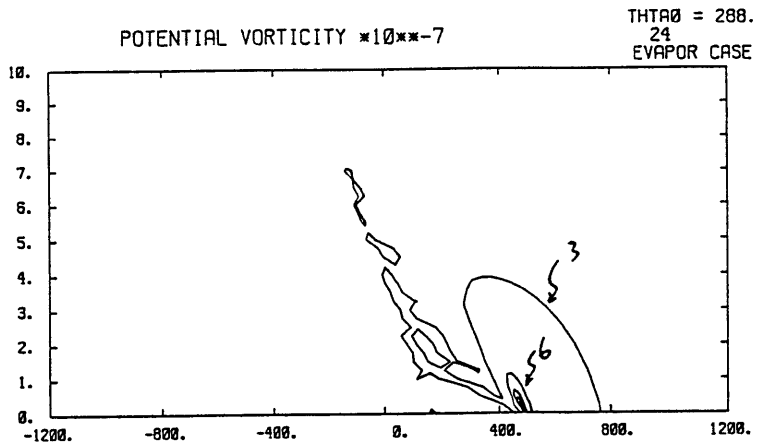

(5.4j) Potential vorticity q larger than $3 \times 10^{-7} m^2 °K\ s^{-1} kg^{-1}$. $q_{max} = 27.53 \times 10^{-7} m^2 °K\ s^{-1} kg^{-1}$.

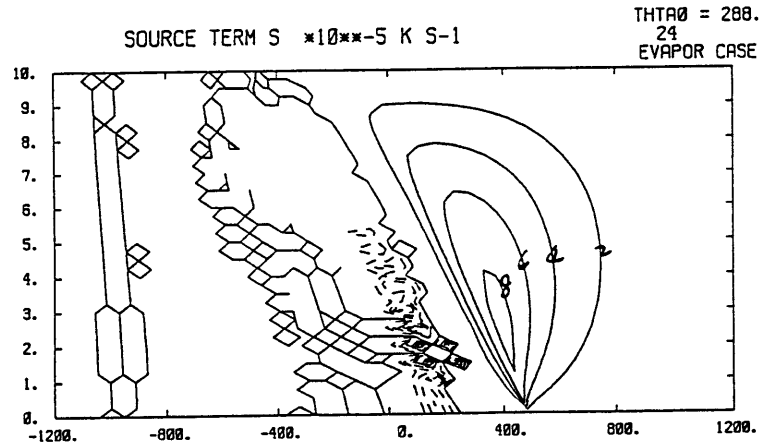

(5.4k) Source term (heating or cooling rate). $S_{max} = 8.44 \times 10^{-5} °K\ s^{-1}$.

Figure 5.4 Case-E, after one day of simulation. Cross section in x-z plane in physical space; the unit is km in both z and x direction.

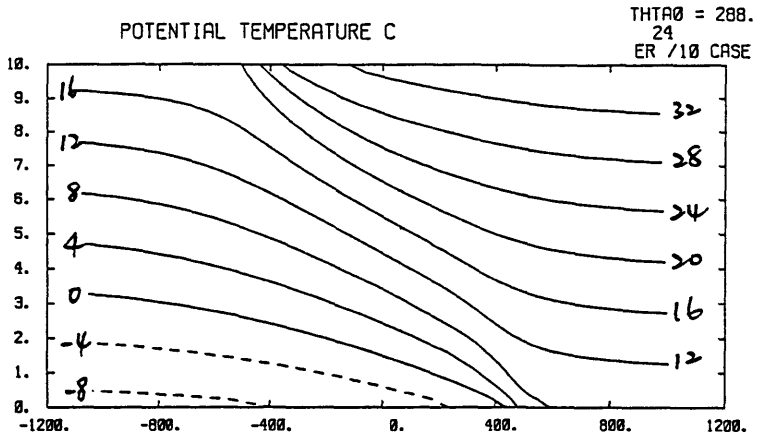

(5.5a) Potential temperature θ (°C).

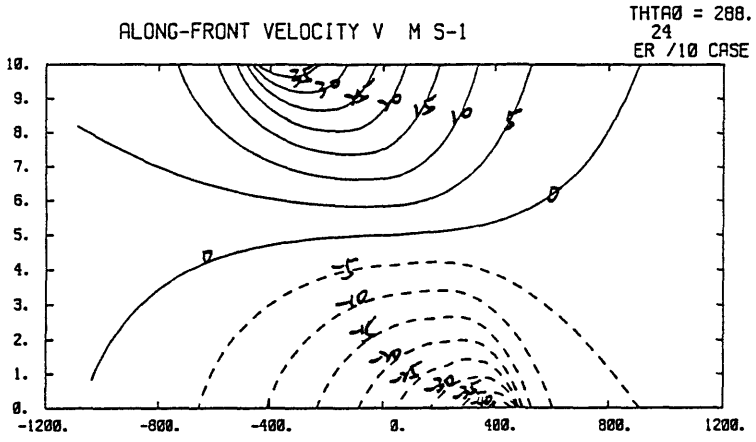

(5.5b) Along-front velocity V_g (ms^{-1}). V_{gmax} = 39.55 ms^{-1}, V_{gmin} = -42.66 ms^{-1}.

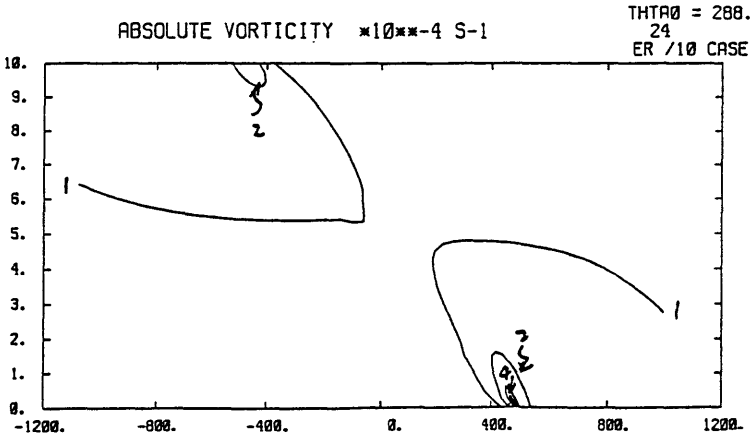

(5.5c) Absolute vorticity ζ ($10^{-4} s^{-1}$). ζ_{max} = 16.42 × $10^{-4} s^{-1}$, ζ_{min} = 0.49 × $10^{-4} s^{-1}$.

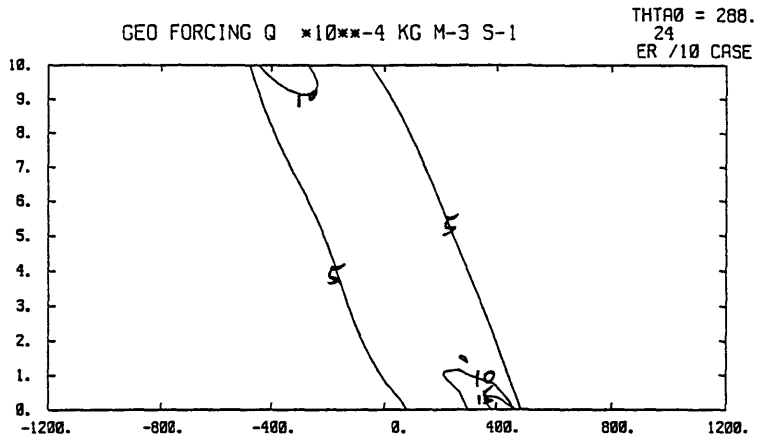

(5.5d) Geostrophic forcing Q (10^{-4} kg m^{-3} s^{-1}). Q_{max} = 18.35 × 10^{-4} kg m^{-3} s^{-1}.

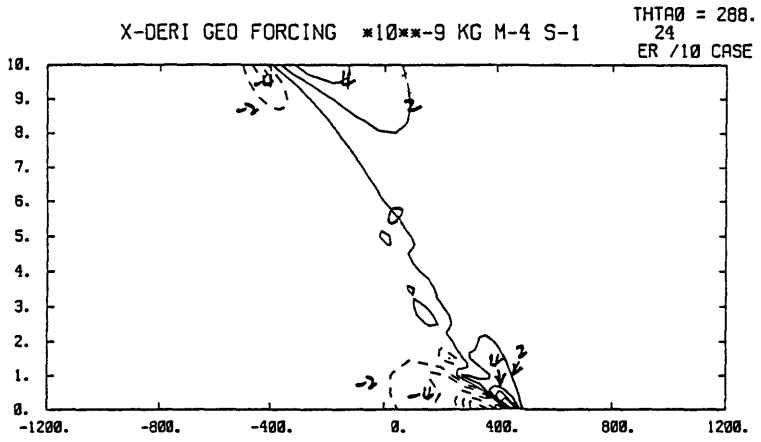

(5.5e) The x-derivative of geostrophic forcing -Q_x (10^{-9} kg m^{-4} s^{-1}). -$Q_{x\,max}$ = 10.66 × 10^{-9} kg m^{-4} s^{-1}, -$Q_{x\,min}$ = -12.21 × 10^{-9} kg m^{-4} s^{-1}.

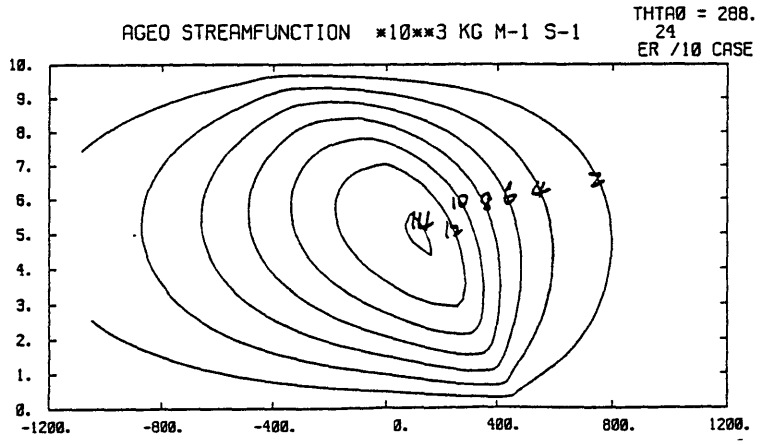

(5.5f) Streamfunction ψ (10^{3} kg m^{-1} s^{-1}). ψ_{max} = 14.18 × 10^{3} kg m^{-1} s^{-1}.

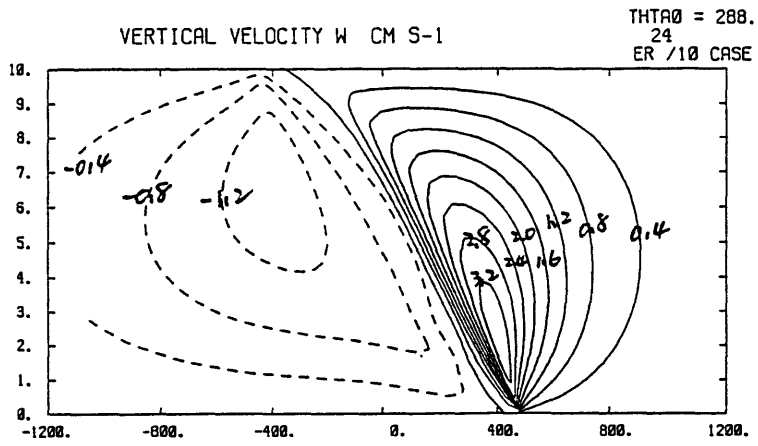

(5.5g) Vertical velocity w (cm s^{-1}). w_{max} = 3.46 cm s^{-1}, w_{min} = -1.39 cm s^{-1}.

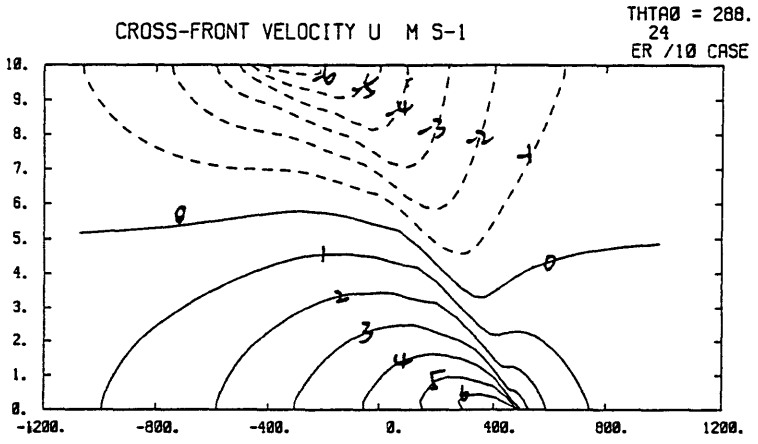

(5.5h) Ageostrophic velocity in the x-direction u_a (m s^{-1}). u_{amax} = 6.85 m s^{-1}, u_{amin} = -6.28 m s^{-1}.

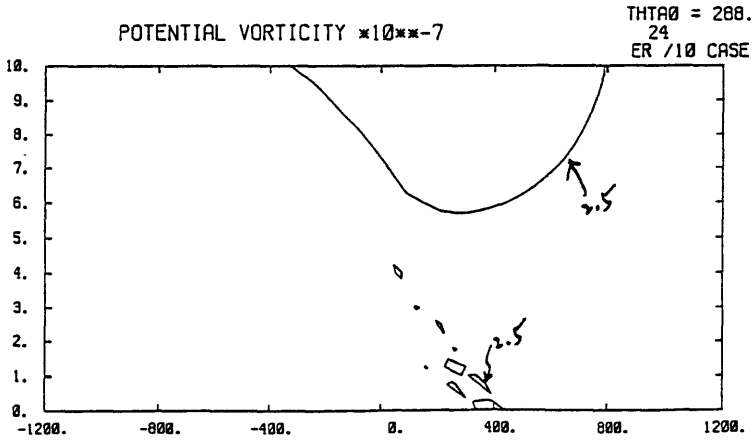

(5.5i) Potential vorticity q less than 2.5 × 10^{-7} m^2 °K s^{-1} kg^{-1}. q_{min} = 1.77 × 10^{-7} m^2 °K s^{-1} kg^{-1}, on the upper boundary.

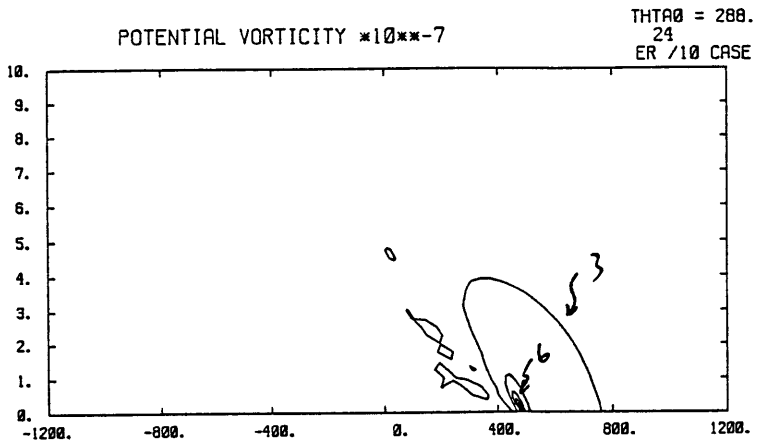

(5.5j) Potential vorticity q larger than 3×10^{-7} m² °K s⁻¹ kg⁻¹. $q_{max} = 21.91 \times 10^{-7}$ m² °K s⁻¹ kg⁻¹.

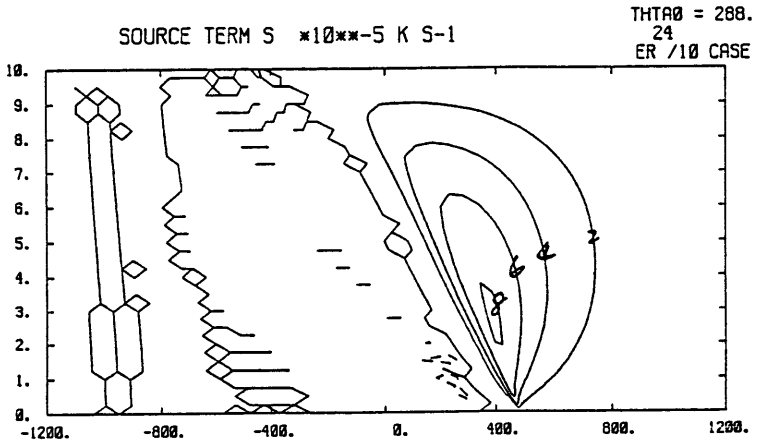

(5.5k) Source term (heating or cooling rate). $S_{max} = 8.25 \times 10^{-5}$ °K s⁻¹.

Figure 5.5 Case Er/10, after one day of simulation. Cross section in x-z plane in physical space; the unit is km in both z and x direction.

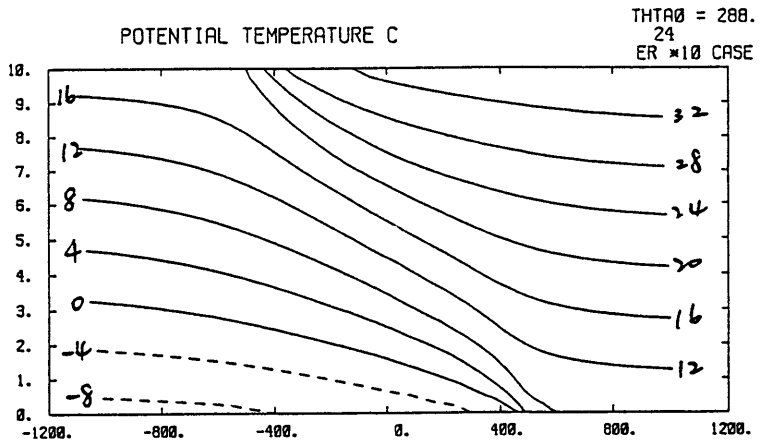

(5.6a) Potential temperature θ (°C).

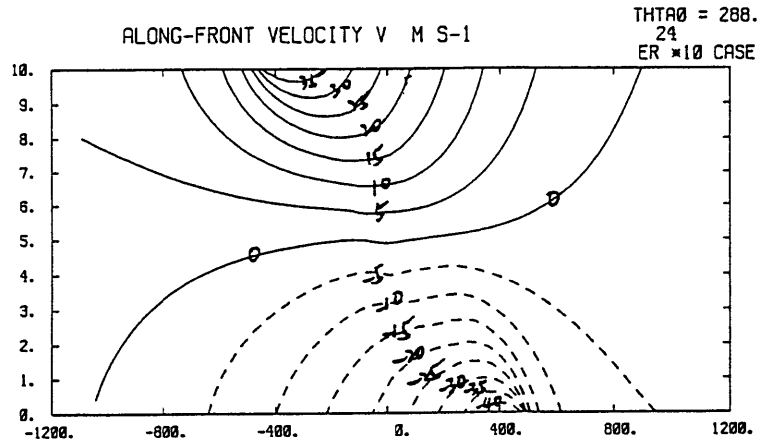

(5.6b) Along-front velocity V_g (ms^{-1}). V_{gmax} = 39.55 ms^{-1}, V_{gmin} = -45.37 ms^{-1}.

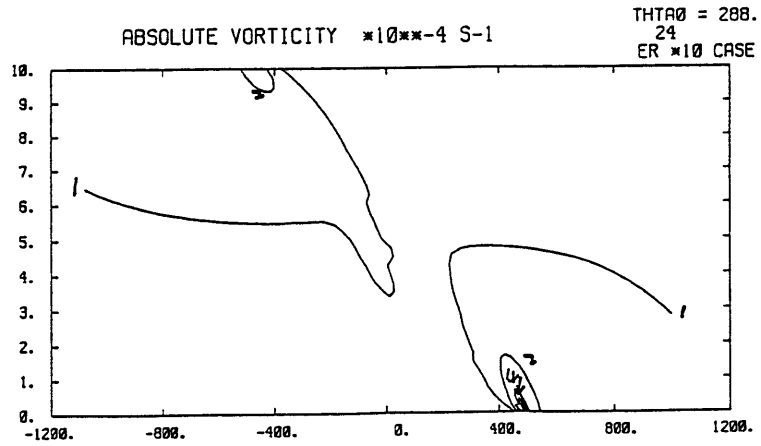

(5.6c) Absolute vorticity ζ (10^{-4} s^{-1}). ζ_{max} = 32.85 × 10^{-4} s^{-1}, ζ_{min} = 0.43 × 10^{-4} s^{-1}.

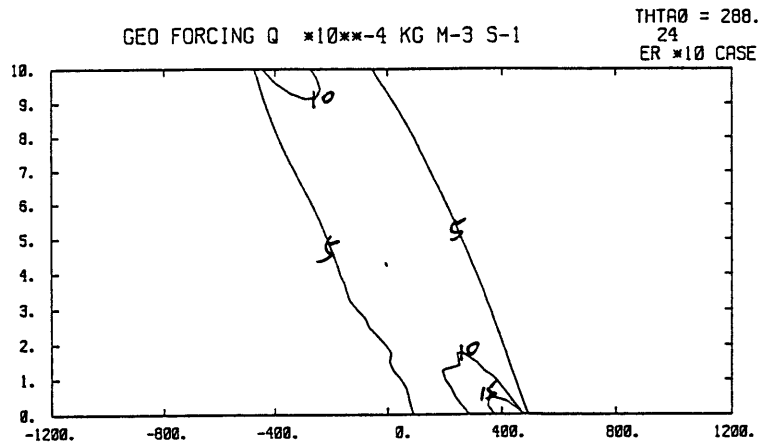

(5.6d) Geostrophic forcing Q (10^{-4} kg m^{-3} s^{-1}). $Q_{max} = 19.88 \times 10^{-4}$ kg m^{-3} s^{-1}.

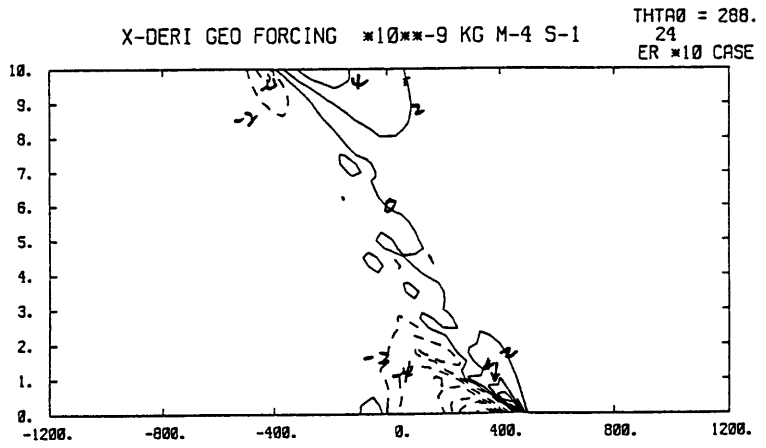

(5.6e) The x-derivative of geostrophic forcing $-Q_x$ (10^{-9} kg m^{-4} s^{-1}). $-Q_{x\,max} = 13.16 \times 10^{-9}$ kg m^{-4} s^{-1}, $-Q_{x\,min} = -13.85 \times 10^{-9}$ kg m^{-4} s^{-1}.

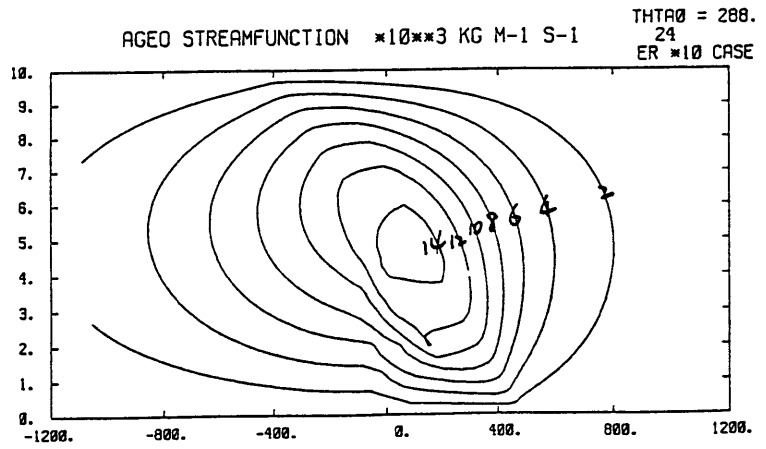

(5.6f) Streamfunction ψ (10^{3} kg m^{-1} s^{-1}). $\psi_{max} = 14.61 \times 10^{3}$ kg m^{-1} s^{-1}.

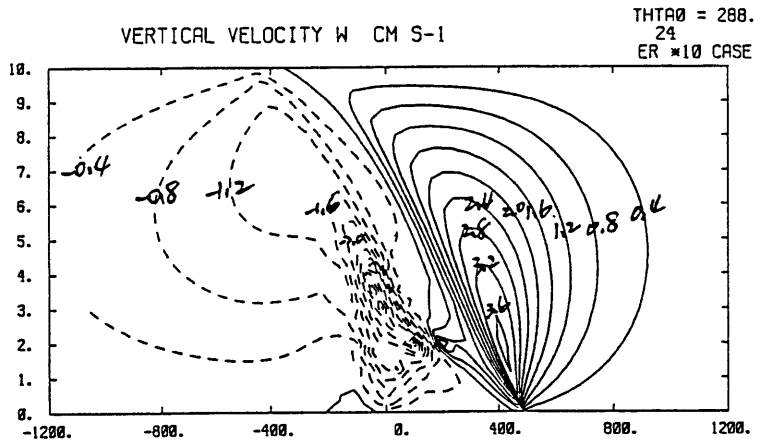

(5.6g) Vertical velocity w (cm s^{-1}). w_{max} = 3.65 cm s^{-1}, w_{min} = -4.24 cm s^{-1}.

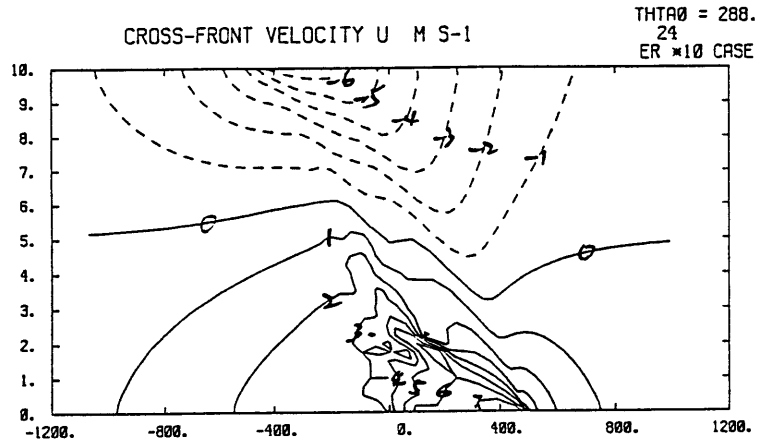

(5.6h) Ageostrophic velocity in the x-direction u_a (m s^{-1}). u_{amax} = 7.54 m s^{-1}, u_{amin} = -6.35 m s^{-1}.

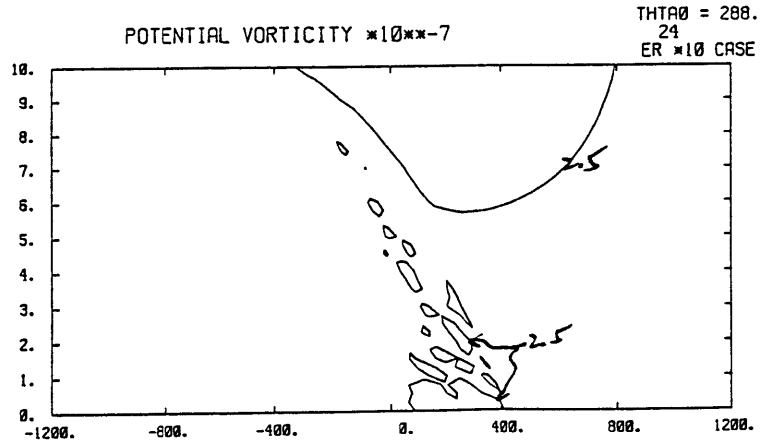

(5.6i) Potential vorticity q less than 2.5 × 10^{-7} m^2 °K s^{-1} kg^{-1}. q_{min} = 1.78 × 10^{-7} m^2 °K s^{-1} kg^{-1}, on the upper boundary.

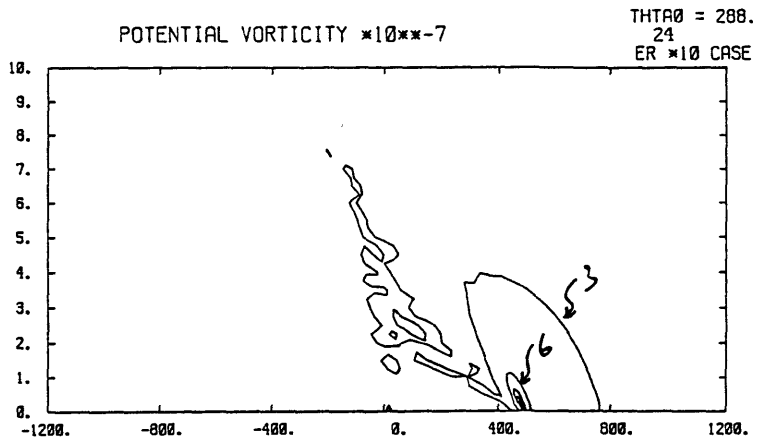

(5.6j) Potential vorticity q larger than 3×10^{-7} m^2 °K s^{-1} kg^{-1}. $q_{max} = 27.61 \times 10^{-7}$ m^2 °K s^{-1} kg^{-1}.

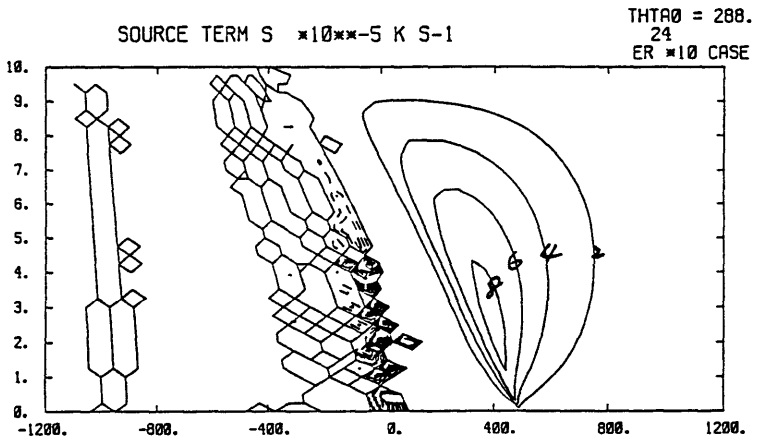

(5.6k) Source term (heating or cooling rate). $S_{max} = 8.59 \times 10^{-5}$ °K s^{-1}.

Figure 5.6 Case Er*10, after one day of simulation. Cross section in x-z plane in physical space; the unit is km in both z and x direction.

Case-D

	along front velocity m/s	absolute vorticity $10^{-4}s^{-1}$	geostrophic forcing $10^{-4}kgm^{-3}s^{-1}$	x-derivative geostrophic forcing $10^{-9}kgm^{-4}s^{-1}$	ageostrophic streamfunction $10^{3}kgm^{-1}s^{-1}$
hour 6	24.56 -24.56	1.42 0.74 0.74 1.42	7.04 7.04	-1.45 1.45 -1.45 1.45	8.48
hour 12	28.18 -28.18	1.66 0.69 0.69 1.66	8.71 8.71	-2.22 2.22 -2.22 2.22	9.15
hour 18	32.06 -32.06	2.08 0.64 0.64 2.08	10.75 10.75	-3.36 3.36 -3.36 3.36	9.80
hour 24	36.17 -36.17	3.10 0.58 0.58 3.10	13.25 13.25	-4.93 4.93 -4.93 4.93	10.36

	vertical velocity cm/s	cross-front velocity m/s	potential vorticity $10^{-7}kg^{-1}m^{2}Ks^{-1}$	condensation heating rate $10^{-5}Ks^{-1}$	
hour 6	-0.71 0.71	-3.84 3.84	N/A	N/A	
hour 12	-0.82 0.82	-4.27 4.27	N/A	N/A	
hour 18	-0.93 0.93	-4.70 4.70	N/A	N/A	
hour 24	-1.04 1.04	-5.14 5.14	N/A	N/A	

Frontal collapse at t = 120360 seconds, i=104, j=1

Table 5.1 Dry case (case-D). The maximum or minimum values at the upper boundary, lower boundary or interior of atmosphere, in every 6 hours up to 24 hours.

Case-C

	along front velocity m/s	absolute vorticity $10^{-4}s^{-1}$	geostrophic forcing $10^{-4}kgm^{-3}s^{-1}$	x-derivative geostrophic forcing $10^{-9}kgm^{-4}s^{-1}$	ageostrophic streamfunction $10^{3}kgm^{-1}s^{-1}$
hour 6	25.03 -25.04	1.44 0.73 0.74 1.48	7.03 7.03	-1.46 1.46 -1.46 1.46	10.14
hour 12	29.38 -29.40	1.72 0.66 0.68 1.91	8.69 8.69	-2.22 2.22 -2.22 2.22	11.51
hour 18	34.22 -34.25	2.29 0.58 0.62 3.06	10.71 10.71	-3.34 3.34 -3.34 3.34	12.85
hour 24	39.52 -39.51	4.00 0.51 0.56 12.52	13.18 13.18	-4.97 4.97 -4.97 4.97	14.06

	vertical velocity cm/s	cross-front velocity m/s	potential vorticity $10^{-7}kg^{-1}m^{2}Ks^{-1}$	condensation heating rate $10^{-5}Ks^{-1}$	
hour 6	-0.80 1.28	-4.31 4.31	2.49 3.04	3.21	
hour 12	-0.98 1.77	-4.96 4.96	2.26 3.83	4.40	
hour 18	-1.17 2.43	-5.61 5.61	2.01 5.84	5.94	
hour 24	-1.38 3.39	-6.28 6.27	1.77 19.30	8.12	

Frontal collapse at t = 92760 seconds, i=106, j=1

Table 5.2 As that of table 5.1, except for moist case (Case-C).

Case-E

	along front velocity m/s	absolute vorticity $10^{-4}s^{-1}$	geostrophic forcing $10^{-4}kgm^{-3}s^{-1}$	x-derivative geostrophic forcing $10^{-9}kgm^{-4}s^{-1}$	ageostrophic streamfunction $10^{3}kgm^{-1}s^{-1}$
hour 6	25.04 -27.32	1.43 0.73 0.63 1.61	7.03 11.28	-1.46 1.46 -10.97 6.43	10.18
hour 12	29.41 -32.30	1.72 0.65 0.53 1.95	8.69 13.55	-2.22 2.22 -12.10 7.90	11.62
hour 18	34.26 -38.16	2.29 0.58 0.45 3.28	10.71 16.06	-3.34 3.34 -13.30 9.73	13.05
hour 24	39.64 -44.54	4.05 0.50 0.40 29.72	13.18 19.34	-4.97 4.97 -13.89 12.33	14.44

	vertical velocity cm/s	cross-front velocity m/s	potential vorticity $10^{-7}kg^{-1}m^{2}Ks^{-1}$	condensation heating rate $10^{-5}Ks^{-1}$	max rate of evaporation s^{-1}
hour 6	-0.79 , -0.82 1.29	-4.32 4.66	2.49 3.04	3.23	$\sim 1.9*10^{-8}$
hour 12	-0.97 , -1.31 1.80	-4.97 5.89	2.26 3.87	4.45	$\sim 3.1*10^{-8}$
hour 18	-1.15 , -1.30 2.48	-5.64 6.60	2.01 6.05	6.06	$\sim 2.1*10^{-8}$
hour 24	-1.44 , -1.91 3.58	-6.34 7.15	1.77 27.53	8.44	$\sim 5.6*10^{-8}$

Frontal collapse at t = 88340 seconds, i=105, j=1

Table 5.3 As that of table 5.1, except for evapor case (case-E). The second value at the upper line in the column of vertical velocity denotes the second maximum descent induced by evaporation.

	along front velocity m/s	absolute vorticity $10^{-4}s^{-1}$	geostrophic forcing $10^{-4}kgm^{-3}s^{-1}$	x-derivative geostrophic forcing $10^{-9}kgm^{-4}s^{-1}$	ageostrophic streamfunction $10^{3}kgm^{-1}s^{-1}$
initial condition	21.22 -21.22	1.28 0.79 0.79 1.28	5.68 5.68	-0.96 0.96 -0.96 0.96	7.77
case-D	36.17 -36.17	3.10 0.58 0.58 3.10	13.25 13.25	-4.93 4.93 -4.93 4.93	10.36
case-C	39.52 -39.51	4.00 0.51 0.56 12.52	13.18 13.18	-4.97 4.97 -4.97 4.97	14.06
case-D	39.64 -44.54	4.05 0.50 0.40 29.72	13.18 19.34	-4.97 4.97 -13.89 12.33	14.44

	vertical velocity cm/s	cross-front velocity m/s	potential vorticity $10^{-7}kg^{-1}m^{2}Ks^{-1}$	condensation heating rate $10^{-5}Ks^{-1}$	Front collpase at
initial condition	-0.60 0.60	-3.42 3.42	N/A	N/A	N/A
case-D	-1.04 1.04	-5.14 5.14	N/A	N/A	t=120360 secs
case-C	-1.38 3.39	-6.28 6.27	1.77 19.30	8.12	t=92760 secs
case-E	-1.44 , -1.91 3.58	-6.34 7.15	1.77 27.53	8.44	t=88340 secs

Table 5.4 The data of initial condition and data of dry case (case-D), moist case (case-C) and evapor case (case-E) at hour 24.

Case Er/10

	along front velocity m/s	absolute vorticity $10^{-4}s^{-1}$	geostrophic forcing $10^{-4}kgm^{-3}s^{-1}$	x-derivative geostrophic forcing $10^{-9}kgm^{-4}s^{-1}$	ageostrophic streamfunction $10^{3}kgm^{-1}s^{-1}$
hour 6	25.04 -25.70	1.44 0.73 0.74 1.48	7.03 8.16	-1.46 1.46 -2.48 2.54	10.15
hour 12	29.39 -31.00	1.72 0.65 0.68 1.92	8.69 11.39	-2.22 2.22 -5.71 5.31	11.55
hour 18	34.23 -36.76	2.29 0.58 0.57 3.16	10.71 14.73	-3.34 3.34 -9.39 8.01	12.91
hour 24	39.55 -42.66	4.01 0.51 0.49 16.42	13.18 18.35	-4.97 4.97 -12.21 10.66	14.18

	vertical velocity cm/s	cross-front velocity m/s	potential vorticity $10^{-7}kg^{-1}m^{2}Ks^{-1}$	Condensation heating rate $10^{-5}Ks^{-1}$	max rate of evaporation s^{-1}
hour 6	-0.80 1.28	-4.32 4.48	2.49 3.04	3.22	$\sim 6*10^{-9}$
hour 12	-0.98 1.78	-4.96 5.26	2.26 3.84	4.41	$\sim 6*10^{-9}$
hour 18	-1.17 2.45	-5.62 6.04	2.01 5.96	5.96	$\sim 6*10^{-9}$
hour 24	-1.39 3.46	-6.28 6.85	1.77 21.91	8.25	$\sim 1.3*10^{-8}$

Frontal collapse at t = 90280 seconds, i=105, j=1.

Table 5.5 As that of 5.3, except with the rate of evaporation equal to one tenth of the rate of evaporation of case-E.

Case Er*10

	along front velocity m/s	absolute vorticity $*10^{-4}s^{-1}$	geostrophic forcing $10^{-4}kgm^{-3}s^{-1}$	x-derivative geostrophic forcing $10^{-9}kgm^{-4}s^{-1}$	ageostrophic streamfunction $10^{3}kgm^{-1}s^{-1}$
hour 6	25.02 -28.38	1.43 0.73 0.53 1.82	7.03 12.02	-1.46 1.46 -10.84 7.27	9.96
hour 12	29.34 -33.60	1.71 0.65 0.52 2.19	8.69 14.19	-2.22 2.22 -8.48 8.90	11.27
hour 18	34.16 -39.19	2.29 0.58 0.48 3.25	10.71 16.78	-3.34 3.34 -10.61 10.82	12.50
hour 24	39.55 -45.37	4.01 0.51 0.43 32.85	13.18 19.88	-4.97 4.97 -13.85 13.16	14.61

	vertical velocity cm/s	cross-front velocity m/s	potential vorticity $10^{-7}kg^{-1}m^{2}Ks^{-1}$	Condensation heating $10^{-5}Ks^{-1}$	max rate of evaporation s^{-1}
hour 6	-0.77 , -2.14 1.29	-4.24 5.05	2.49 3.10	3.23	$\sim 8.7*10^{-8}$
hour 12	-0.93 , -1.85 1.79	-4.86 6.16	2.26 3.87	4.42	$\sim 1.3*10^{-8}$
hour 18	-1.11 , -2.17 2.35	-5.53 6.15	2.02 6.00	5.93	$\sim 6.1*10^{-7}$
hour 24	-1.38 , -4.24 3.65	-6.35 7.54	1.78 27.61	8.59	$\sim 2.4*10^{-7}$

Frontal collapse at t = 88220 seconds i=105, j=1.

Table 5.6 As that of 5.3, except with the rate of evaporation equal to ten times the rate of evaporation of the case-E.

Hour 24

	along front velocity m/s	absolute vorticity $10^{-4}s^{-1}$	geostrophic forcing $10^{-4}kgm^{-3}s^{-1}$	x-derivative geostrophic forcing $10^{-9}kgm^{-4}s^{-1}$	ageostrophic streamfunction $10^{3}kgm^{-1}s^{-1}$
case Er/10	39.55 -42.66	4.01 0.51 0.49 16.42	13.18 18.35	-4.97 4.97 -12.21 10.66	14.18
case-D (Er)	39.64 -44.54	4.05 0.50 0.40 29.72	13.18 19.34	-4.97 4.97 -13.89 12.33	14.44
case Er*10	39.55 -45.37	4.01 0.51 0.43 32.85	13.18 19.88	-4.97 4.97 -13.85 13.16	14.61

	vertical velocity cm/s	cross-front velocity m/s	potential vorticity $10^{-7}kg^{-1}m^{2}Ks^{-1}$	Condensation heating $10^{-5}Ks^{-1}$	max rate of evaporation s^{-1}
case Er/10	-1.39 3.46	-6.28 6.85	1.77 21.91	8.25	$\sim 1.3*10^{-8}$
case-D (Er)	-1.44 , -1.91 3.58	-6.34 7.15	1.77 27.53	8.44	$\sim 5.6*10^{-8}$
case Er*10	-1.38 , -4.24 3.65	-6.35 7.54	1.78 27.61	8.59	$\sim 2.4*10^{-7}$

Table 5.7 The data of the case Er/10, the case-E (Er) and the case Er*10 at hour 24.

	Time of frontal collapse
case-D	1 day 9 hours 26 minutes
case-C	1 day 1 hour 46 minutes
case-E	1 day 32 minutes 20 seconds
case Er/10	1 day 1 hour 4 minutes 40 seconds
case Er*10	1 day 30 minutes 20 seconds
case RH75	1 day 1 hour 21 minutes 20 seconds
case RH95	23 hours 41 minutes 20 seconds

Table 5.8 The comparison of the time needed for front to collapse in different cases.